UNIVERSITY OF THESSALY

SCHOOL OF ENGINEERING

DEPARTMENT OF MECHANICAL ENGINEERING

Diploma Thesis

Modeling microstructural evolution of austenitic stainless steels in additive manufacturing

By

Marios P. Sotiriou

Submitted in partial fulfillment of the requirements for the degree of Diploma in Mechanical Engineering at the University of Thessaly

2023

Approved by Members of the Thesis Committee

First Member (Supervisor)

Prof. Gregory N. Haidemenopoulos
Department of Mechanical Engineering, University of Thessaly

Second Member

Prof. Nikolaos Aravas
Department of Mechanical Engineering, University of Thessaly

Third Member

Prof. Vasilis Bontozoglou
Department of Mechanical Engineering, University of Thessaly

Date approved: June 15, 2023

Abstract

This study is concerned with the modeling of the heat transfer and microstructural evolution of austenitic stainless steels in Additive Manufacturing (AM), within an Integrated Computational Materials Engineering (ICME) framework. The thermodynamics and kinetics of solidification are investigated. The effect of the cooling rate is taken into account, through dendrite growth theory. CALPHAD-based modeling is applied to predict non-equilibrium thermophysical properties under rapid cooling conditions. Heat transfer and diffusion analyses are carried out in sequence. An in-house heat transfer model is developed to perform thermal simulations using FEM, considering the effect of the powder. The calculated temperature history is provided as input for the microstructural simulation of solidification and solid-state transformations, upon rapid cooling and thermal cycling. A CALPHAD modeling methodology of solidification and solid-state transformations upon thermal cycling is developed, to consider the variance in solidification type, cooling rate and growth mechanism. The methodology is applied on an AISI 316L austenitic stainless steel with microstructural results in agreement with experimental evidence, as a case study to establish a benchmark simulation scheme for Selective Laser Melting (SLM) and other additive manufacturing processes.

Preface

A version of Chapter 4 was published in a conference paper:

M.P. Sotiriou, J.S. Aristeidakis, M.-I.T. Tzini, I. Papadioti, G.N. Haidemenopoulos, N. Aravas, *Microstructural and Thermomechanical Simulation of the Additive Manufacturing Process in 316L Austenitic Stainless Steel*, (2021) 20. https://doi.org/10.3390/iec2m-09237.

A version of Chapter 5 was published in a conference paper:

M.P. Sotiriou, J.S. Aristeidakis, S.A. Koimtzidis, I. Papadioti, M.-I.T. Tzini, G.N. Haidemenopoulos, N. Aravas, *Microstructural and heat transfer modeling of selective laser melting in austenitic stainless steels*, (2022)

Versions of Chapter 3, Chapter 4 and Chapter 5 were presented at conferences:

M.P. Sotiriou, M.I.T. Tzini, J.S. Aristeidakis, G.N. Haidemenopoulos, I. Barsoum, "*A computational study of solidification during additive manufacturing of AISI 304 austenitic stainless steel*", 7th Pan-Hellenic Conference of Metallic Materials, December 11-13, 2019. Available at ResearchGate.

Marios P. Sotiriou, John S. Aristeidakis, Maria-Ioanna T. Tzini, Ioanna Papadioti, Gregory N. Haidemenopoulos, Nikolaos Aravas, "*Microstructural and Thermomechanical Simulation of the Additive Manufacturing Process in 316L Austenitic Stainless Steel*", The 1st International Electronic Conference on Metallurgy and Metals, Volume: Mater. Proc. 2021, 3(1), 20, DOI: 10.3390/IEC2M-09237.

M.P. Sotiriou, J.S. Aristeidakis, M.I.T. Tzini, I. Papadioti, G.N. Haidemenopoulos, N. Aravas, "*Thermomechanical and microstructural simulation of the AM process of 316L austenitic stainless steel*", 6th International Virtual Conference of Engineering Against Failure, June 23-25, 2021.

M.P. Sotiriou, J.S. Aristeidakis, S. Koimtzidis, I. Papadioti, M.I.T. Tzini, N. Aravas, G.N. Haidemenopoulos, "*Microstructural and thermomechanical modeling and simulation of selective laser melting in austenitic stainless steels*", 8th International Conference of the Hellenic Metallurgical Society, December 14-16, 2022.

Table of Contents

List of figures

List of tables

Acknowledgements

In my years at the University of Thessaly I met a lot of interesting people that defined my academic and personal character. Every adventure in science begins in ignorance and it is always a difficult path to move forward. But fortunately, there is company along the journey, with spirited minds and good hearts that aid in creating order from disorder.

I am grateful to my advisor Prof. Greg Haidemenopoulos, for guiding my first steps in research and inspiring my love for materials science. He trusted me early on my academic journey and gave me the opportunity and the means to aim for my dreams. His invaluable mentoring and the team he created at the University of Thessaly will always be in my heart. I dedicate to him Chapter 2 – Solidification theory in austenitic stainless steels, for compelling me to explain a small part of the world by searching for the truth. I feel honored to have been his student. I would like to extend my sincere thanks to Prof. Nikolaos Aravas, for co-advising me in my thesis. I greatly admire his passion towards proper research, teaching me how to be a better scientist. I am greatly thankful to Prof. Vasilis Bontozoglou for serving in my thesis committee as well as for being an influence on how enthusiasm towards a field of study can make the difference.

Special thanks to all past and present members of the Laboratory of Materials of the University of Thessaly, that I had the chance to meet. I offer my appreciation to Dr. Eleni Kamoutsi for introducing me to the principles of physical metallurgy as well as for her constant support through the years. Also, since I had the pleasure to have a small number of students on my own, I would like to extend my gratitude to them for making me discover my passion for teaching, with the promise to get better. Over the course of this thesis, I had the pleasure of working alongside several members of the Laboratory of Computational Mechanics of the University of Thessaly. Special thanks to Dr. Ioanna Papadioti for helping me with the simulation of heat transfer in additive manufacturing. I appreciate the collaboration with Symeon Koimtzidis, who I thank for his friendship and determination to improve our work. I am also thankful to my friend Sokratis Xenos for the inspiring conversations on computational and philosophical matters.

I could not have undertaken this journey without my dear friends Dr. John Aristeidakis and Dr. Margianna Tzini. I am deeply grateful for their teaching, patience and invaluable friendship offered from their hearts. To them I dedicate Chapter 4 – CALPHAD-based simulation of microstructural evolution, with the promise that this does not end here. It is a blessing that I have people believe in me and I hope to make them proud one day. Words cannot effectively express my love and gratitude towards my friends Christina, Lenou, my childhood friends Apostolis, Andreas, Dimitris, Lampros, Argyris and many more. I thank them for always standing with me in the light of joy as in shade of challenge. Finally, I send all my love to my parents, for their rigid belief and unquestioning support. Without them I could not have reached this far.

Sincerely,
Marios Sotiriou
June 2023, Volos

This thesis is dedicated to my parents

Theodora and Panagiotis

Chapter 1. Introduction

1.1. Problem definition

Metal part Additive Manufacturing (AM), commonly referred to as metallic "3D-printing" is emerging in recent years as a novel technique of producing near-net-shape three-dimensional parts derived directly from CAD models by fusing raw materials with various energy sources (e.g., electron beam EB, laser beam LB, electric arc). Complex geometry parts produced using AM, which could be impractical or impossible and cost-expensive to produce following traditional machining approaches, achieve the demanding natural shapes required in many bioengineering applications as in dental prosthetic components, or yield excellent strength to weight ratios ideal for automotive and aerospace applications. However, advanced industrial AM production is challenged by issues concerning the controllability and reproducibility in manufacturing [1], let alone process-associated inherent time and cost restrictions [2]. Accelerating the adoption of AM requires building on existing knowledge related to heat transfer, non-equilibrium phase transformations and high-performance modeling within a fundamental computational approach using Integrated Computational Materials Engineering (ICME) tools, in order to avoid time- and cost-consuming extensive experimentation to determine standard specific sets of manufacturing parameters [3,4].

AM processes can be classified based on the method of material deposition, either as Powder Bed (PB) when a metallic powder layer is spread over a pre-existing surface using a powder roller or blade, or as Powder Deposition (PD) when the metallic powder is deposited directly on the heat spot via a moving nozzle. Therefore, AM processes involve repeated deposition of metallic material, followed by a heat source pass to melt and fuse the powder in selected areas, building layer-by-layer the 3D structure. The procedure is characterized by the development of an inhomogeneous temperature field that evolves both spatially and temporally, determining the microstructural evolution. The resulting rapid heating and cooling cycles lead to phase transformations under non-equilibrium conditions. In non-equilibrium processes, the solidus temperature is affected by the cooling path as increasingly higher cooling rates allow for solidification to continue at lower temperatures. An implication of high-rate or rapid solidification is the development of thermal expansion/contraction of the material resulting in development of significant residual stresses and distortions in the part resulting in warping-induced failure [5,6]. The ensuing rapid thermal cycling can further influence the development of undesirable microstructural features, such as significant elemental microsegregation, leading to composition and subsequently physical and property inhomogeneities like poor corrosion resistance. Microsegregation is mainly caused by limited diffusion of substitutional elements in the solid phases, causing compositions to deviate from the equilibrium, near the solid/liquid interface, as solidification progresses, thus fast diffusing elements like carbon usually do not segregate significantly. It is important to accurately model solidification related phenomena, in order to predict and optimize microstructures produced by AM and consequently the mechanical properties, such as elasticity, yield strength and stiffness [7]. Despite extensive research in the field there are still many challenges during production, arising from multifaceted interaction of various physical phenomena involving many fields of study, including heat and mass transfer, phase transformations, elastic and plastic deformation, and residual stresses.

1.2. Thesis objective and Outline

Although extended literature has been dedicated to additive manufacturing research [2,8–10], yet a model for the accurate prediction of the as-built microstructure with respect to the processing parameters remains to be developed. The importance of investigation of the microstructural evolution resides in the value of interpretation of the contributing mechanisms, in order to proceed to design and optimization of the manufacturing products for the various applications. The present analysis aims in achieving insight into the phenomena that determine the microstructural evolution of austenitic stainless steels in additive manufacturing, as well as in processes that involve rapid cooling, and focuses on the development of a benchmark simulation framework to predict the microstructural evolution of austenitic stainless steels in welding and additive manufacturing, setting the general methodology foundations for computational material design and optimization in additive manufacturing applications.

An integrated heat transfer and microstructural simulation methodology of additive manufacturing is designed to determine accurately the transient temperature field and the microstructural evolution, thus the morphology and spatial/temporal distribution of phases and alloying elements. Heat transfer and microstructural analyses are carried out in sequence. Initially, non-equilibrium microstructural modeling is applied to predict the thermophysical properties under rapid cooling conditions. Heat transfer simulations are performed via the development of an in-house 2D-FEA model in ABAQUS for additive manufacturing, considering the effect of the powder. The calculated temperature history is provided as input for the microstructural simulation of solidification and solid-state transformations. A CALPHAD-based approach of solidification and solid-state transformations upon thermal cycling is developed, to consider the variance in solidification type (alloy composition), cooling rate (from the electric arc to laser beams) and growth mechanism (epitaxial growth, nucleation and growth). The methodology is applied on an AISI 316L austenitic stainless steel as a case study to establish a benchmark simulation scheme for Selective Laser Melting (SLM) and other additive manufacturing processes [11]. A schematic illustration of the applied methodology, including a final mechanical analysis that is not elaborated upon the present study, is given in Figure 1.1.

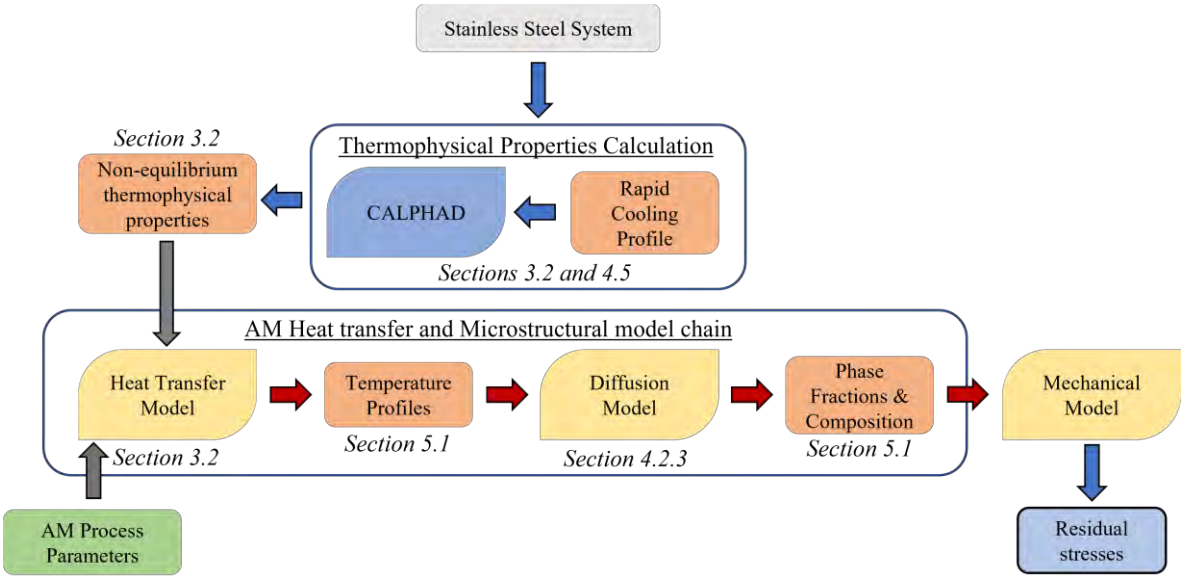

Figure 1.1. Flowchart of the proposed simulation methodology for additive manufacturing processes.

The integrated simulation methodology employed a benchmark 316L system with composition given in Table 1.1, under the manufacturing conditions described in 2D SLM experiments conducted by Bertsch et al. [12], as reference act as a case study on the application of the methodology.

Table 1.1. Benchmark AISI 316L composition in (wt%)

316L	Cr	Ni	Mo	C	Mn	Fe
Composition (wt%)	18.39	13.94	2.6	0.03	1.47	bal.

In Chapter 2, solidification is thoroughly examined for its dominant influence on the microstructure formation and associated microsegregation. The thermodynamics and kinetics of solidification are investigated and the effects of the cooling rate are established taking into account the dendrite growth theory. In Chapter 3, a finite element heat transfer model is developed in ABAQUS, to describe the transient temperature evolution in additive manufacturing processes with high fidelity, since the thermal history is essential in determining the resulting microstructure. In Chapter 4, thermodynamic and kinetic models of solidification are employed to simulate the microstructural evolution upon solidification and subsequent solid-state transformations, using the CALPHAD approach through the Thermo-Calc software, including Scheil-Gulliver model and DICTRA model that consider diffusion in multiphase and multicomponent systems. The effect of processing parameters on critical microstructural features such as the freezing range, phase fractions, and elemental segregation is investigated. Solidification and solid-phase transformations are examined upon thermal cycling via multi-phase and multi-component diffusion simulations. In 5.1, the results of the analysis are presented. The ensuing microstructural properties, including phase fractions and constitutions, as well as the temperature field can be provided as an input for a mechanical analysis, to calculate the residual stresses and distortions.

Chapter 2. Solidification theory in austenitic stainless steels

2.1. Microstructure of as-cast austenitic stainless steels

Austenitic stainless steels of the AISI 300 series containing Cr (16 to 25 wt%) and Ni (8 to 20 wt%) [13,14], are the most common type of stainless steels, employed for a wide variety of applications for their excellent combinations of corrosion resistance, high/low temperature performance and mechanical strength [15,16]. While Cr is added to induce the stainless character by formation of the protective Cr_2O_3 oxide film, Ni aims in promoting the austenitic microstructure at ambient temperatures to avoid ductile-to-brittle transition and maintain high performance [13,14]. Additional alloying with Mo, Mn, Si, N, Ti or Nb, yields further enhancement of desirable properties like oxidization or creep resistance. For example, the addition of Mo (AISI 316 grades) or a small amount of N (AISI 3xxN grades) can improve pitting resistance [17]. Some typical AISI 300 systems are given in Table 2.1.

Table 2.1. Nominal compositions of AISI 300 series stainless steels [13,18].

Type	Microstructure	Nominal composition (wt%)									
		Cr	Ni	C	Mn	Si	Mo	Nb	N	Other	Fe
301	Austenitic	17	7	0.08	1	0.5	-	-	0.05	-	bal.
302	Austenitic	18	9	0.08	1	0.4	-	-	-	-	bal.
303	Austenitic FM	19	9	0.08	1	0.5	-	-	-	S	bal.
304	Austenitic	19	9.25	0.04	1	0.4	-	-	-	-	bal.
304L	Austenitic	19	10	0.02	1	0.4	-	-	-	-	bal.
304N	Austenitic	19	9.2	0.04	1	0.4	-	-	0.13	-	bal.
304LN	Austenitic	19	10	0.02	1	0.4	-	-	0.13	-	bal.
305	Austenitic	18	11.8	0.06	1	0.4	-	-	-	-	bal.
306	Austenitic	17.8	14.8	0.01	1	4	-	-	-	-	bal.
308	Austenitic	20	11	0.04	1	0.5	-	-	-	-	bal.
309	Austenitic	23	13.5	0.1	1	0.5	-	-	-	-	bal.
310	Austenitic	25	20.5	0.15	1	0.75	-	-	-	-	bal.
314	Austenitic	24.5	20.5	0.15	1	2.25	-	-	-	-	bal.
316	Austenitic	17	12	0.04	1	0.4	2.2	-	-	-	bal.
316L	Austenitic	17	12	0.02	1	0.4	2.2	-	-	-	bal.
316LN	Austenitic	17	12	0.02	1	0.4	2.2	-	0.13	-	bal.
317	Austenitic	19	13	0.04	1	0.4	3.3	-	-	-	bal.
321	Austenitic	18	10.5	0.04	1	0.4	-	-	-	Ti	bal.
329	Duplex	25.5	3.5	0.04	0.5	0.4	-	-	-	-	bal.
330	Austenitic	18.5	35.5	0.05	1	1.2	-	-	-	-	bal.
334	Austenitic	19	20	0.04	0.5	0.5	-	-	-	Al, Ti	bal.
347	Austenitic	18	11	0.04	1	0.4	-	0.6	-	-	bal.
348	Austenitic	18	11	0.04	1	0.4	-	0.6	-	Ta	bal.

Most austenitic stainless steel grades are considered weldable, if precautions are applied in design to avoid defect or failure issues that decrease weldability, like hot-cracking, sensitization, ductility dip cracking, reheat cracking and copper contamination cracking [19]. Hot-cracking is one of the commonly encountered failure types during welding, occurring when residual liquid is retained between solidified grains for extended freezing ranges,

resulting in tearing upon development of contraction-induced stresses due to solidification. It is possible to reduce the freezing range and avoid hot-cracking by modifying the system's thermodynamics. Moreover, sensitization refers to precipitation of chromium carbides on the grain boundaries in the Heat Affected Zone (HAZ), increasing the susceptibility for intergranular corrosion. The development of the L austenitic stainless steel grades (AISI 3xxL), with decreased content of C that inhibits the precipitation of chromium carbides, or micro-alloying with Ti or Nb promoting corresponding MC carbides to avoid chromium engagement, can reduce sensitization susceptibility and its effects. Welding standards exist for all weldability risk factors, and typical material grades have been developed as those presented in Table 2.1, to provide solutions that are reliable for most applications.

From traditional casting to welding and modern additive manufacturing processes that involve the melt state, microstructural evolution initiates with solidification. The as-solidified microstructure is the product of only the solidification transformation while the as-cast microstructure is defined as the result of both solidification and subsequent solid-state transformations that occur during the following cooling stage, without any additional post-processing. The importance of solidification resides in determining key-aspects of the as-solidified and as-cast microstructures like the initial solid morphology, phase contents and spatial distribution of alloying elements across various scaling orders, namely the macro- and micro-segregation, that are able to influence microstructural features until the final product. Most process-chains that involve casting, consider the as-cast as an intermediate microstructural stage and design the following steps in reference to the as-cast product. In welding, the as-cast microstructure often undergoes minimal post-treatment due to physical or financial restrictions and design must be applied to control the microstructure throughout the process, making the as-cast the near-end product. In additive manufacturing, the unconventional building conditions provide the ability to create unique microstructural features like small grain size [12] (sub-grain structures that are often $< 1\,\mu m$), control of the crystallographic texture orientation control [20] and spatial solute segregation to differentiate local distribution of properties [21].

It is therefore necessary to study the as-solidified and as-cast microstructures as well as solidification as the dominant phase transformation, in order to apply alloy design to as-cast products. This chapter is concerned with the investigation of the microstructural evolution of AISI 300 series austenitic stainless steels in welding and additive manufacturing. The theoretical principles of solidification are analyzed in the context of welding, as a fundamental case. Additive manufacturing is considered a subcase of welding and the same theoretical principles are therefore applied.

2.1.1. Thermodynamics of solidification in austenitic stainless steels

Thermodynamic behavior of AISI 300 series austenitic stainless steels is based on the ternary Fe-Cr-Ni system. The complete phase diagram of such system is a three-dimensional entity that can be represented in two dimensions with ternary diagrams. Ternary diagrams provide useful insight for constitutional investigation and correlation of alloying elements and their effect in the system's thermodynamics. However, it is difficult to contemplate microstructural evolution without considering the temperature, therefore, isopleth sections of the phase diagram, are commonly used as the starting point of most thermodynamic analyses. An exemplary isopleth section of the phase diagram at 18 wt% Cr, of the ternary Fe-Cr-Ni system is presented in Figure 2.1 (calculated based on the CALPHAD methodology of computational

thermodynamics, implemented in Thermo-Calc [22] and validated from [23]), based on the reference AISI 304 composition Fe-18Cr-8Ni (known as 18-8 grade steels). From Figure 2.1 it is evident that δ-ferrite and austenite are the only thermodynamically stable solid-solutions around the solidification temperature range across the Ni compositional range. The Cr/Ni ratio (given on the lower horizontal axis of Figure 2.1) is widely used to quantify the solidification behavior, since it captures the correlation between austenite-stabilizing Ni content and ferrite-stabilizing Cr content that influence the extent of their respective thermodynamic regions. Low Cr/Ni compositions prefer to solidify with austenite first, while high Cr/Ni compositions prefer primary δ-ferrite solidification.

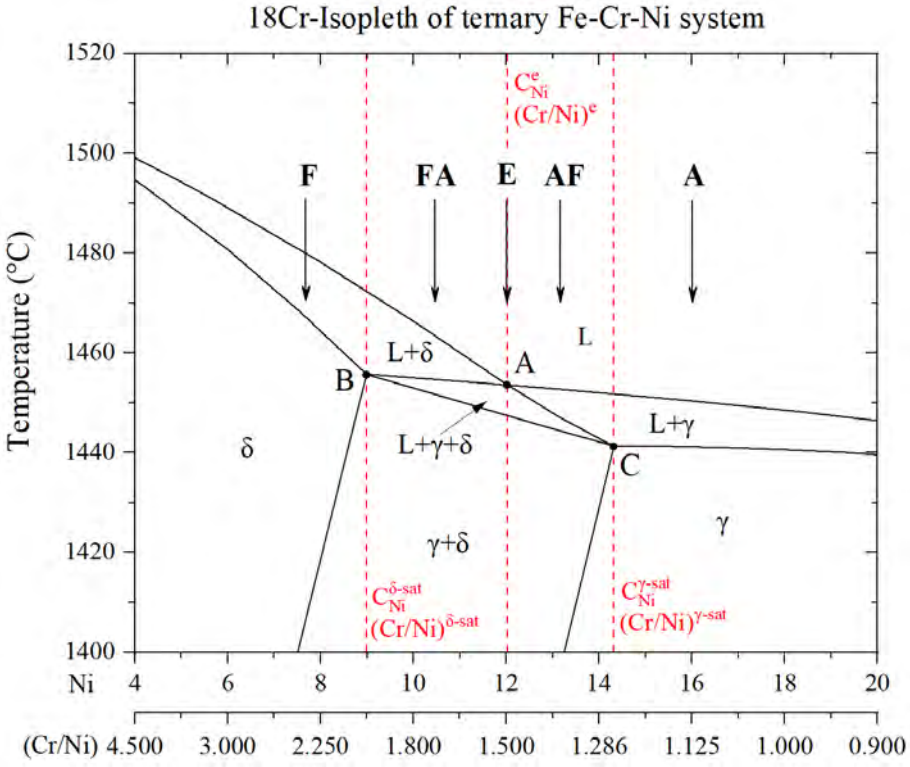

Figure 2.1. 18Cr-Isopleth section of Fe-Cr-Ni and definition of solidification paths [23].

The linear structure defining the three-phase region is referred in the literature as the tie-triangle [13,14] and describes simultaneous growth of both austenite and ferrite from the melt. Notice that in contrast to binary systems, where the three-phase reaction (eutectic or peritectic) is defined by a line, in ternary systems the additional degree of freedom provided by the third alloying element allows for the reaction to occur in a compositional and a temperature range. The apexes of the tie-triangle are defined by points *A*, *B* and *C*, as noted in Figure 2.1: point *A* is the location of the eutectic liquidus temperature and points *B*, *C* correspond to the three-phase compositional solubility limit values for δ-ferrite and austenite respectively. The triangle's sides, namely solvus lines *AB* and *AC*, as well as the line of two-fold saturation *BC*, define transformation limits for solidification. In multi-component systems, the tie-triangle is visible in the Cr and Ni isopleth sections of the phase diagram. Phase equilibria are carried out across the span of Ni content, revealing the compositional dependance of solidification classified by the solidification mode, the relative position of the equilibrium solidification path in reference to the position of the tie-triangle *ABC*. Solidification mode is a significant characteristic, since it qualifies the solidification thermodynamics and controls the

microstructural evolution (phase fractions and composition) of the as-solidified and thus, the as-cast microstructure.

The Primary Solidification Mode (PSM) is defined by the first solid phase to grow from the melt and is determined by the relative position of the system's solidification path, compared to the eutectic point's (point *A*) abscissa C_{Ni}^{e}. If $C_{Ni} < C_{Ni}^{e}$ the alloy solidifies with δ-ferrite first, if $C_{Ni} > C_{Ni}^{e}$ it solidifies with austenite first and if $C_{Ni} = C_{Ni}^{e}$ the eutectic reaction commences with simultaneous growth of austenite and δ-ferrite from the melt. Similar criteria can be formulated in terms of Cr/Ni ratios, which constitute a more applicable tool in multi-component systems, where $(Cr/Ni)^{\gamma-sat}$ refers to the Cr/Ni ratio corresponding to point *C* and $(Cr/Ni)^{\delta-sat}$ refers to the Cr/Ni ratio corresponding to point *B*. PSM types are given in Table 2.2 for the ternary system. Total Solidification Mode (TSM) in addition to PSM, requires determination of secondary phase formation -if evident- and is taken into account from the relative position of the solidification path in relation to all of the tie-triangle's apexes (points *A*, *B*, *C*). Therefore, a total of five distinct solidification modes are constituted: types A (solidification of only Austenite), AF (solidification of first Austenite then δ-Ferrite), E (simultaneous solidification of both Austenite and δ-Ferrite), FA (solidification of first δ-Ferrite then Austenite) and F (solidification of only δ-Ferrite), with classification criteria for the ternary system given in Table 2.2. Note that the first letter of type signs refers to the PSM, while the second, if existing, refers to the second solidifying phase.

Table 2.2 Equilibrium solidification modes

Cr/Ni	TSM	PSM	Reaction sequence
$\left(\frac{Cr}{Ni}\right) < \left(\frac{Cr}{Ni}\right)^{\delta-sat}$	F	F	$L \rightarrow L + F \rightarrow F$
$\left(\frac{Cr}{Ni}\right)^{\delta-sat} < \left(\frac{Cr}{Ni}\right) < \left(\frac{Cr}{Ni}\right)^{e}$	FA	F	$L \rightarrow L + F_p \rightarrow L + F_p + (A+F)_e \rightarrow A + F$
$\left(\frac{Cr}{Ni}\right) = \left(\frac{Cr}{Ni}\right)^{e}$	E	E	$L \rightarrow L + (A+F)_e \rightarrow A + F$
$\left(\frac{Cr}{Ni}\right)^{e} < \left(\frac{Cr}{Ni}\right) < \left(\frac{Cr}{Ni}\right)^{\gamma-sat}$	AF	A	$L \rightarrow L + A_p \rightarrow L + A_p + (A+F)_e \rightarrow A + F$
$\left(\frac{Cr}{Ni}\right)^{\gamma-sat} < \left(\frac{Cr}{Ni}\right)$	A	A	$L \rightarrow L + A \rightarrow A$

Table 2.2 also contains information regarding the solidification reactions for each mode. For types A and F, austenite or δ-ferrite respectively, is the only solid phase growing from the melt throughout solidification. For type AF, evolution of primary austenite A_p commences below liquidus and continues until the solidification path crosses the δ-ferrite solvus, from which point the three-phase reaction is activated and both austenite and δ-ferrite grow from the melt. FA type exhibits the opposite sequence, with primary ferrite F_p and a secondary eutectic mixture. In processes close to equilibrium conditions (e.g., casting) it is possible to distinguish between primary and secondary ferrite or austenite [24]. Finally, the eutectic type E in processes close to equilibrium, does not involve any distinct primary solidification phase growth.

The thermodynamic description of the 18Cr-Isopleth section of the Fe-Cr-Ni system is extended to confine all systems across the entire ternary Fe-Cr-Ni compositional range. The ternary Fe-Cr-Ni phase diagram is given in Figure 2.2(a) [23], calculated based on the CALPHAD methodology of computational thermodynamics, implemented in Thermo-Calc [22], employing the TCFE6 thermodynamic database for ferrous alloys. Note that only Cr and Ni content are independent variables, with the value of Fe acting as complement for every system. Thermodynamic mapping of the phase equilibria is carried out in isothermal sections, for a set of reference temperature values, spanning from 1500 to 1360°C at constant intervals of 20°C, to reveal the solidification behavior across the entire compositional range.

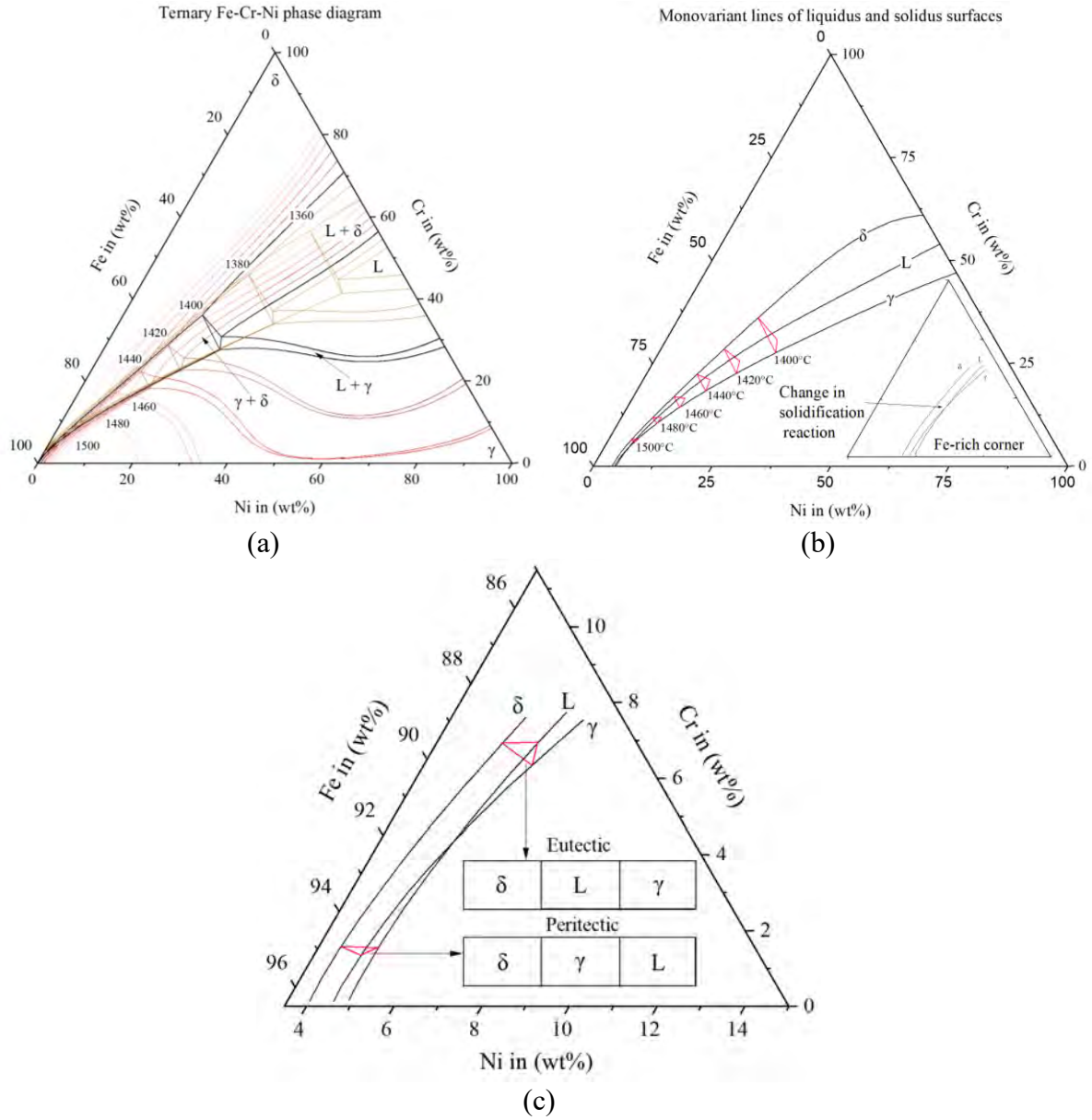

Figure 2.2. Phase equilibria of ternary Fe-Cr-Ni system: (a)Ternary Fe-Cr-Ni phase diagram, (b) monovariant lines of liquidus and solidus surfaces and evolution of the tie triangle with temperature, and (c) detail of monovariant lines of the liquidus and solidus surfaces at the Fe-rich corner of the ternary Fe-Cr-Ni system. Thermodynamic change of the tie-triangle from acute to obtuse, indicating change in the reaction from eutectic to peritectic.

In Figure 2.2(a) the constitutional dependence of liquidus and solidus temperatures, as well as all thermodynamic regions of the system is captured. Systems rich in Fe exhibit higher liquidus temperatures, while iron-poor systems with equal Cr and Ni contents remain on the liquid state even as low as 1360°C. From Figure 2.2(a), the evolution of the tie-triangle with composition and temperature for the ternary system is isolated in Figure 2.2(b). The liquidus projection surfaces of austenite and δ-ferrite converge to the eutectic point A of the tie triangle for all systems, forming the L-monovariant line. Similarly, the austenite and ferrite solvus projection surfaces converge with the line of two-fold saturation for all systems in points B and C of the tie-triangle, forming the δ and γ-monovariant lines upon application of austenite or δ-ferrite depletion criteria respectively. These lines indicate the composition of the phases and the temperature of solidification reactions.

All lines begin at the peritectic reaction in the Fe-rich side of a Fe-Ni system and culminate at eutectic reactions in Cr-Ni systems of similar content amounts [19]. The nature of the three-phase reaction is therefore composition dependent. Transition between reaction schemes takes place in the Fe-rich side of the diagram, where the shape of the tie-triangle changes from acute to obtuse, due to change of the relative position in the trajectories of L and γ-monovariant lines, as pictured in Figure 2.2(c). For most austenitic stainless steels, Ni content is higher than 6 wt%, thus the three-phase reaction should always be eutectic in character. However, in the welding literature [13,19,25] the terms eutectic and peritectic have been used to describe some as-cast microstructures, often in accordance with metallographic observations [25], indicating uncertainty regarding the specific solidification mechanism. A possible explanation is that in processes far from equilibrium where microsegregation phenomena apply, there can be sufficient spatial solute distribution to reach the peritectic thermodynamic region and locally change the type of the solidification three-phase reaction, during the microstructural evolution. Yu et al. [25] presented experimental evidence of austenite forming alongside dendritic grain boundaries between primary δ-ferrite dendrites and residual liquid on a 304 F type system, proving that the three-phase reaction has a peritectic component as well. Similar results were provided in [25] for a 310 A system where δ-ferrite evolved on interdendritic cavities due to solute trapping. Both cases exhibit a transition from single phase to two-phase solidification, entering thermodynamic regions inside the tie triangle. This indicates that the development of microsegregation, creating a moving boundary layer that moves with the solid/liquid interface, can alter the composition locally inside interdendritic regions, resulting in occurrence or change of the three-phase reaction character according to thermodynamic indication. Yonemura et al. [26] presented cases of two-phase solidification systems, where δ and γ are eutectic in the first solidification stage and peritectic in the late solidification stage. Therefore, either single-phase solidification (F, A) systems that are close to the border with the tie triangle, or two-phase solidification (FA, AF) systems that are far from the eutectic composition are susceptible to the peritectic reaction on the last melt fraction, present in interdendritic/intercellular regions. However, the three-phase reaction remains dominantly eutectic in character for the majority of two-phase solidification systems. Modeling the three-phase reaction is discussed on Chapter 4.

2.1.2. Kinetics, melt pool and morphology of the as-cast microstructure

As-cast microstructures are formed due to solidification and solid-state transformations. In welding and additive manufacturing, a moving heat source (e.g., electric-arc, EB, LB) fuses the material by melting and then solidification upon cooling. The three-dimensional space signified by the presence of the melt is called melt pool. The melt pool shape and location are

dynamic as it follows the path of the heat source. Using the Langragian specification of a moving observer that follows the heat source, the melt pool takes a non-axisymmetric three-dimensional shape that can be approximated by a semi double-ellipsoid [27] in the absence of intense mechanisms like the key-holing effect [28]. The boundary that defines the melt pool is called melt pool periphery, and constitutes the most remote locus of melt pool points, relatively to the position of the heat source. During solidification, the melt pool periphery is characterized by heat balance, with material closer to the heat source being cooled and the material beyond the melt pool periphery being heated. As a result, the melt pool periphery is characterized by the lowest temperature (by definition equal to liquidus) inside the melt pool, and thus it is where solidification commences. When the deposition material is chemically similar to the substrate -that is normally the case in welding and always in additive manufacturing- the primary solid forms according to a mechanism called epitaxial growth [29] which will be analyzed in Section 2.2.1. Presently the initial solidification stage is omitted, assuming that the transformation advances right away with a dendritic front as a result of constitutional supercooling ahead of the liquid/solid interface [30]. An illustration of the transverse section of the melt pool during dendritic solidification is presented in Figure 2.3(a). The melt pool is geometrically defined in the transverse section by a width ($w = 2a$) and a depth ($d = b$). The dendrites grow from the melt pool periphery, towards the spot of the heat source, in the direction of the local highest spatial temperature gradient. Furthermore, a polar system of coordinates, with a center at the heat source spot and counter-clockwise angular direction, is defined and employed throughout the present analysis, to aid in melt pool morphological characterization. From Figure 2.3(a) it is evident that for $a \approx b$ the microstructure exhibits angular symmetry as well. Notice that dendrites can also incline in the direction of the heat source movement, as illustrated in Figure 2.3(b), as the heat moving heat source changes the direction of heat flow and thus the final growth direction. Assuming a trajectorial coordinate system alongside the dendrite axis t^d and a polar coordinate system (r^d, θ^d) at the base of a dendrite, it is possible to describe the microstructural evolution during solidification. As the heat source travels at a constant velocity V equal to the printing/scanning speed, it establishes a steady state across the longitudinal direction and thus the representation of the entire microstructural evolution is reduced to studying a single dendrite of mean length (in case of single-phase solidification) or a neighboring couple of dendrites (for two-phase solidification), throughout the trajectorial coordinate t^d, including the equiaxed section, if any.

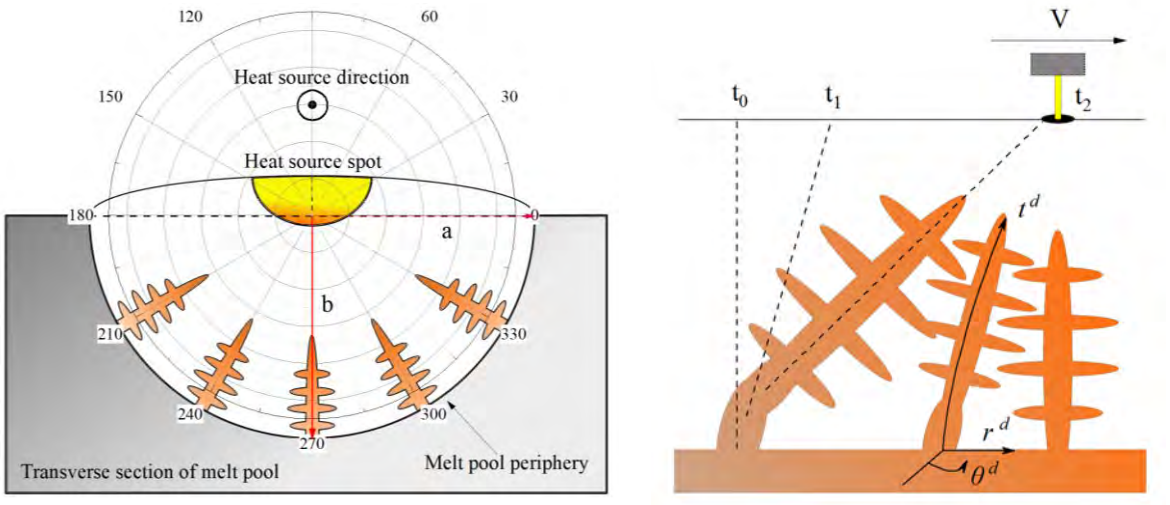

(a) (b)

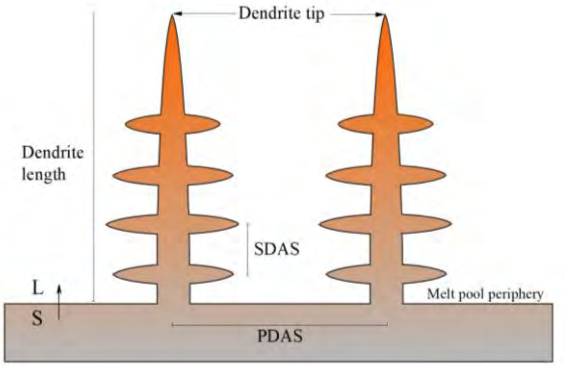

(c)

Figure 2.3. Dendritic solidification: (a) Transverse section of the melt pool ellipsoid and coordinate system, (b) Dendrite evolution in the longitudinal direction and (c) Geometry features of dendrites.

Geometrical features of dendrites are given in Figure 2.3(c). Dendrite length is the distance between the completely solidified moving periphery, and the dendrite tip. The region of the melt pool where dendritic solidification takes place is called mushy zone [30]. Solidification in austenitic stainless steel welds is a diffusive transformation, carried out with solute partitioning in the solid/liquid interface between the melt and both solid phases. Transformation kinetics are based on diffusion distances, and in association with cooling rate they control the development of microsegregation, the spatial evolution of concentration of alloying elements. In dendritic growth, the distance between primary dendrites (PDAS) and the distance between secondary dendrite arms (SDAS) are the principal diffusion distances. In cellular growth, where secondary dendrites have not been developed, microstructural evolution is controlled by diffusion occurring across the PDAS, while in columnar-dendritic growth, upon development of secondary dendrite arms, the transformation is control by diffusion across the SDAS. Flemings [30] reported that DAS depends on the cooling rate ($log\ \varepsilon$) in a linear fashion, through the determination of parameters a and n in the following expression:

$$\lambda_i = a\varepsilon^n \tag{2.1}$$

where $i = 1$ for PDAS, $i = 2$ for SDAS, λ_i is in (μm) and ε in (°C/s). Katayama and Matsunawa [31] determined the parameters from experimental measurements on a 55-Fe 310S austenitic stainless steel, given in Equations 2.2 and 2.3:

$$\lambda_1 = 80\varepsilon^{-0.33} \tag{2.2}$$

$$\lambda_2 = 25\varepsilon^{-0.28} \tag{2.3}$$

Choosing the appropriate diffusion distance for simulation of the microstructural evolution is a topic that will be further discussed on Chapter 4. Presently, the analysis suggests that development of microsegregation across PDAS accompanies the evolution primary dendrites (cellular microstructure) and synergistic segregation in PDAS and SDAS is present on columnar-dendritic microstructure upon evolution of secondary dendrite arms.

Inoue and Koseki [32] examined the crystallographic orientation of austenite and ferrite dendrites in FA type solidification, and reported absence of correlation, indicating that the eutectic character of the three-phase reaction refers to independent rather than restricted growth of dendrites. Hence, throughout the present study the term “eutectic” is used to describe the simultaneous independent growth of austenite and ferrite during solidification.

Thermodynamics through compositional dependance of the solidification mode (Cr_{eq}/Ni_{eq}) and kinetics via control of morphology and spatial/temporal evolution of phases and composition, determine the resulting as-cast microstructure. For low-cooling rate welding (up to $10^3 °C/s$ as in electric arc welding), schematic representations of typical obtained microstructures encountered in literature [13,14,31,33], are presented in Figure 2.4, for solidification modes F, FA, AF and A.

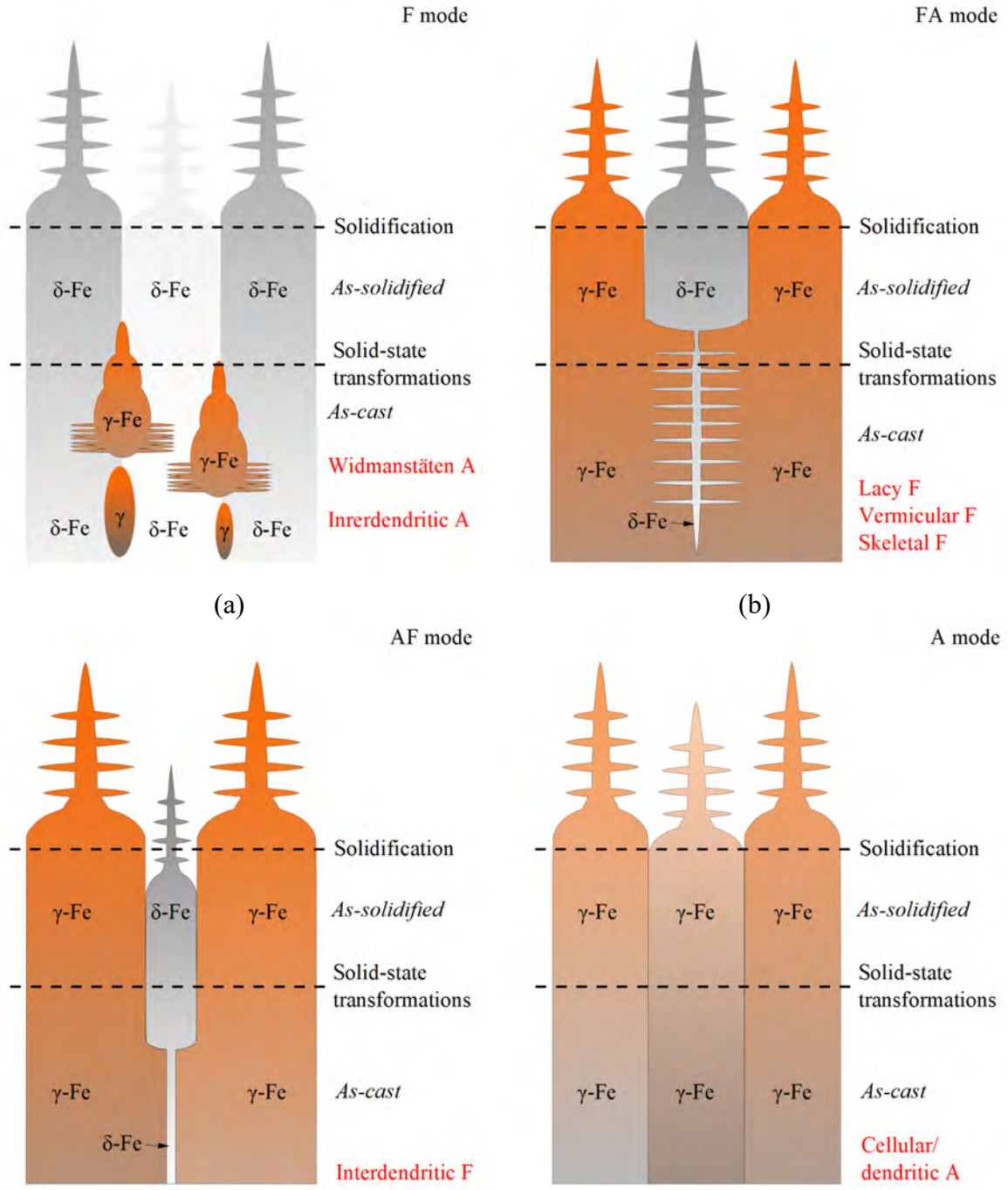

Figure 2.4. Schematic representation of the microstructural evolution per solidification mode in welding: (a) type F solidification, (b) type FA solidification, (c) type AF solidification and (d) type A solidification.

The eutectic E solidification type is omitted, as it principally resembles the microstructural evolution of AF and less of FA types for intermediate and high cooling rates (or rather FA, AF modes are characterized by the eutectic behavior), but in practice it rarely occurs.

The microstructural evolution of *F-type* solidification mode in low-cooling rate welds is presented in Figure 2.4(a). As-solidified microstructure consists of single δ-ferrite dendrites, divided by sub-grain boundaries (cellular morphology) or dendritic walls (columnar-dendritic morphology). In transverse section, the microstructure appears as cellular (array of cells arranged in a hexagonal mesh) and from viewing at an angle, dendrites appear as trapezoidal, rectangular or long laths [29,33]. Upon further cooling, the $\delta \rightarrow \gamma$ transformation initiates heterogeneously at the dendritic boundaries or cell walls, by a nucleation and growth mechanism, and austenite grows in morphology depending on the composition and cooling rate of the process, and its effect on solid-state transformations. At low/intermediate cooling rates, austenite forms at the sub-grain boundaries and grows as Widmanstäten platelets, while at low cooling rates austenite is present in the interdendritic/intercellular regions. Moreover, Inoue and Koseki [32]

During *FA-type* solidification, primary δ-ferrite and following austenite dendrites grow independently from the melt, according to the eutectic reaction, and the resulting as-solidified microstructure has a dual-phase character. As cooling progresses, $\delta \rightarrow \gamma$ transformation reduces the amount of ferrite, and the resulting morphology is again affected by the cooling rate, but this time effective on both the solidification and solid-state transformations stage. That is because solid-state growth depends on microsegregation, the spatial distribution of alloying elements during solidification and the transformation itself progresses according to solid-state kinetics. As will be discussed in Section 2.3, at low cooling rates, the microstructure is columnar-dendritic, described by the development of secondary arms. Segregation is therefore developed in both PDAS and SDAS, a situation that leads to preferential growth of austenite in regions where the last melt solidified (between secondary dendrite arms), that are rich in austenite-stabilizing elements, forming the morphology known as skeletal or vermicular δ-ferrite. Lacy F, an alternative morphology that is observed, can describe the same microstructural features as skeletal F, observed at an angle to the axis of reference as can be observed in experimental results by Yu et al. [25]. Inoue and Koseki [32] treating lacy and vermicular as different microstructures, established a relation between lacy/vermicular and the alignment of preferential growth direction, heat flow direction and relative crystallographic orientation at ferrite nucleation. Finally, Elmer et al. [29,33] reported the blocky austenite morphology for FA-type solidification with nearly 100% ferritic as-solidified microstructure, where nucleation of austenite was restricted at the grain boundaries and not between secondary dendrite arms, reducing the austenite/ferrite boundary area for solid-state transformation. The final microstructure is mostly ferritic, with allotriomorphs (blocks) of austenite in the interdendritic region.

The microstructural evolution of *AF-type* solidification mode at low cooling rate welds is presented in Figure 2.4(c). Solidification initiates with growth of austenite dendrites. Segregation of Cr in the interdendritic areas allows for the growth (epitaxial growth or nucleation and growth) of δ-ferrite dendrites, growing independently among austenite, in dendritic form as well. The as-solidified microstructure consists of austenite core dendrites, separated by walls of δ-ferrite. For the as-cast microstructure, the $\delta \rightarrow \gamma$ transformation reduces the ferritic amount even further and, in some cases, it can disappear altogether [31].

Finally, the microstructural evolution of *A-type* solidification mode at low cooling rate welds is presented in Figure 2.4(d). No ferrite is present in the as-solidified or as-cast microstructure, since it is not thermodynamically stable. The as-cast microstructure is composed of austenite dendrites, divided by subgrain boundaries or dendritic walls, similar to F-type solidification mode.

2.1.3. As-cast microstructure prediction tools

Investigation of solidification thermodynamics of the ternary Fe-Cr-Ni system provides information on the relationship between alloy composition and the solidification mode. However, austenitic stainless steels are in practice multi-component systems, containing additional alloying elements like C, Mo, Mn and Si, besides Cr and Ni, that alter the system thermodynamics in deviating from the ternary Cr/Ni ratio quantification. For that reason, equivalency relationships have been developed to substitute the preliminary Cr/Ni ratio (accurate in the ternary system Fe-Cr-Ni) in multi-component systems, where alloying additions can either promote austenite stabilization similar to the effect of Ni, or δ-ferrite stabilization similar to the effect of Cr. Ferrite-promoting elements, other than Cr, include Mo, Si, Nb, Al, Ti, V and W, whereas austenite-promoting elements, other than Ni, include C, Mn, N, Cu and Co [13]. In equivalency relationships the effect of additional phase-promoting elements is taken into account using weighted coefficients for every contributor. Determination of the coefficients relies on phenomenological investigation of the austenite/ferrite content in the as-cast microstructure (not the as-solidified), and thus equivalency relationships were linked from the early stages of their development to as-cast microstructure prediction tools for austenitic stainless-steel welds. Since the diagrams aim to predict only phase fraction values, morphology features and distribution of phases and alloying elements are omitted from those analyses. The most renowned diagrams include the Schaeffler diagram (1949 update) [34] , the DeLong diagram (1973) [35] and the WRC-1992 [36] which is still employed today as reference for most welding applications. The equivalency relationships developed for these tools are given in Table 2.3.

Table 2.3. Cr and Ni equivalency relationships for as-cast microstructure prediction.

As-cast prediction tool	Equivalency relationships (units in wt%)
Schaeffler diagram [34]	$Cr_{eq}^{Sch} = Cr + Mo + 1.5Si + 0.5Cb$ $Ni_{eq}^{Sch} = Ni + 30C + 0.5Mn$
DeLong diagram [35]	$Cr_{eq}^{DL} = Cr + Mo + 1.5Si + 0.5Cb$ $Ni_{eq}^{DL} = Ni + 30C + 30N + 0.5Mn$
WRC-1992 diagram [36]	$Cr_{eq}^{WRC} = Cr + Mo + 0.7Nb$ $Ni_{eq}^{WRC} = Ni + 35C + 20N + 0.25Cu$

All predictive tools aim to quantify the as-cast microstructure's ferrite content from the weld metal's composition, utilizing the developed equivalency relationships. The DeLong equivalency relationships have evolved directly from those of Schaeffler, only to account for the N trait in stabilizing austenite. The Schaeffler and WRC-1992 diagrams are presented in Figure 2.5. The Schaeffler diagram predicts directly the δ-ferrite volume fraction based on the weld metal composition, a demanding quantity to validate experimentally in terms of volume fraction measurements. For that purpose, the Ferrite Number (FN) scale was introduced in

DeLong and WRC diagrams, quantifying the magnetic behavior of welds in ambient temperature (where δ-ferrite is ferromagnetic while austenite is paramagnetic), and while not directly proportional to ferrite volume fraction, there is good agreement for values under 10 vol%. Notice that the as-cast ferrite content is always less than the as-solidified, regardless of solidification mode, because after solidification, the solid-state $\delta \rightarrow \gamma$ transformation always takes place. In Figure 2.5(b) an experimental identification of the solidification mode limits (red-dotted lines) is attempted based on the as-cast ferrite content.

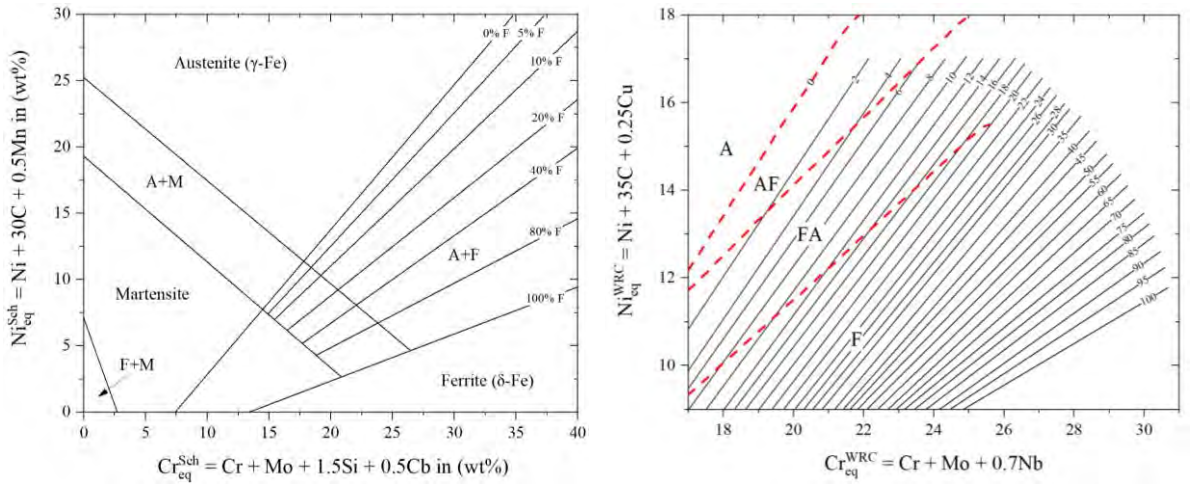

(a) (b)

Figure 2.5. Prediction diagrams for the as-cast microstructure of austenitic stainless steels: (a)The Schaeffler diagram and (b) the WRC-1992 diagram.

The Schaeffler diagram can make microstructural estimations from the Fe-rich corner of the system and involves evolution of martensite as well, while the WRC-1992 focuses on the austenite/ferrite two-phase system, proposing constitutional limits to differentiate among the solidification modes, both primary (PSM) and total (TSM). The WRC-1992 diagram can be employed for the validation of models that predict the microstructural evolution in electric-arc welding. Despite being accurate for as-cast estimations, it is impossible through employment of composition tools to predict the microstructural evolution in-situ, differentiate between solidification and solid-state transformation effects, and measure temporal and spatial distribution of phases and alloying elements. In addition, the effect of cooling rate and microstructural morphology are not taken into account, and thus the accuracy and results range of the prediction is restricted, not only for related processes like additive manufacturing, but in welding as well, since application on a reference system for electric-arc welds and laser beam welds cannot have the same microstructural results [29]. A useful observation is that in multi-component systems, Cr_{eq}/Ni_{eq} ratio can be employed to accurately represent the system's thermodynamics and classify the solidification mode [37].

2.2. Effect of the cooling rate

Welding and additive manufacturing are processes carried out under far-from-equilibrium conditions. Cooling rate (G) is the most important controllable process parameter affecting transformation kinetics and diffusion throughout microstructural evolution. Table 2.4 contains some typical cooling rate estimation ranges for several processes [29]. The cooling rate is determined by how efficiently the melt pool can dissipate the absorbed energy from the heat source and latent heat of the solidifying material. Heat is outfluxed from the melt pool via two main routes: (a) Conduction from the melt pool periphery towards the solid material substrate

and (b) Convection-radiation from the free surface of the melt pool towards the surrounding environment. Classification of cooling rates as low from 10^0 to 10^3 °C/s, as intermediate from 10^3 to 10^5 °C/s and as high from 10^5 °C/s and above is applied.

Table 2.4. Indicative cooling rate ranges for solidification-involving processes [29].

Process	Cooling rate (°C/s)
Directional solidification	10^{-1} to 10^1
Casting	10^0 to 10^2
Arc welding	10^1 to 10^3
EB welding	10^2 to 10^4
LB welding	10^2 to 10^6
Additive manufacturing	10^3 to 10^7
Rapid solidification processing	10^4 to 10^7

The effect of cooling rate on the microstructural development during solidification of stainless steel alloys was studied by Elmer [29,33]. There are three key points on how the cooling rate affects solidification. The first effect concerns the morphology of the dendrites, as by increasing the cooling rate, the columnar-dendritic shape is suppressed in favor of the transverse growth of primary dendrites. Columnar-dendritic microstructures give place to cellular morphologies. Note that cellular and columnar-dendritic are two terms referring to separate morphologies, depending on the presence of secondary dendrite arms. This transition affects solid-state transformation morphologies as well, as the intercolumnar character of the secondary phase (austenite in FA and δ-ferrite in AF) changes into intercellular.

The second effect impacts the kinetics of solid-state transformations. As the cooling rate increases, solute diffusion in the solid decreases and thus solid-state transformations are delayed or inhibited. For alloys with low Cr/Ni ratios that solidify with primary austenite, the as-cast ferrite content increases with cooling rate, as the $\delta \rightarrow \gamma$ kinetics are retarded, while for alloys with high Cr/Ni ratios that solidify with primary ferrite, as-cast ferrite content increases with cooling rate, as nucleation and growth kinetics of austenite are impeded. Finally, the third and most important effect, addresses the solidification behavior and will be discussed in Section 2.2.2, after the presentation of epitaxial growth, the initiating mechanism of solidification in welding and additive manufacturing.

2.2.1. Epitaxial growth

Solidification in casting initiates on the mold surface, where the melt temperature is the lowest. Molds are made from a variety of materials that usually do not have any chemical relationship with the cast material in order to achieve quality casting as well as protect the mold surfaces and solidification initiates with nucleation and growth of randomly oriented crystals (with the exception of directional and single crystal solidification). Solidification of the first grains in casting begins with nucleation and growth on the mold surface, and microstructural evolution proceeds according to the theory described in Section 2.1. However, in welding and additive manufacturing, nucleation and growth is not typically the solidification main initiation mechanism. Due to the nature of these processes, the material substrate in contact with the melt, either has similar composition, phase and structure (welding metallic components with electrodes made of similar alloy composition) or is exactly the same system. Under this condition, solidification commences directly from grains already present on the melt pool

periphery, a phenomenon called epitaxial growth. The first solidified layer on the melt pool periphery is identical to the substrate, as the existing microstructure keeps on growing and solidification proceeds with a planar front and not a dendritic one, due to the growth rate (R) approaching zero. Elmer et al. [29,33] examined epitaxial growth under variance of the cooling rate and determined that while epitaxial growth is present under all conditions, the width of the plane-front layer, decreases with the cooling rate, ranging from 10μm for low cooling rates, to $< 1\mu m$ for high cooling rates. This area fraction is not important in relation to the rest of the solidified volume, but is an important feature because from it grow all crystals in the melt, changing the thermodynamics of the system by enabling growth of metastable phases that can influence the primary solidification mode.

2.2.2. Competitive growth and primary solidification mode

Immediately after the plane-front layer, random disruptions on the solidification interface result in transition to a cellular solidification front, with nucleation of new dendrites and growth of existing ones [29,33]. In that stage, dendrites compete to outgrow their neighbors in claiming the progressively decreasing space towards the heat source spot. The direction of dendrites is not perfectly perpendicular to the plane-front periphery, since their core axis is influenced by crystal growth relationships (like the K-S relationship [26]) in addition to the spatial temperature gradient and the local composition gradient. Growth velocity is determined by diffusion and thus it depends on the cooling rate [38]. Competitive growth can alter the solidification mode via two mechanisms. Illustrations of competitive growth mechanisms that change the solidification mode are presented in Figure 2.6.

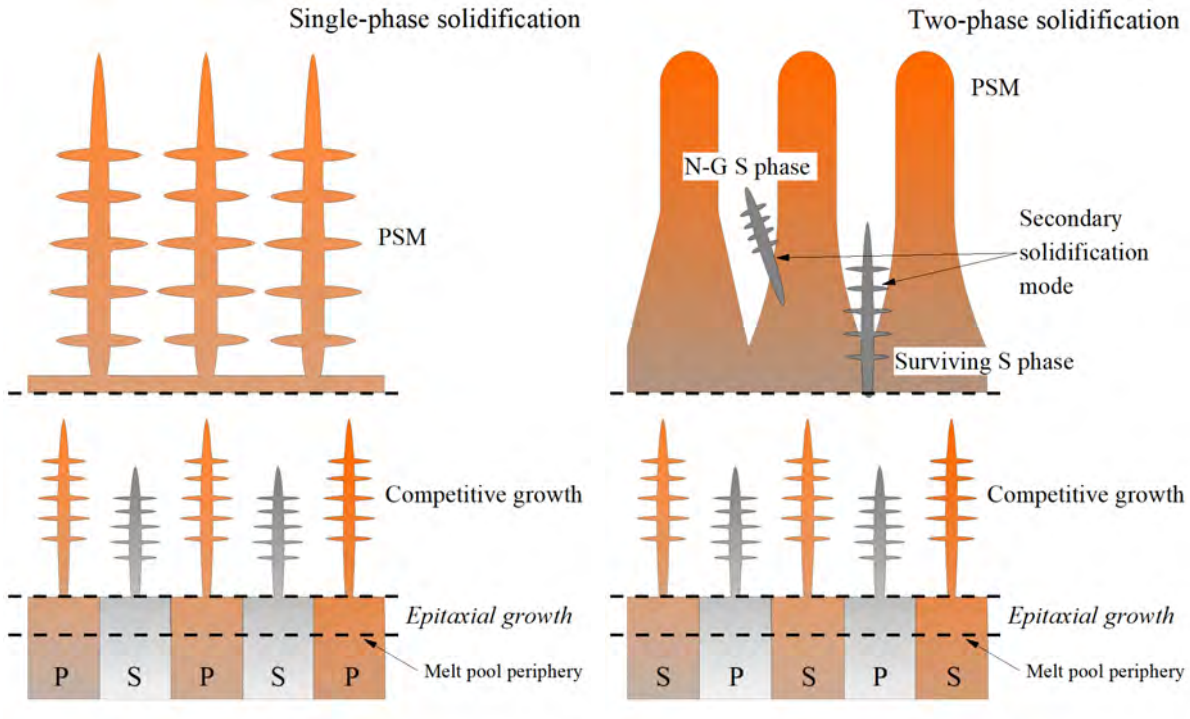

(a) (b)

Figure 2.6. Epitaxial and competitive growth in solidification: (a) Single-phase solidification mechanism and (b) two-phase solidification mechanisms.

In single-phase solidification (types A, F) epitaxial and competitive growth do not affect the phase contents of the solidified material, since only a single dendrite phase is present. However,

in two-phase solidification (types AF, FA), epitaxial growth enables and competitive growth enacts the possibility to change the solidification mode as the cooling rate increases [29]. In order to study that effect, the substrate is assumed to contain equal amounts of austenite and ferrite, since competitive growth is affected by the epitaxially grown substrate content, although Mas et al. [39] reported that change in the solidification mode can occur from small secondary phase fractions.

The first competitive growth mechanism changes the solidification mode from two-phase into single-phase type as presented in Figure 2.6(a). Epitaxially grown dendrites of the equilibrium primary (P) and secondary (S) solidification phases compete under an increased cooling rate to determine the non-equilibrium primary solidification mode. For either high or low Cr/Ni ratios respectively, the driving force for the growth of equilibrium primary austenite or δ-ferrite respectively, promotes sufficient evolution of their corresponding dendrites -a superstable primary phase- to obstruct completely the evolution of secondary phase dendrites. Microstructural evolution continues with the growth of single-phase equilibrium-primary dendrites, determining the effective primary solidification mode. This mechanism is applied on two cases: transition of FA mode to F and transition of AF mode to A, pictured in Figure 2.7(a).

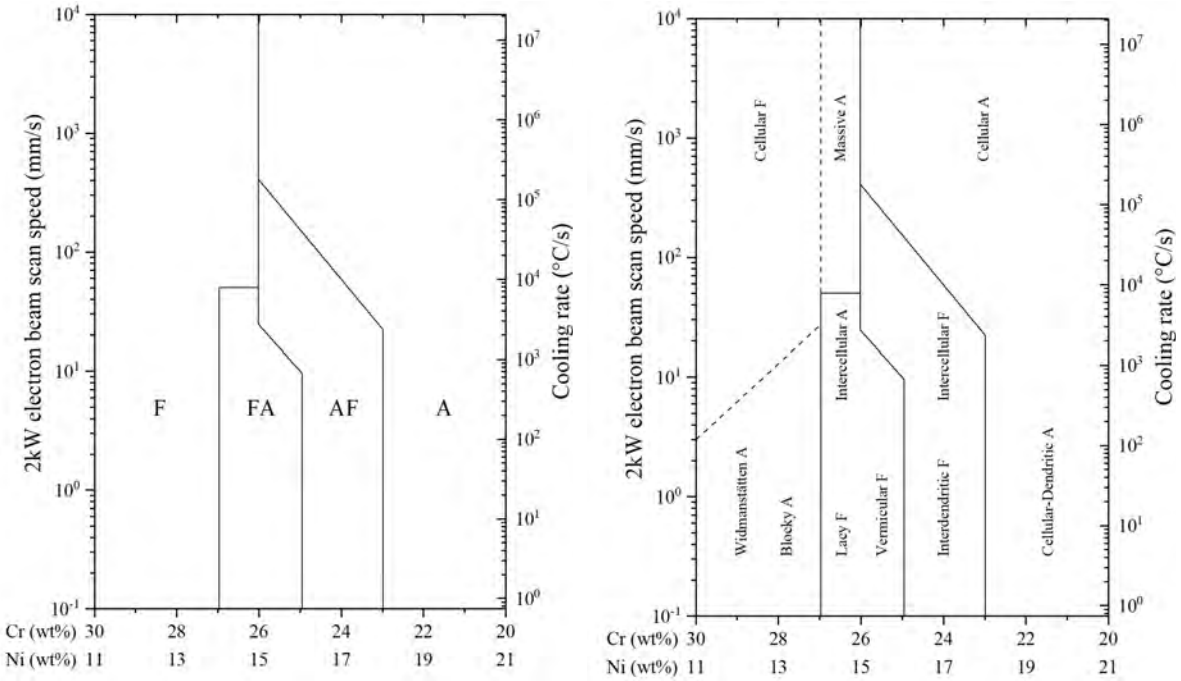

(a) (b)

Figure 2.7. Microstructure maps that describe the influence of cooling rate and composition: (a) Evolution of the solidification mode map and (b) map of microstructural formations [29].

The second competitive growth mechanism changes the primary solidification mode between two-solidification type systems, and is illustrated in Figure 2.6(b). High cooling rates promote the epitaxially grown equilibrium-secondary phase dendrites to outgrow the equilibrium-primary phase. This transition is attributed to reinforcement of the driving force of the secondary phase due to metastable growth kinetics at high cooling rates that enables thermodynamic override of low-cooling rate kinetics. Thus, the equilibrium-secondary phase becomes the primary solidification phase, defining the PSM. However, the suppressed phase can manage to be present in the as-solidified microstructure, either by surviving the PSM

dendritic growth due to thermodynamic stability, or by nucleation and growth on the primary phase dendrites, due to cooling rate decrease as the solidification front approaches the heat source. The second competitive growth mechanism is effective in one case; transition of FA mode to AF mode, pictured in Figure 2.7(a).

Based on the discussed competitive growth mechanisms, Elmer et al. [29,33] created the qualitative diagram of Figure 2.7(a), describing the dependence of solidification mode of the ternary Fe-Cr-Ni system to the cooling rate. The vertical axis of the original diagram of Figure 2.7(a) [29] reflects the analogy between increase in cooling rate and welding source velocity. A complementary cooling rate axis was added based on the provided experimental measurements [29]. At low cooling rates, solidification mode is only determined by the system thermodynamics, thus the transition Cr/Ni ratios from F to FA, from FA to AF and from AF to A solidification mode coincide with $(Cr/Ni)^{\delta-sat}$, $(Cr/Ni)^{e}$ and $(Cr/Ni)^{\gamma-sat}$ of Figure 2.1 respectively. As the cooling rate increases, the described competitive growth mechanisms change the solidification mode at three cases. Changes FA→F and AF→A occur due to the first competitive growth mechanism, where the equilibrium-primary phase becomes superstable with limited diffusion. Change FA→AF occurs due to the second competitive growth mechanism, where metastable austenite dendrites dominate equilibrium-primary δ-ferrite dendrites, changing the PSM. Inoue and Koseki [32]captured experimentally this transition changing the PSM with decreasing cooling rate, as solidification progressed inside the melt pool. From Figure 2.7(a) it is evident that systems that exhibit FA mode at low cooling rates can solidify either with F or with A mode at high cooling rates. That is because certain systems close to the eutectic system, solidifying as FA at low cooling rates undergo two solidification mode transitions: FA→AF→A as the cooling rate increases.

The solidification mode transitions were verified experimentally [29,33] and the corresponding microstructure and their compositional and cooling rate dependence are presented in Figure 2.7(b), exhibiting all three effects of the cooling rate on the microstructure. From low to intermediate cooling rates, morphological changes take place from a columnar-dendritic to a cellular microstructure, that combined with limited solid-state transformations, result in development of intercellular morphologies with reduced secondary phase fractions. From intermediate to high cooling rates, competitive growth transition mechanisms in solidification mode are effective, resulting in single-phase cellular morphology solidification of either austenite or ferrite, depending on the PSM, the determination of which will be discussed in Section 2.3. The case of low Cr/Ni FA-type solidification presents special behavior, since above intermediate cooling rates it solidifies with single ferrite, however, below solidus temperature the system undergoes a massive $\delta \rightarrow \gamma$ transformation, resulting in the development of a single-massive austenite microstructure (austenite that retains the microstructural features of ferrite via an interface-controlled transformation) [40].

Employing information from the diagrams of Figure 2.7 [29], in addition to [41–43], Lippold [38] composed a microstructural map of the solidification mode as a function of the solidification/growth rate (R), given in Figure 2.8. Similar to Figure 2.7(a), there are solidification mode transitions with increasing solidification rate, however Figure 2.8 provides a more accurate tool to describe the transition boundaries since it incorporates the effect of the Suutala diagram [43]. A significant addition is the mapping of the region dominated by the massive $\delta \rightarrow \gamma$ transformation, discovering two additional system cases. The first case concern systems that at low cooling rates solidify with FA mode and as the solidification rate increases,

initiate the massive transformation according to the behavior described in Figure 2.7(b). However, at lower Cr/Ni ratios, the diagram of Figure 2.8 predicts the interruption of the massive transformation to enter an AF solidification mode mechanism, before culminating in A mode solidification at even higher rates. Therefore, there is an intervention of massive transformation region in-between the transition FA→AF. The second system case corresponds to F solidification mode systems that besides high Cr/Ni FA mode systems, can lead to massive transformation as well, as the solidification rate increases. In contrast to the statement of [38], the cooling rate regulates the solidification/growth rate, since it affects diffusion and not vice versa. Therefore, the importance of Figure 2.8 resides in its ability to validate retrospectively the model selection (as will be discussed in Chapter 4); starting from the map of Figure 2.7(a) and solving the microstructural evolution problem, to calculate the solidification rate and proceed to verify the predicted solidification mode from Figure 2.8.

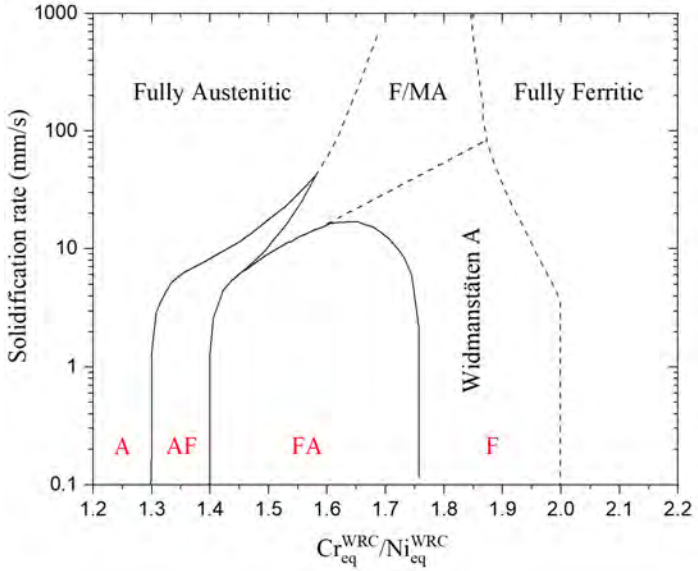

Figure 2.8. Preliminary microstructural map of austenitic stainless steel welds as a function of solidification growth rate. Derived from [29,41–43].

2.3. Dendrite growth theory

In Section 2.2, the maps of Elmer [29] provided the basis to predict the solidification mode and the resulting microstructure on the ternary Fe-Cr-Ni system, from the process cooling rate and the alloy composition. The mechanisms that change the solidification mode were analyzed qualitatively. However, this approach omits morphology transitions across the melt pool, electing a dominant microstructural feature in Figure 2.7(b) for each case. Moreover, in order to apply the solidification mode calculations in multi-component systems, growth of metastable austenite must be related to alloy composition. The KGT dendrite growth theory developed by Trivedi et al. [44,45] is widely employed to investigate the effect of solid-front morphology to solidification behavior and predict the morphology transitions across the melt pool. Primary solidification mode in multi-component systems can also be determined based on competitive dendrite growth of the solidifying phases.

2.3.1. Morphology transition

According to Kurz-Trivedi-Giovanola (KGT) dendrite growth theory [45], the morphology of the solidification front is quantified in relationship to spatial thermal gradient (G) and liquid/solid interfacial velocity (V). For a given G, increase of the interfacial velocity (V) leads

to microstructural transition following the morphological array presented in Figure 2.9. At very low interfacial velocities (infinite diffusion), there is absence of constitutional undercooling and solidification proceeds with planar front. As the cooling rate -and thus interfacial velocity- increases constitutional undercooling becomes effective and dendrites form, first with primary and then secondary arms, defining the cellular and dendritic microstructures. At even higher interfacial velocities, diffusion is significantly influenced, inhibiting secondary and progressively primary dendrite arms to form, leading to cellular and finally a planar solidification front morphology that is often referred to as metallic glass. The present study is concerned with the dendritic to cellular at high velocities and columnar to equiaxed transitions, since only these have been experimentally observed in welding and additive manufacturing [46,47]. The interfacial velocity affects the temperature at the solid/liquid interface, represented by the dendrite tip. KGT theory focuses on determining the dendrite tip undercooling ΔT_{tip} in order to compute the dendrite tip temperature T_d :

$$T_d = T_L - \Delta T_{tip} \tag{2.4}$$

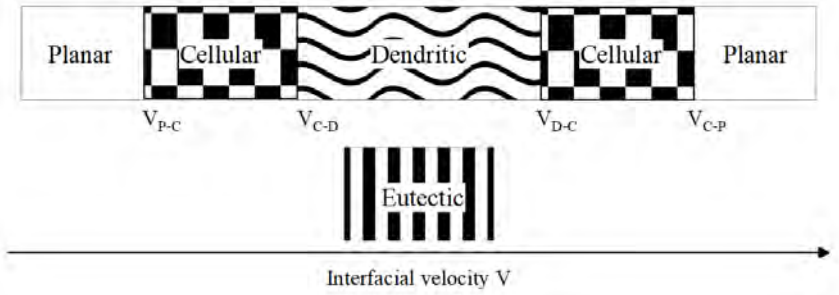

Figure 2.9. Interfacial front morphology evolution with growth velocity.

Kurz and Trivedi [45] determined an expression for dendritic ΔT_t on directional solidification under rapid cooling conditions, as applied in welding and additive manufacturing:

$$\Delta T_t = \sum_i \left(\frac{k_i^v \Delta T_{0,i}^v Iv(Pe_d)}{1-(1-k_i^v)Iv(Pe_d)} + C_{0,i}(m_i - m_i^v) + \frac{V}{\mu_{k,i}} \right) + \frac{2\Gamma}{R} + \frac{GD}{V} \tag{2.5}$$

where:

$$m_i^v = m_i \left(1 + \frac{k_i - k_i^v \left(1 - \ln\left(\frac{k_i^v}{k_i} \right) \right)}{1 - k_i} \right) \tag{2.6}$$

$$k_i^v = \frac{k_i + Pe_i}{1 + Pe_i} \tag{2.7}$$

$$\mu_{k,i} \approx \frac{V_0(1-k_i)}{m_i} \tag{2.8}$$

$$Pe_i = \frac{a_0 V}{D} \tag{2.9}$$

m_i^v is the liquidus slope, k_i^v the equilibrium partition coefficient, $\mu_{k,i}$ the interface kinetic coefficient for element i, and Pe_i the interfacial Péclet solute redistribution number for element i. Moreover, V_0 is the speed of sound in pure solid-state iron, Γ is the Gibbs-Thompson coefficient, a_0 is the solid/liquid interfacial diffuse layer thickness and D is the solute diffusion

coefficient in liquid, assuming negligible solid-state diffusion. The index v is used to imply growth velocity dependance. The non-equilibrium freezing range $\Delta T_{0,i}^{v}$ is:

$$\Delta T_0^v = \sum_i \frac{m_i^v C_{0,i}(k_i^v - 1)}{k_i^v} \tag{2.10}$$

Solution of Equation 2.5 is based on the temperature field around cylindrical/plate crystal, proposed by Ivantsov [48]. Hence the Ivantsov function $Iv(Pe_d)$ is calculated from:

$$Iv(Pe_d) = \begin{cases} \sqrt{\pi Pe_d}, & for\ Pe_d \ll 1 \\ 1 - \dfrac{1}{2Pe_d} + \dfrac{3}{4Pe_d^2}, & for\ Pe_d \gg 1 \end{cases} \tag{2.11}$$

where:

$$Pe_d = \frac{RV}{2D} \tag{2.12}$$

The dendrite tip radius R, is calculated according to [49]:

$$R = \sqrt{\frac{\Gamma}{\sigma^*(\sum_i m_i G_{c,i}\xi_{d,i} - G)}} \tag{2.13}$$

$G_{c,i}$ is the solute concentration gradient ahead of the dendrite tip, σ^* is the dendrite tip selection parameter, assumed to be constant for a reference alloy system and $\xi_{d,i}$ is the equilibrium deviation parameter, where:

$$G_{c,i} = \frac{(C_{t,i} - C_{0,i})V}{D \cdot Iv(Pe_d)} \tag{2.14}$$

$$C_{t,i} = \frac{C_{0,i}}{1 - (1 - k_i^v)Iv(Pe_d)} \tag{2.15}$$

$$\xi_{d,i} = 1 - \frac{2k_i^v}{\sqrt{1 + \dfrac{1}{\sigma^* Pe_d^2}} - 1 + 2k_i^v} \tag{2.16}$$

with $C_{t,i}$ being the dendrite tip composition.

The criterion for cellular/dendritic transition at high velocities, as illustrated in Figure 2.9, defines the critical cooling rate transition between intercellular and intercolumnar microstructures, as seen in Figure 2.7(b), is given by the expression:

$$V_{D-C} = \sum_i \frac{GD}{\Delta T_{0,i}}(1 - (1 - k_i)Iv(Pe_d)) \tag{2.17}$$

The second morphological change of interest is the Columnar to Equiaxed Transition (CET). From [50,51] a criterion relating the spatial thermal gradient G to the extended volume fraction of equiaxed grains φ:

$$G = \frac{1}{1+n}\sqrt[3]{\frac{-4\pi N_0}{3\ln(1-\varphi)}}\Delta T_t\left(1-\frac{\Delta T_n^{n+1}}{\Delta T^{n+1}}\right) \tag{2.18}$$

where N_0 is the equiaxed nucleant volume density ΔT_n is the nucleation undercooling for equiaxed grains and n is a material constant. CET is determined by the following criterion:

$$If\ \varphi\ is \begin{cases} < 0.0066 \rightarrow fully\ columnar - dendritic \\ > 0.066\ and < 0.49 \rightarrow mixed\ morphology \\ > 0.49 \rightarrow fully\ equiaxed - dendritic \end{cases} \tag{2.19}$$

Some thermodynamic and kinetic information, useful for dendritic growth models in Fe-Cr-Ni systems are provided by Löser and Herlach [52].

2.3.2. Metastable growth and primary solidification mode

The KGT dendrite growth theory was applied in the previous section to define criteria for morphological transitions. However, a KGT-based investigation was followed by Sutton [19] to study the evolution of metastable austenite dendrites via the interface response approach, in order to determine a solidification mode transition criterion at high cooling rates. Dendrite tip temperatures T_γ^* for austenite and T_δ^* δ-ferrite are calculated as a function of the interfacial velocity, presented in Figure 2.10 [19].

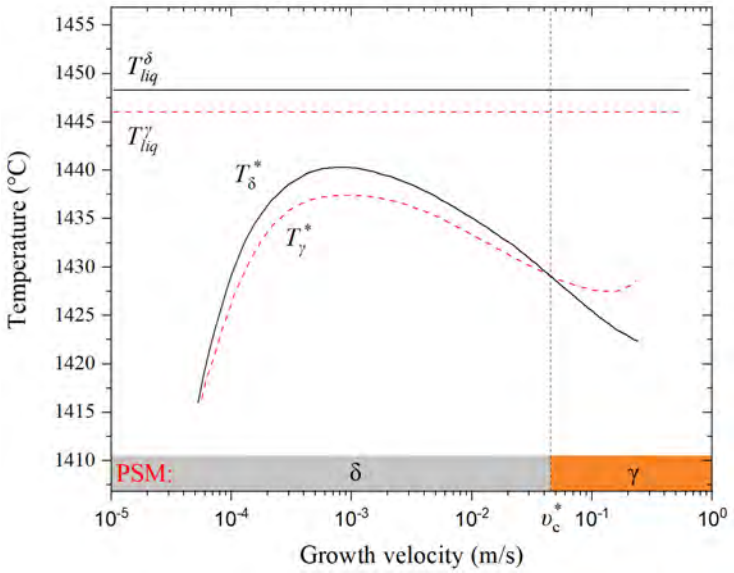

Figure 2.10. Relationship between growth velocity V and dendrite tip temperature for δ-ferrite and austenite, showing metastable austenite growth at high velocities, for a Fe-Cr-Ni stainless steel, at constant G=400°C/mm, from Sutton et al. [19,49].

In austenitic stainless steel systems that exhibit two-phase solidification, at low and intermediate interfacial velocities $T_\delta^* > T_\gamma^*$ and thus the bath undercooling needed for ferrite dendrites is lower than austenite leading to an advantage of ferrite during competitive growth. However, after a critical growth velocity v_c^*, growth of metastable austenite is favored since it requires reduced undercooling for elevated dendrite tip temperature. Combined with high cooling rates, the dendrite tip temperature controls the PSM and thus the solidification mode. A primary solidification mode diagram was developed by determining dendrite tip temperatures from a multi-component KGT model on reference austenitic stainless steel

systems and calibrating from experimental data. The PSM diagram of Sutton [19], is presented in Figure 2.11. The PSM diagram can be used to determine the A→F transition boundary under high cooling rates, in accordance with the solidification mode map of Figure 2.7(a) by Elmer et al. [29] for multi-component systems.

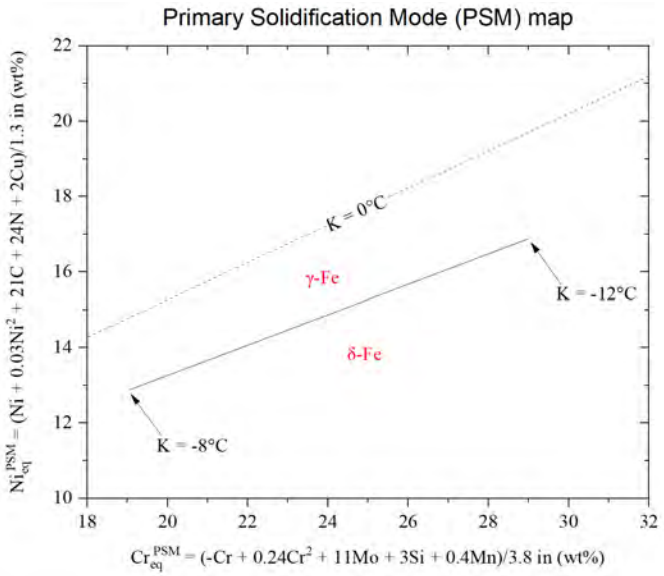

Figure 2.11. Primary Solidification Mode (PSM) diagram [19].

Sutton [19] employed a multiple regression model to assess the relationship between solidification freezing range and solidification sequence, developing equivalency expressions suited to predict the PSM, given in Equations 2.20-2.21:

$$Cr_{eq}^{PSM} = \frac{-Cr + 0.24Cr^2 + 11Mo + 3Si + 0.4Mn}{3.8}, in\ (wt\%) \tag{2.20}$$

$$Ni_{eq}^{PSM} = \frac{Ni + 0.03Ni^2 + 21C + 24N + 2Cu}{1.3}, in\ (wt\%) \tag{2.21}$$

Equations 2.20 and 2.21 determine a system's relative position to the critical PSM boundary of Figure 2.11, that in high cooling rates designates the fully ferritic from the fully austenitic microstructure. Variable K is a correction factor, adjusted to fit the PSM boundary to the experimental observations.

Chapter 3. Heat transfer analysis of additive manufacturing

3.1. Elements of heat transfer

In Chapter 2, many parameters referring to the spatial or temporal temperature evolution were analyzed, as the cooling rate R, the growth rate G and the velocity of the heat source V, important for controlling the microstructural evolution. It is thus evident that knowledge of the temperature behavior is required to study the microstructure of additive manufacturing products. In addition, accurate in-situ experimental measurements are demanding if not impossible to acquire and require specialized techniques and expensive equipment, since heating and cooling are rapid and the process involves phase changes in very high temperatures, yielding accurate results only for surface temperature measurements. Calculation of the spatial and temporal temperature profiles requires solution of the integral energy balance of Equation 3.1 [53]:

$$\int_{\Omega} \rho \dot{U} dV = \int_{\partial\Omega} -\boldsymbol{q} \cdot \boldsymbol{n}\, dS + \int_{\Omega} \rho \dot{r}\, dV\,, \forall\, \Omega \Rightarrow \int_{\Omega} \left(\rho \dot{U} + \nabla \cdot \boldsymbol{q} - \rho \dot{r}\right) dV = 0,\ \forall\, \Omega \tag{3.1}$$

$$\rho \dot{U} + \nabla \cdot \boldsymbol{q} - \rho \dot{r} = 0 \tag{3.2}$$

where Ω is the space that is occupied by the material, $\partial\Omega$ is the boundary of space Ω, ρ the material density in kg/m^3, U the internal energy per unit mass in J/kg, $\boldsymbol{q}$ the heat flux in W/m^2, $\boldsymbol{n}$ the outward unit normal vector to boundary $\partial\Omega$ and r the internal heat generation rate per unit volume in J/kg. Changes in internal energy can be expressed by definition in terms of specific heat $c(T)$ in $J/kg/$℃:

$$\dot{U} = \frac{\partial U(T)}{\partial T} \dot{T} = c\, \dot{T} \tag{3.3}$$

Applying the isotropic Fourier low and accounting for internal energy changes $\dot{U}_l$ due to phase changes in the material, provide the governing equation for transient heat transfer analysis:

$$\nabla \cdot (\boldsymbol{k} \cdot \nabla T) + \rho(\dot{r} - \dot{U}_l) = \rho\, c\, \dot{T} \tag{3.4}$$

with $\dot{U}_l > 0$ in melting and $\dot{U}_l < 0$ in solidification. The latent heat U_L is calculated from Equation 3.5:

$$U_L = \int_{T_S}^{T_L} \dot{U}_l(T)\, dT \tag{3.5}$$

For a homogeneous and isotropic material, $\boldsymbol{k} = k\boldsymbol{\delta}$, transforming Equation 3.4 in the Fourier-Biot of Equation 3.6:

$$\mathrm{k}\, \nabla^2 T + \rho(\dot{r} - \dot{U}_l) = \rho\, c\, \dot{T} \tag{3.6}$$

Heat transfer from a material point is carried out via conduction with the substrate material or powder particles, via natural or forced convection with the atmosphere or via radiation. The mixed convection radiation boundary condition is given in Equation 3.7:

$$\boldsymbol{q} \cdot \boldsymbol{n} = -h(T - T_0) - \sigma\varepsilon[(T - T_z)^4 - (T_0 - T_z)^4] \tag{3.7}$$

where h is the convection film coefficient in $W/m^2/°C$, T_0 the sink temperature T_z the reference temperature (absolute zero), ε the material radiation emissivity and $\sigma = 5.669 \times 10^{-8}\ W/m^2/°C$ is the Stefan-Boltzmann constant.

3.2. Modeling heat transfer in additive manufacturing

In the present chapter, a heat transfer model is developed based on a Finite Element Methodology (FEM), implemented in ABAQUS [54] a general-purpose finite element software, aiming to predict the temperature evolution in additive manufacturing processes. The model considers printing of a 1.5x1.5 mm 2D rectangular wall following a unidirectional scanning strategy (right to left) and heat transfer calculations were carried out in UMATHT user subroutine. The heat source of the laser beam, the latent heat effects, as well as the heat losses due to convection and radiation were modeled via the DFLUX user subroutine in ABAQUS. Thermal analysis employed two-dimensional diffusive heat transfer elements (DC2D4) to evaluate the temperature evolution due to successive material deposition with dimensions close to the layer thickness value, in order to capture the melt pool.

Laser velocity was taken equal to $u = 675\ mm/s$, power $P = 100\ W$, layer thickness 0.02 mm, chamber temperature T_∞=27°C and idle time 10 s between consecutive passes. Meshing in square elements with 4 nodes each and sides $DX = DY = 0.02\ mm$ was carried out to be specifically equal to the layer thickness of the printing process. Melt pool depth in AM processes must exceed the layer thickness in order to achieve incorporation, but only slightly for efficient material deposition. Consequently, choosing an element height to be equal to the layer thickness implies that the temperature on the bottom nodes of the elements representing material deposition, must reach values over but close to the liquidus temperature. Therefore, the model is restricted by the resulting temperature evolution and can be calibrated accordingly.

To evaluate the transient temperature evolution, the model requires information regarding the thermophysical properties of the material, namely thermal conductivity k, specific heat c_p, density ρ and latent heat U_L. The accuracy level of the results depends on the precision and realism of the employed non-equilibrium thermophysical properties, that can range from equilibrium [55] (as a first-degree approximation) to rapid solidification calculations. In this approach, all thermophysical properties are temperature and microstructure depended, implemented via the KMATPROP subroutine in ABAQUS. The calculated temperature-dependent thermophysical properties for the reference 316L system are given in Figure 3.1.

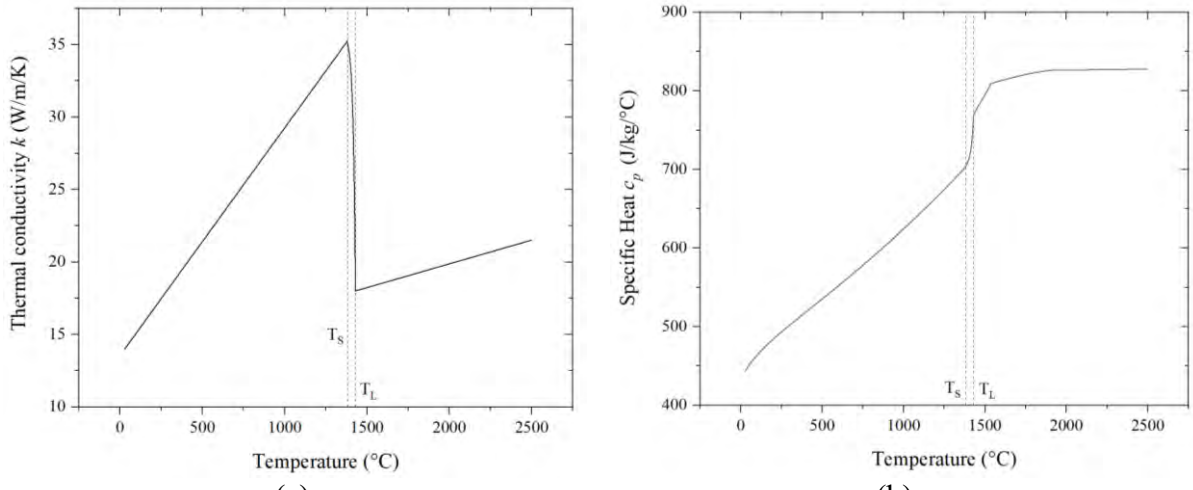

(a) (b)

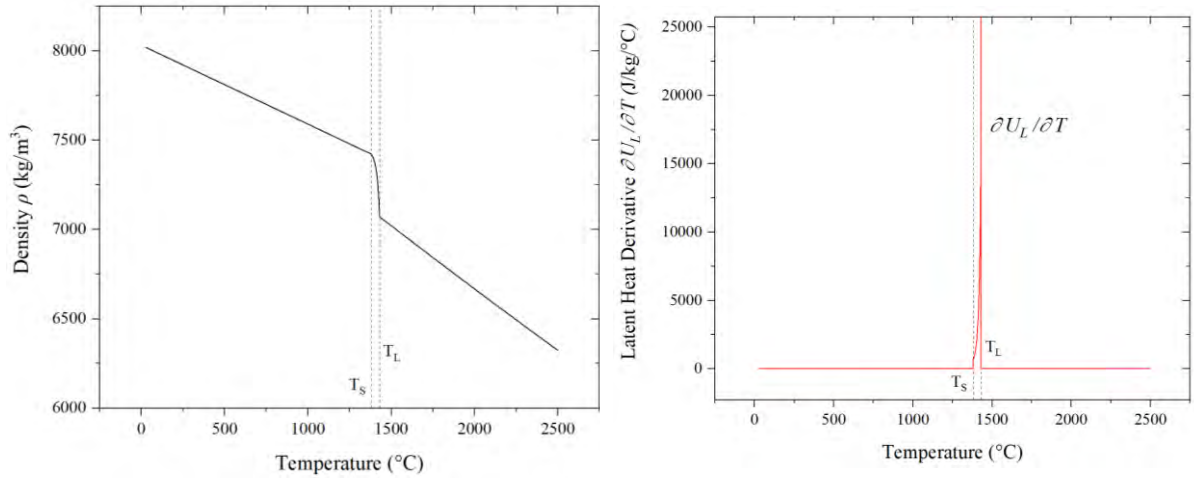

(c) (d)

Figure 3.1. Thermophysical properties of the reference 316L: (a) Thermal conductivity k, (b) specific heat capacity c_p, (c) density ρ and (d) Latent heat temperature derivative.

Latent heat of solidification is calculated from Figure 3.1(d), via numerical integration of the temperature derivative to be $U_L = 1976.65\ kJ/kg$. Notice that presently information on the thermophysical properties is considered given. Analysis on the calculation of non-equilibrium thermophysical properties is carried out in Chapter 4.

Material deposition was modeled based on the quiet element methodology, as described by Michaleris [56]. The elements are present but are assigned properties, so that they do not affect the analysis. More specifically the thermal conductivity k and the specific heat c are set to zero, minimizing conduction to adjust energy transfer through the quiet elements:

$$k_{quiet} = c_{quiet} = 0 \tag{3.8}$$

The element activation process, both as powder and solid material is described by Koimtzidis [57] for a unidirectional scanning strategy. Further research on the effects of scanning strategy would require three-dimensional implementation. The moving heat source was modeled as the longitudinal two-dimensional analog of a simple ellipsoid volumetric heat input, as presented in Figure 3.2, reduced from the double ellipsoid of Goldak et al. [27] for $\alpha_1 = \alpha_2$:

$$\rho\dot{r} = \frac{6PF}{\pi ab} e^{-3\left[\left(\frac{\xi}{a}\right)^2 + \left(\frac{\eta}{b}\right)^2\right]} \tag{3.9}$$

where r ($\dot{r} = \dot{e}_{laser}$ in Figure 3.2) is the internally supplied heat into the body per unit volume, P is the heat source power, (a, b) the ellipsoid semi-axes values and (ξ, η) the local coordinates at the ellipsoid center. F is a dimensionless power factor, constituting the only calibration parameter of the model. The power factor corrects for emissivity overestimation and transition from a three to two-dimensional heat source. The single-ellipsoid volumetric source was assigned dimensions $a = 40\ \mu m$, $c = 20\ \mu m$ and $b = 1\ mm$ accounting for the 2D analysis. At this point, based on the formulation of the boundary conditions, a distinction between Powder Bed (PB) and Powder Deposition (PD) methods must be exercised to achieve calculation of accurate temperature results. The model presented is based on the work of Spyrou and Aravas [58] on laser spot welding, and its additive manufacturing adaptation of Sotiriou et al. [53].

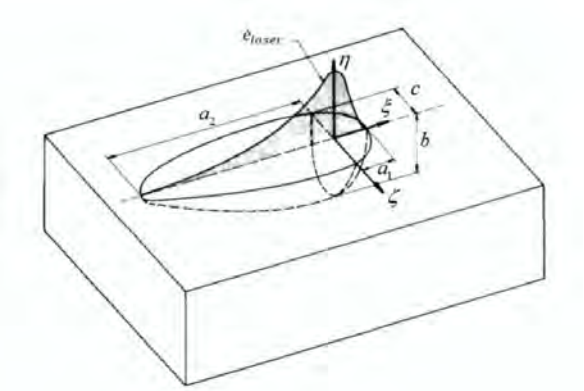

Figure 3.2. Double ellipsoid heat source input model with dimensions and local coordinate system, from Goldak et al. [27].

3.2.1. Heat transfer in Powder Bed (PB) methods

Aiming to provide a sophisticated formulation to better describe AM conditions, the effect of the deposited powder on top of the built material, as well as of the powder surrounding the built specimen (effective only for powder bed techniques), was considered. An illustration of the simulated powder bed geometry is presented in Figure 3.3.

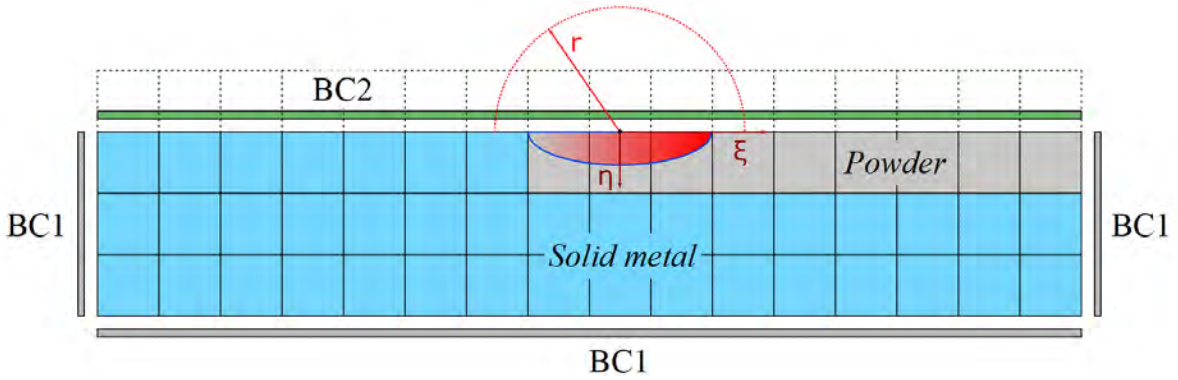

Figure 3.3. Powder bed methods simulation geometry and applied boundary conditions.

There are two different boundary conditions applied for the solution of the heat transfer analysis as they are applied on the free surface areas of the geometry in Figure 3.3, and are given in Table 3.1.

Table 3.1. Description of the boundary conditions

BC name	Description
BC1	Equivalent conduction BC in a semi-infinite medium with thermal conductivity k and known constant interface temperature.
BC2	Convection-radiation BC with applied forced convection anemometry and known constant interface temperature.

The BC1 boundary condition was developed for powder bed additive manufacturing techniques, to describe the dissipation of heat from the specimen free surfaces towards the surrounding powder bed environment. Heat transfer in powder beds is a complex phenomenon, that consists of combined conduction and radiation components, among the powder particles [59]. BC1 is based on constituting an equivalent cooling law expression in a semi-infinite

medium for the iteratively calculated surface temperature T_s and sink temperature $T_0 = 20℃$, given in Equation 3.10:

$$q_s = \frac{k_{eff}}{\sqrt{\pi a_{eff} t}}(T_s - T_0) \tag{3.10}$$

where k_{eff} is the equivalent thermal conductivity of the environment material, a_{eff} is the thermal diffusivity of the environment material, given in Equation 3.11 and t is the time from the activation of a boundary element upon which the boundary condition of Equation 3.10 begins to apply. For all powder-submerged free-surface areas of the geometry, BC1 is applied for $k_{eff} = k_p$. Formulation of the BC1 condition achieves computational relief and simulation speed, against the heavy additional FE simulation of the powder environment, and is justified based on the difference in order of magnitude between printed parts and the size of the powder bed bath. In powder bed techniques, as building progresses the manufactured part is gradually being submerged in powder, thus BC1 is applied on the base region as well, where the substrate geometry was omitted since building [12] often employs construction of supporting columns that account for less than 5% of the total base area. The effect time in Equation 3.10 models for the gradual heat accumulation in the powder bed. The thermal diffusivity of powder is calculated in Equation 3.11:

$$a_{eff} = \frac{k_p}{\rho_p c_{p,p}} \tag{3.11}$$

where $\rho_p = APF\rho_s$ and $c_{p,p} = APFc_{p,s}$. The APF_p describes the packing efficiency of the powder under the effect of gravity. For closely packed powder beds with consistent powder particles of constant diameter, is assumed that packing is similar to an FCC lattice, with $APF_p = 0.7405$. The thermophysical properties of the powder (red lines) in comparison with those of the solidified material (black lines) are presented in Figure 3.4. An enhancement in the quite element method [56] involved the consideration of powder as an intermediate state of "activated" material points, representing metal deposition regions. between the initial ($k = 0\ and\ c_p = 0$) and the terminal ($k = k_S\ and\ c_p = c_{p,s}$), where index s stands for the post-solidification material. This intermediate state would exhibit the effective thermophysical properties of the austenitic stainless steel powder, calculated as that were those of the solid materials multiplied with the atomic packing factor ($APF = 0.74$ for powder stacking roughly in close-structure FCC under the effect of gravity).

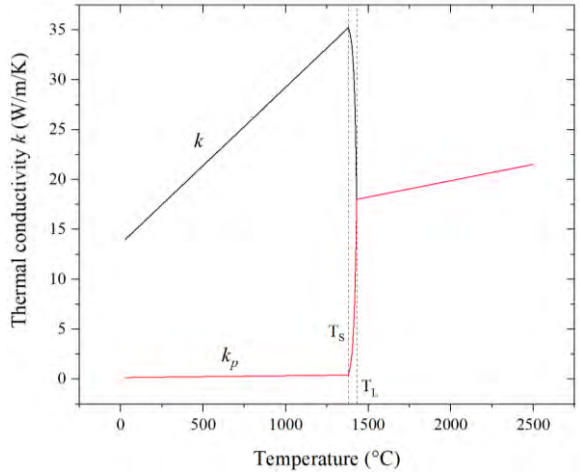

(a)

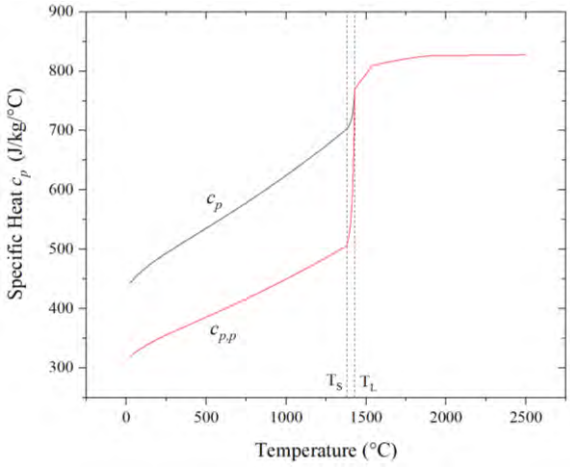

(b)

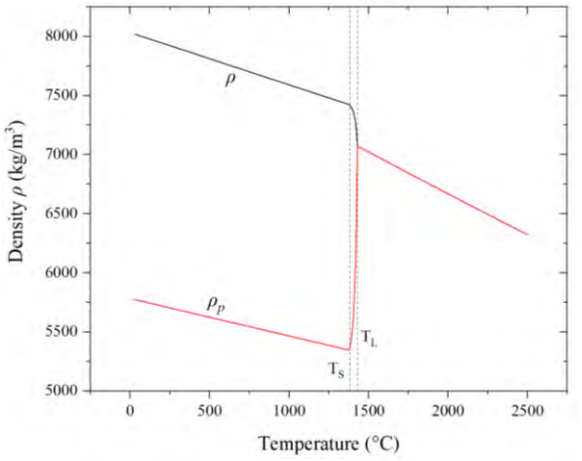

(c)

Figure 3.4. Thermophysical properties of consolidated (black lines) and powder (red lines) 316L: (a) Thermal conductivity k, (b) specific heat capacity c_p, (c) density ρ and (d) Latent heat temperature derivative.

All powder thermophysical properties describe the "complex" powder state in temperatures lower than solidus, since at that temperature, melting initiates and all properties change drastically. For temperatures higher than liquidus, metal powder is completely transformed to the melt state, according to thermodynamics as well as the nature of additive manufacturing. Since change of the element character from powder to consolidated metal occurs when the cooling stage begins, it is computationally convenient to maintain the powder thermophysical properties at temperatures over liquidus, and set them equal to the respective melt thermophysical properties. Note that in temperatures between the solidus and liquidus temperatures, a mixture rule with respect to the solid (considering the distinction between phases) and liquid phase fractions is applied to determine the thermophysical properties throughout the state change.

For the effective thermal conductivity of the powder as a continuous medium, an in-depth modeling approach was followed. Considering the resultant heat transfer flux that comprises of conduction-radiation components acting among the powder grains, an equivalent temperature-time-dependent conduction factor k_{eff} was formulated according to de Moraes and Czekanski [60], given in Equation 3.12 [59–61]

$$k_{eff} = k_g \left[J_1 + \sqrt{1-\varphi} \left(J_2 + \Lambda \frac{k_{contact}}{k_g} \right) \right]$$

$$J_1 = \left(1 - \sqrt{1-\varphi}\right) \cdot \left(1 + \frac{\varphi k_R}{k_g} \right)$$

$$J_2 = (1-\Lambda) \cdot \left(\frac{2}{1 - \frac{B k_g}{k_s}} J_3 + \frac{k_R}{k_g} \right) \tag{3.12}$$

$$J_3 = \left[\frac{B}{\left(1 - \frac{B k_g}{k_s}\right)^2} \left(1 - \frac{k_g}{k_s}\right) \ln\left(\frac{k_s}{B k_g}\right) - \frac{B+1}{2} - \frac{B-1}{1 - \frac{B k_g}{k_s}} \right]$$

where,

$$B = 1.25\left(\frac{1-\varphi}{\varphi}\right)^{\frac{10}{9}} \tag{3.13}$$

$$k_R = \frac{4\varepsilon_p \sigma T^3 x_R}{1 - 0.132\varepsilon_p} \tag{3.14}$$

$$k_{contact} = 18\Lambda k_s, \qquad for\ \Lambda < 3 \times 10^{-4} \tag{3.15}$$

In Equation 3.14, ε_p is the effective powder emissivity, calculated according to Sih and Barlow [61]:

$$\begin{gathered} \varepsilon_p = A_H \varepsilon_H + (1 - A_H)\varepsilon_s, where: \\ \varepsilon_H = \frac{\varepsilon_s\left[2 + 3.082\left(\frac{1-\varphi}{\varphi}\right)^2\right]}{\varepsilon_s\left[2 + 3.082\left(\frac{1-\varphi}{\varphi}\right)^2\right] - 1} \\ A_H = \frac{0.908\varphi^2}{1.908\varphi^2 - 2\varphi + 1} \end{gathered} \tag{3.16}$$

φ is the porosity of the bed, with $\varphi = 1 - APF_p = 0.2424$ for FCC [60], $\varepsilon_s = 0.55$ [62] is the solid emissivity, ε_H is the gap emissivity and A_H is the area fraction of the powder surface. r_p is the average powder diameter, which can be determined from the manufacturer's specifications (e.g., for 316L powder by [63], $r_p = 35\ \mu m$).

In Equation 3.12, k_g is the thermal conductivity of surrounding gas, which for a N_2 pure atmosphere (to decrease oxidation risk) Hoshino et al. [64] determined in Equation 3.17:

$$k_g = \sqrt{T}\left(\frac{a_1}{T} + a_2 + a_3 T\right) \tag{3.17}$$

$$a_1 = -1.125 \times 10^2$$

$$a_2 = 1.354 \times 10^0$$

$$a_3 = 1.453 \times 10^{-4}$$

In Equation 3.15, $\Lambda = 5 \times 10^{-6}$ from [59], is the fraction area of a powder particle in contact with neighboring particles (powder particles are not perfect spheres). Finally, the Marangoni effects were taken into account due to the effect of forced convection caused by the laser beam on the melt pool, enhancing thermal conductivity $k^*(T) = \lambda k(T)$ for $T > T_L$ according to [62,65], where $\lambda = 4$ is the isotropic enhancement coefficient.

Furthermore, the BC2 convection-radiation boundary condition of the free surface area in contact with the atmosphere, was modeled according to hot-film anemometry effect proposed by Gouge et al. [66] to account for the forced convection induced by the heat source beam.

$$h(r) = h_{max} e^{Br} + h_0 \tag{3.18}$$

where r is the radial distance from the heat source spot, illustrated in Figure 3.3, h_{max} is the peak value of the film coefficient, B an exponential decay rate and h_0 the convective offset.

3.2.2. Heat transfer in Powder Deposition (PD) methods

For powder deposition methods in additive manufacturing, the same formalism can be applied as described in Section 3.2.1, with two modifications. The BC1 boundary condition in powder environment is replaced by convection-radiation BC2 boundary condition with the atmosphere gas in all free surface areas of the mesh, as described in Equation 3.18. Secondly, the traditional quite element method of [67] applies, without powder present as an intermediate state and activation of a quite element will occur at the moment of heating initiation, assigning the powder properties briefly and only for the duration of the first heating, as illustrated in Figure 3.5. An interesting observation is that in the powder deposition model, the forced convection anemometry is effective for vertical free surface areas (illustrated by the red circular section in Figure 3.5), in contrast with the powder bed model, where the presence of the powder does not permit for classic convection-radiation BC inside the powder bed. Moreover, BC1 depending on the manufacturing process can account for a metal substrate (wrought or cast alloy) from where the main heat dissipation flow is abducted. In that case, Eq. 3.10 and 3.11 are formulated:

$$q_s = \frac{k_{sub}}{\sqrt{\pi a_{sub} t}}(T_s - T_0) \tag{3.19}$$

$$a_{sub} = \frac{k_{sub}}{\rho_{sub} c_{p,sub}} \tag{3.20}$$

Where k_{sub}, ρ_{sub} and $c_{p,sub}$ are the thermal conductivity, density and specific heat of the substrate material respectively.

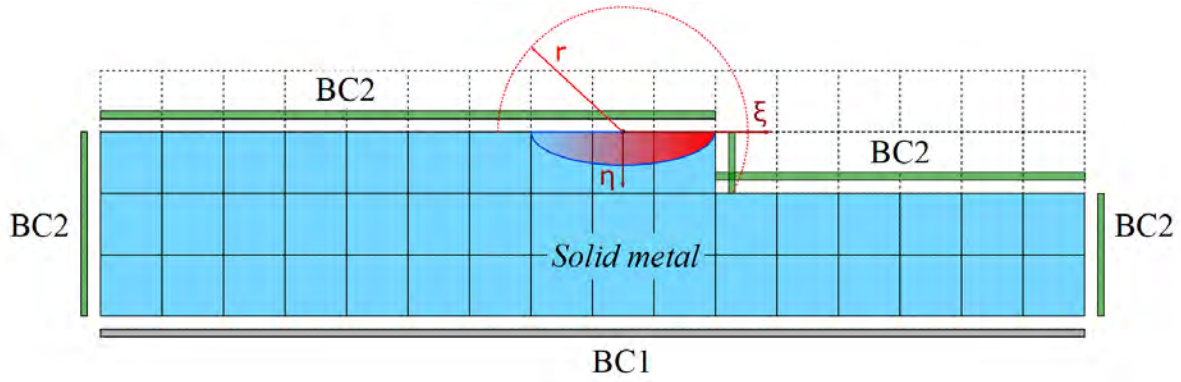

Figure 3.5. Powder deposition methods simulation geometry and applied boundary conditions.

Chapter 4. CALPHAD-based simulation of microstructural evolution

4.1. Introduction to CALPHAD modeling of microstructural evolution

In Chapter 2, the solidification mechanisms and their dependence on composition, cooling rate and morphology were established. The objective of the present study is to model the non-equilibrium phase transformations and provide a simulation framework to predict the microstructural evolution in additive manufacturing of austenitic stainless steels. Computational thermodynamics and kinetics based on the CALPHAD approach [68–73], were employed to simulate the microstructural evolution upon solidification and sub-sequent solid-state transformations, occurring under rapid cooling and thermal cycling conditions. The CALPHAD approach, is based on minimizing the Gibbs free energy of phases in multi-phase and multi-component systems, and carry out phase equilibria to calculate the phase diagram of the system. The Gibbs free energy is calculated based on the Redlich-Kister-Muggianu (RKM) model for substitutional solid-solutions [74]:

$$G = \sum_i X_i G_i^o + RT \sum_i X_i ln X_i + \sum_i \sum_{i \neq j} X_i X_j \sum_p L_{ij}^{(p)} \left(X_i - X_j\right)^p + \sum_i \sum_{i \neq j \neq k} X_i X_j X_k \sum_p L_{ijk}^{(p)} \tag{4.1}$$

and for interstitial solid-solutions (application on C), ignoring the magnetic terms:

$$G = G^o + G^{id} + G^{xs} + G^{mag}, where:$$

$$G^o = \sum_i y_i y_C G_{i:C}^o + \sum_i y_i y_{Va} G_{i:Va}^o$$

$$G^{id} = RT \sum_i y_i ln y_i + cRT(y_C ln y_C + y_{Va} ln y_{Va})$$

$$G^{xs} = y_C \sum_i \sum_{i \neq j} y_i y_j L_{i,j:C} + y_{Va} \sum_i \sum_{i \neq j} y_i y_j L_{i,j:Va} + y_C y_{Va} \sum_i y_i L_{i:C,Va} + y_C \sum_i \sum_{i \neq j \neq k} y_i y_j y_k L_{i,j,k:C} + y_{Va} \sum_i \sum_{i \neq j \neq k} y_i y_j y_k L_{i,j,k:Va} \tag{4.2}$$

$$G^{mag} = RTln(\beta + 1) f(T/T_c)$$

In multi-component and multi-phase systems, calculation of the Gibbs free energy employs information from thermodynamic databases. The methodology is implemented commercially in Thermo-Calc software [22]. Simulation of diffusive phase transformations during additive manufacturing, requires solution of a moving interface problem with kinetic calculations, solving the equation formulated by Borgenstam et al. [73] in multi-component systems:

$$J_k = -\sum_{i=1}^{n} L'_{kl} \sum_{j=1}^{n} \frac{\partial \mu_i}{\partial c_j} \frac{\partial c_j}{\partial z} \tag{4.3}$$

A local equilibrium condition is applied on the moving interface, with solute limits determined from CALPHAD-based thermodynamics. Mobility information is required to solve the

equation systems, provided by kinetic databases, implemented in the DICTRA module of Thermo-Calc [22].

In Section 4.2 simulation of solidification compares the applicability of CALPHAD thermodynamic and kinetic models under rapid-solidification conditions, while Section 4.3 presents the modeling for different solidification morphologies. In Section 4.4 simulation of solid-state transformations under rapid cooling and thermal cycling is carried out and in Section 4.5 a methodology for calculating non-equilibrium thermophysical properties is displayed.

4.2. Solidification

The analysis objective of the present section is to simulate the microstructural evolution during the solidification process, using computational thermodynamics and kinetics based on the CALPHAD approach [68,69]. The plethora of phenomena involved during solidification, as discussed in Chapter 1, add to the modeling complexity. Several simulation models were employed, each based on a different set of assumptions, approaching the transformation from a slightly different angle [75]. The validity of the model assumptions was examined and simulation results were compared to determine which model better describes solidification under rapid cooling conditions. An AISI 316L austenitic stainless steel with nominal composition given in Table 4.1, was considered in all simulations as reference to compare the solidification models. Initially the limiting case of equilibrium solidification is investigated in Section 4.2.1, which, despite being not applicable under additive manufacturing conditions, provides useful information regarding the system's thermodynamic behavior. Next, introduction of the cooling rate effect was investigated during solidification under non-equilibrium conditions, initially assuming an infinitely high value with the Scheil-Gulliver approach in Section 4.2.2 and then simulating a finite value with the DICTRA model in Section 4.2.3, better approximating the conditions during additive manufacturing.

Table 4.1. Reference AISI 316L composition in (wt%)

316L	Cr	Ni	Mo	C	Mn	Fe
Composition (wt%)	18	14	2.6	0.03	1	bal.

4.2.1. Equilibrium solidification

Computational alloy thermodynamics, based on the CALPHAD approach [68,69], were employed to describe the microstructural constitution at equilibrium conditions as well as the driving forces for phase transformations. All thermodynamic calculations were performed in the Thermo-Calc software [22] coupled with the TCFE11 thermodynamic database for ferrous alloys. Based on the reference composition of Table 4.1, two isopleth sections of the phase diagram were computed, with respect to Cr and Ni presented in Figures 4.1(a) and (b) respectively. In both Cr and Ni-Isopleth sections, solidification tie triangle is revealed, defined by apexes A (the eutectic point), B and C (limits of solute solid solubility in δ-ferrite and austenite respectively), where the liquid phase (L), primary austenite (γ) phase, and primary ferrite (δ) phase coexist at equilibrium. The solidification's type can be characterized based on the relative position of the system at which the solidification path proceeds (noted by the red-dotted line), compared to the corners of the triangle, according to the analysis of Section 2.1.1.

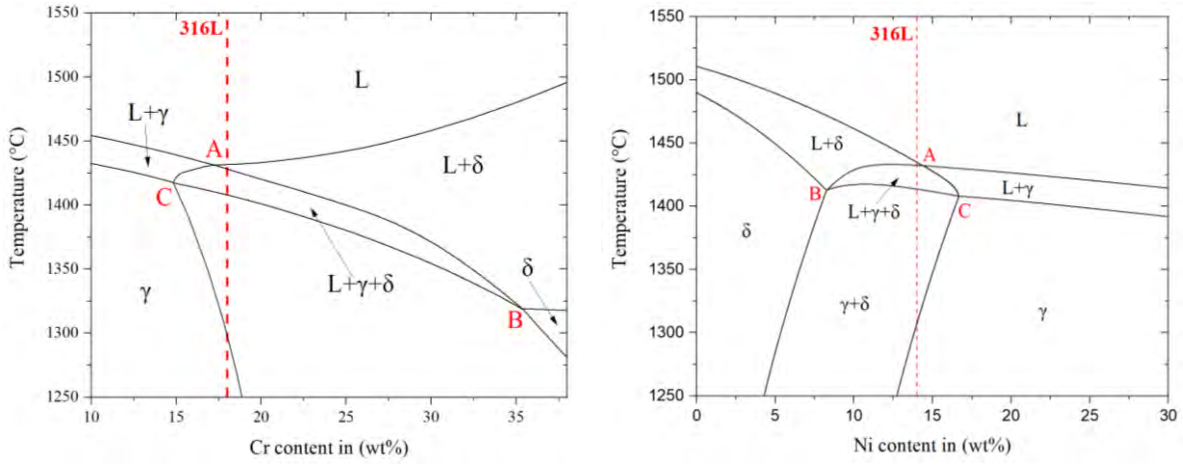

(a) (b)

Figure 4.1. Equilibrium solidification path of reference 316L system. (a) Cr-Isopleth and (b) Ni-Isopleth.

In equilibrium solidification calculations, the solidification mode is a result and not prerequisite to apply the modeling. The reference 316L system exhibits an FA-type solidification behavior, with primary solidification of δ-ferrite precedes the eutectic reaction. Figure 4.1 implements the effect of the additional alloying elements on thermodynamic behavior, in contrast to the ternary system of Figure 2.1. The equilibrium solidification path of the systems is presented in Figure 4.2. A distinction between single-phase and two-phase growth can be established by an increase in the solidification rate that characterizes independent eutectic growth.

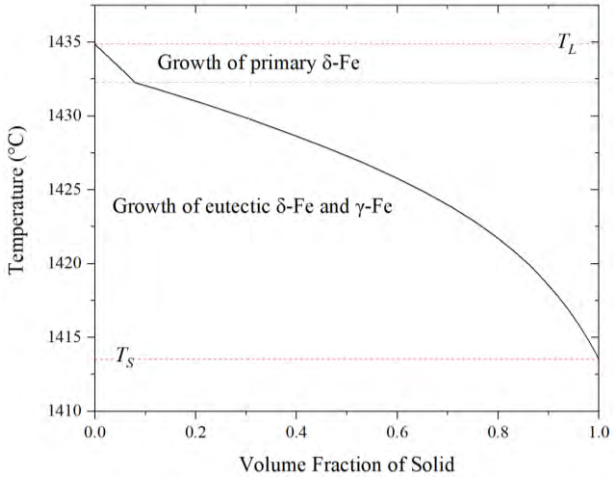

Figure 4.2. Equilibrium solidification path of reference 316L system.

Equilibrium solidification is a limit case, corresponding to infinitesimal cooling rate combined by sufficient time for diffusion to take place for the system to reach equilibrium conditions (compositions and phase fractions) at each temperature increment. It exhibits a freezing range value of $FR^{eq} = 21.32℃$ for the reference system. The limiting case of equilibrium solidification provides useful information regarding the behavior of the system upon solidification and is the basis for the following non-equilibrium calculations. As was discussed in Chapter 2, from the Cr and Ni-Isopleth, the upper/lower compositions of the tie-triangle apex points B, C are determined, and the Cr_{eq}/Ni_{eq} transition ratios among solidification modes can be determined and set as boundaries in the low cooling rate region of multi-component solidification mode maps, derived from Figure 2.7(a) [29]. Additional thermodynamic

calculations and sensitivity analysis, indicated that all systems exhibited constitutional sensitivity to C and N content, greatly influencing thermodynamics and equilibrium solidification mode, both primary and total. Exemplary of this behavior is the solidification mode transition between 316L solidifying with FA-type and 316LN that changes the mode to AF for less than 1 wt% N content. This behavior is important when printing takes place in nitrogen environment, where excess N can be absorbed in the solidifying melt pool. Another effect concerns variations due to microsegregation, despite both C and N being fast diffusing elements.

4.2.2. Scheil-Gulliver model

During additive manufacturing processes, the heat source develops high temperatures at the point of impact, forcing the material (e.g. powder) to melt. As the source moves away, the material solidifies under high cooling rates and therefore non-equilibrium conditions. To better describe the non-equilibrium solidification phenomena, resulting from rapid cooling, the Scheil–Gulliver model was employed, as implemented in Thermo-Calc. Scheil–Gulliver simulations consider the extreme case of infinite cooling rates, assuming that no diffusion occurs in the solid phases, infinite diffusion in the liquid and that local equilibrium conditions are established on the solid/liquid interface, at all times during solidification. The developing microsegregation in solid, is described by the Scheil equation:

$$c_s^* = kc_o(1 - f_s)^{k-1} \tag{4.4}$$

where c_s^* is the concentration of the solid/liquid interface at f_s fraction solid, c_o is the nominal composition of the melt and k is the partition coefficient $k = c_s^*/c_L^*$. An important aspect of this model is that all systems will solidify according to the three-phase reaction, no matter the solidification mode. Therefore, the Scheil-Gulliver approach constitutes a limit case for a reference system of phases, for all kinetic modeling variations. In order to ensure computational stability, the simulation terminated at 99% of the solidification process. Simulation results of the Scheil-Gulliver model for the reference 316L systems are presented in Figure 4.3, considering two-phase solidification:

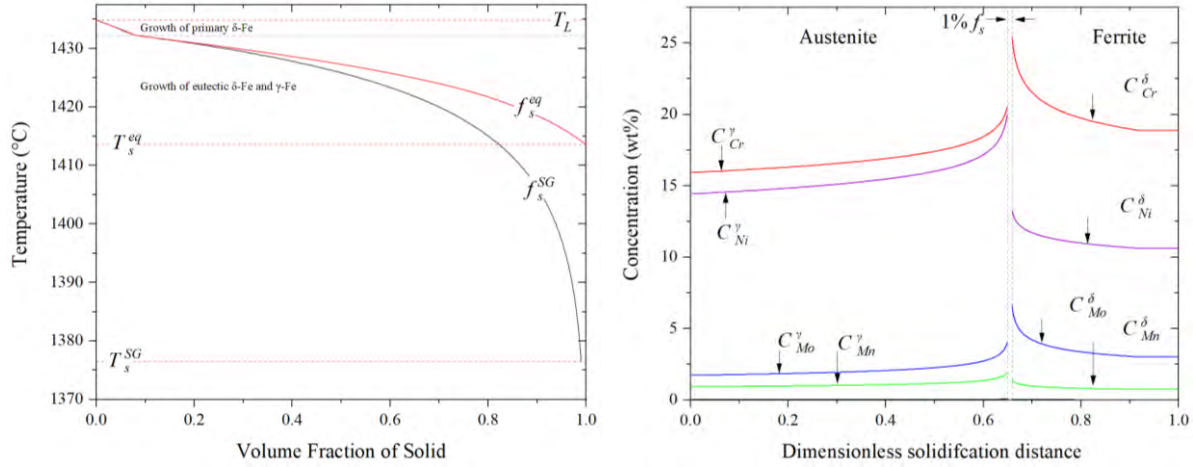

(a) (b)

Figure 4.3. Scheil-Gulliver simulation results. (a) Scheil and equilibrium solidification paths comparison and (b) Scheil segregation profiles.

The non-equilibrium solidification path, produced from the Scheil model is pictured in Figure 4.3(a), alongside its equilibrium solidification counterpart. While the liquidus temperature

remains unchanged, the Scheil-Gulliver solidus T_S^{SG} resides at 1376.5°C, creating a freezing range $FR^{SG} = 58.36$°C. Since the Scheil hypothesis treats the solid phases as independently growing from liquid, the model is eutectic in character. This is apparent from the segregation profiles of both austenite and ferrite, given in Figure 4.3(b). Figure 4.3(b) was constructed from the results of the Scheil model, in reference to the simulated dimensionless microstructural distance, in a way that is comparable to the DICTRA diffusion cell and accounts for the model assumptions. Austenite and δ-ferrite were placed in opposite ends of the dimensionless cell, to explain the independent growth character of the Scheil model. The solid phases do not have any interaction except with the liquid phase. Development of microsegregation is positive in both cases towards the melt, in contrast with experimental observations [46,76].

The Scheil-Gulliver model has been a contender in describing the microstructural evolution under high cooling rates. The model is however accurate for rapid solidification in very high interfacial velocities (Section 2.3.1). For cooling rates in most welding and additive manufacturing applications, the solidification mechanism remains diffusive and the Scheil model overpredicts the non-equilibrium effects [77]. Therefore, an in-depth non-equilibrium analysis that simulates diffusion in multi-component and multi-phase systems, is promoted as the most suitable modeling to predict the microstructural evolution.

4.2.3. Solidification using diffusion control transformation kinetics

The equilibrium solidification and the Scheil–Gulliver models provide a fast and reliable method of determining the key phenomena and microstructural features during solidification. However, they both lack in the fidelity required to capture the interactions from subsequent heating and cooling cycles, as well as the spatial and temporal evolution of microstructural features, upon additive manufacturing processing. The present section is concerned only with the simulation of solidification, with solid-state transformation results presented in Section 4.4. Kinetic calculations were performed in the DICTRA module of Thermo-Calc [22], coupled with the MOBFE2 mobility and TCFE6 thermodynamic databases. One-dimensional mass diffusion was considered in a planar geometry diffusion cell, with a size of 0.5 μm, representative of the as-solidified microstructure. The cell is assumed a closed thermodynamic system with no mass with the environment, under the effect of a temperature global condition. All regions are separated by moving interfaces where local equilibrium conditions are imposed during transformations and every interface is defined by a position of interface (POI) and a velocity of interface (VOI). POI values determine the phase fractions and VOI values the transformations velocity.

In all cases, simulation initiates at a temperature higher than liquidus, when the system resides in the liquid state. The cell is thus initially comprised of a single liquid phase region. In order to simulate growth of a solid phase, it must be placed adjacent to the liquid region as inactive. As the temperature decreases and the inactive phases become thermodynamically stable, they nucleate and grow, consuming the liquid. However, DICTRA is a 1D sharp-interface model that does not simulate the nucleation of a phase directly, but rather than describes the growth of a phase after the driving force for nucleation exceeds a critical value. This model assumption is suitable for application in additive manufacturing, where no nucleation kinetics take place at the melt pool periphery, and solid cells grow epitaxially from the substrate. Moreover, DICTRA provides the ability to model the three-phase reaction and/or primary solidification growth of either austenite or δ-ferrite, by modeling diffusion in a specific geometric configuration that approximates a specific morphology via selecting the structure/sequence of

phases on the cell, thus taking into account the solidification mode. Further morphology modelling can be also applied by determining the cell size to attest for the principal diffusion distances, as well as considering two or more cells connected by immobile interfaces that permit solute flow, as will be discussed in Section 4.3. In this section, the analysis focuses on simulation of cellular growth, as the dominant microstructural feature in additive manufacturing, assuming that microsegregation develops only on the transverse section of cells and not the longitudinal. This is in contrast to findings by Poole and Weinberg [78], reporting rejected solute ahead of the dendrite tip, however minor in nature compared to the transverse partitioning, thus justifying the assumption.

To study the effect of diffusion cell structure, a series of five systems, derived from the reference 316L composition by changing the Ni content to adjust the solidification mode, were examined. The Cr and Ni composition of the systems are given in Table 4.2. Each system corresponds to a cell structure. This model comparison aims to investigate the microsegregation behavior of solidification types, in order to provide an insight to experimental identification of solidification modes. The Ni-Isopleth of the 316L reference system is presented in Figure 4.4, containing the solidification paths of the additional systems.

Table 4.2. Solidification mode systems as derived from the reference 316L system composition.

Solidification mode system	Cr (in wt%)	Ni (in wt%)
FL	18	8
LAF	18	10
ALF (316L)	18	14
LFA	18	16
AL	18	17

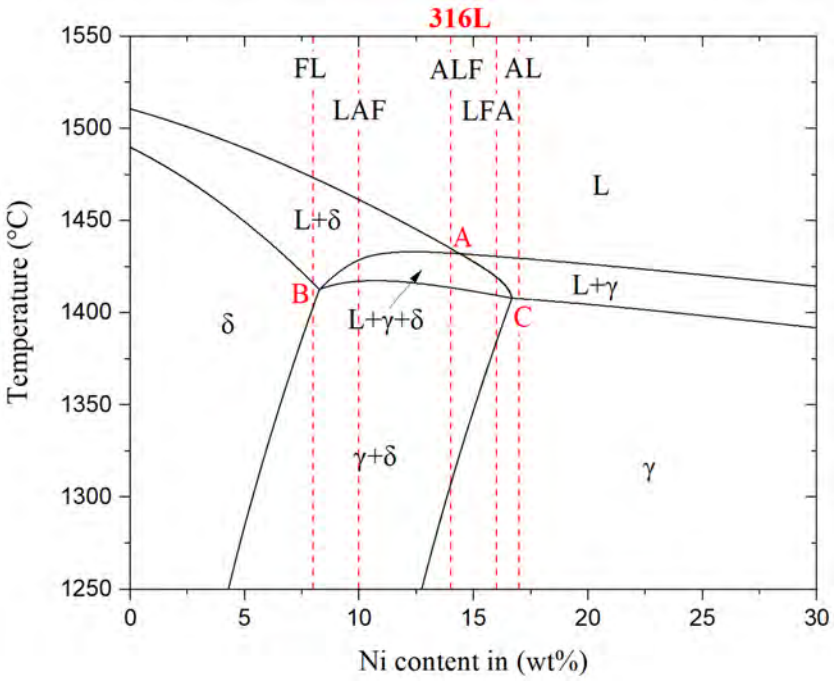

Figure 4.4. Diffusion models systems and corresponding solidification mode.

For single-phase solidification, modeling for either A or F-type, one inactive region of either γ austenite or δ ferrite is attached adjacent to the initial liquid region. The diffusion cells for A and F-type solidification are pictured in Figure 4.5.

(a) (b)

Figure 4.5. Single-phase solidification cells: (a) Single austenite AL for type-A and (b) single δ-ferrite FL for type-F.

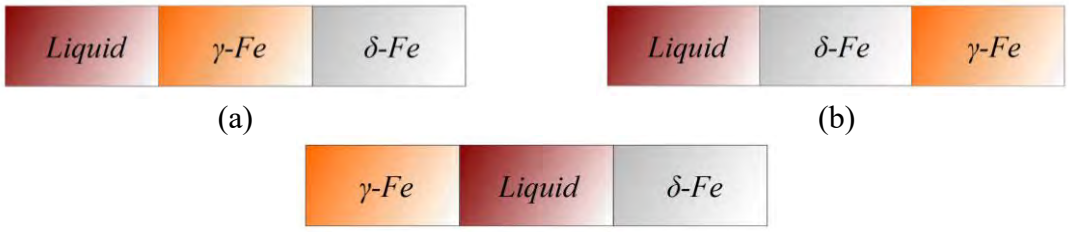

(a) (b)

(c)

Figure 4.6. Two-phase solidification models: (a) Left (Ni-poor) peritectic LAF, (b) right (Ni-rich) peritectic LFA and (c) eutectic ALF model simulating AF or FA solidification.

For two-phase solidification systems, the cell is initially comprised of a single liquid phase region with two inactive regions of γ austenite and δ ferrite adjacent to it, separated via moving interfaces [53,75]. As the temperature decreases and the inactive phases become thermodynamically stable, they nucleate and grow, consuming the liquid. The positioning of the austenite and ferrite regions compared to the liquid region allows for modeling of either eutectic or peritectic reactions. Eutectic solidification is simulated by positioning the austenite and ferrite regions of each side of the liquid as γ/L/δ, from now on referred to as ALF model. By positioning the austenite and ferrite phases adjacent to each other and the liquid, either as L/γ/δ, the LAF model, or as L/δ/γ, the LFA model is obtained, simulating the Ni-poor or the Ni-rich peritectic reaction respectively. Diffusion cells for all two-phase solidification models are illustrated in Figure 4.6. Note that the reference 316L system is included in the set of systems, corresponding for the ALF diffusion model. In addition, the AL system, although residing in FA equilibrium solidification type, is investigated for A-type solidification, since in high cooling rates, a transition from AF to A mode is observed [29]. Diffusion control simulation of solidification was carried out under a linear temperature profile with a cooling rate value $R = 1000℃/s$. Results in terms of solidification paths and microsegregation profiles of Cr and Ni at the end of solidification, for all models are given in Figure 4.7. While quantitative comparison of solidification paths or segregation profiles is inappropriate given that the systems have different nominal compositions, it is important to qualitatively compare the segregation behavior. The solidification path diagrams are included for completion to indicate the ability of the models to predict transient phase evolution. Also, by definition a positive segregation refers to an increasing amount solute content while a negative segregation to a decreasing amount of solute content.

Single phase solidification models AL and FL, exhibit continuous composition profiles. In AL model (Figure 4.7(b)) the growing austenite absorbs Ni and rejects Cr in the melt, with Cr developing a positive and Ni a negative segregation towards the cell walls (where the last liquid solidified). The opposite behavior is present in F-type solidification (Figure 4.7(j)), however,

due to the BCC structure enabling diffusion, segregation of both element is restricted in an insignificant spatial variation. The final microstructure is considered homogeneous. An important observation is the change of monotonic decrease in the segregation of Cr close to the cell walls, enabling backwards diffusion. This phenomenon relates to thermodynamics and more specifically to the shape of the monophasic solvus line, signifying a transition from increasing to decreasing solubility as the temperature drops, with solidification segregation capturing the effect.

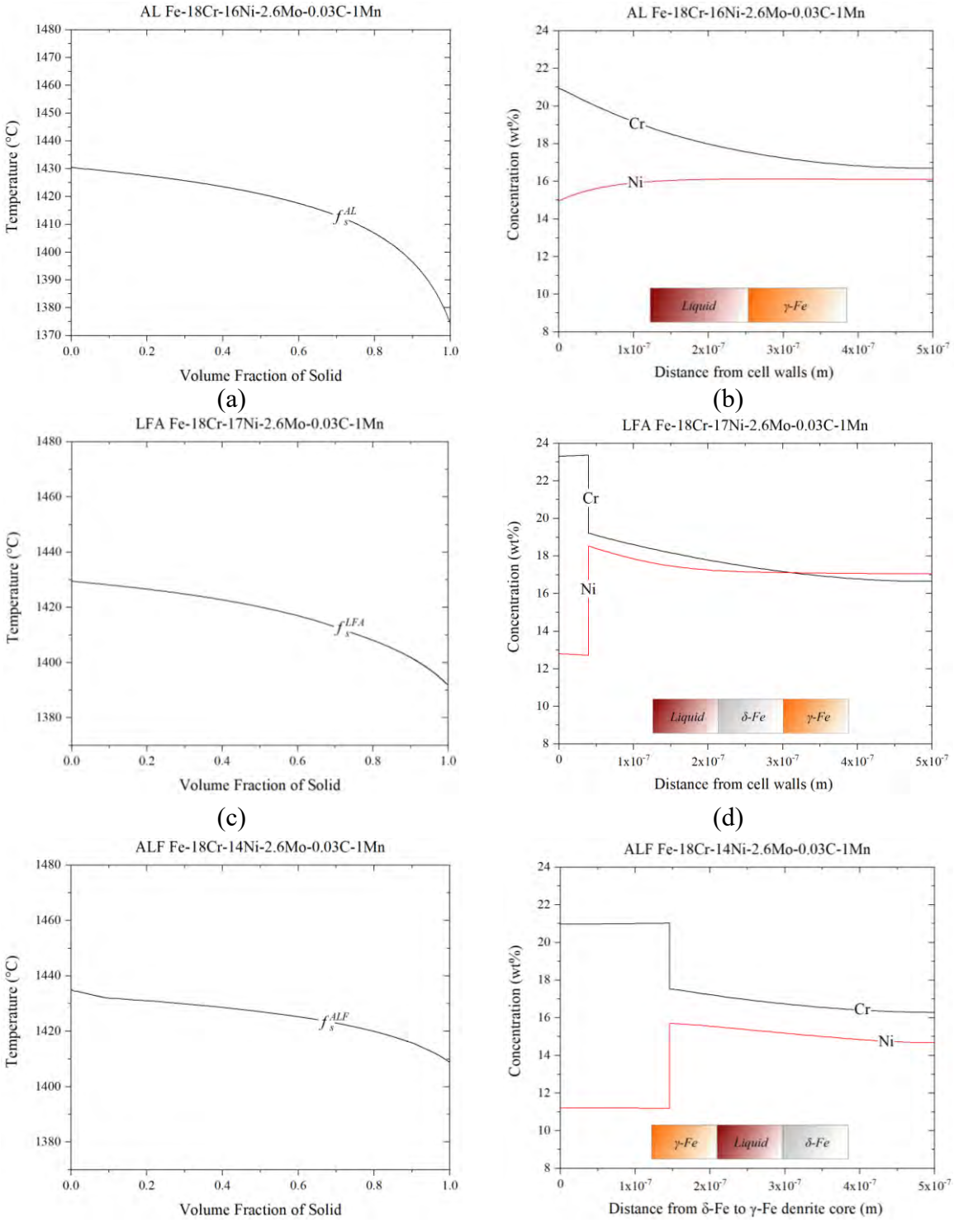

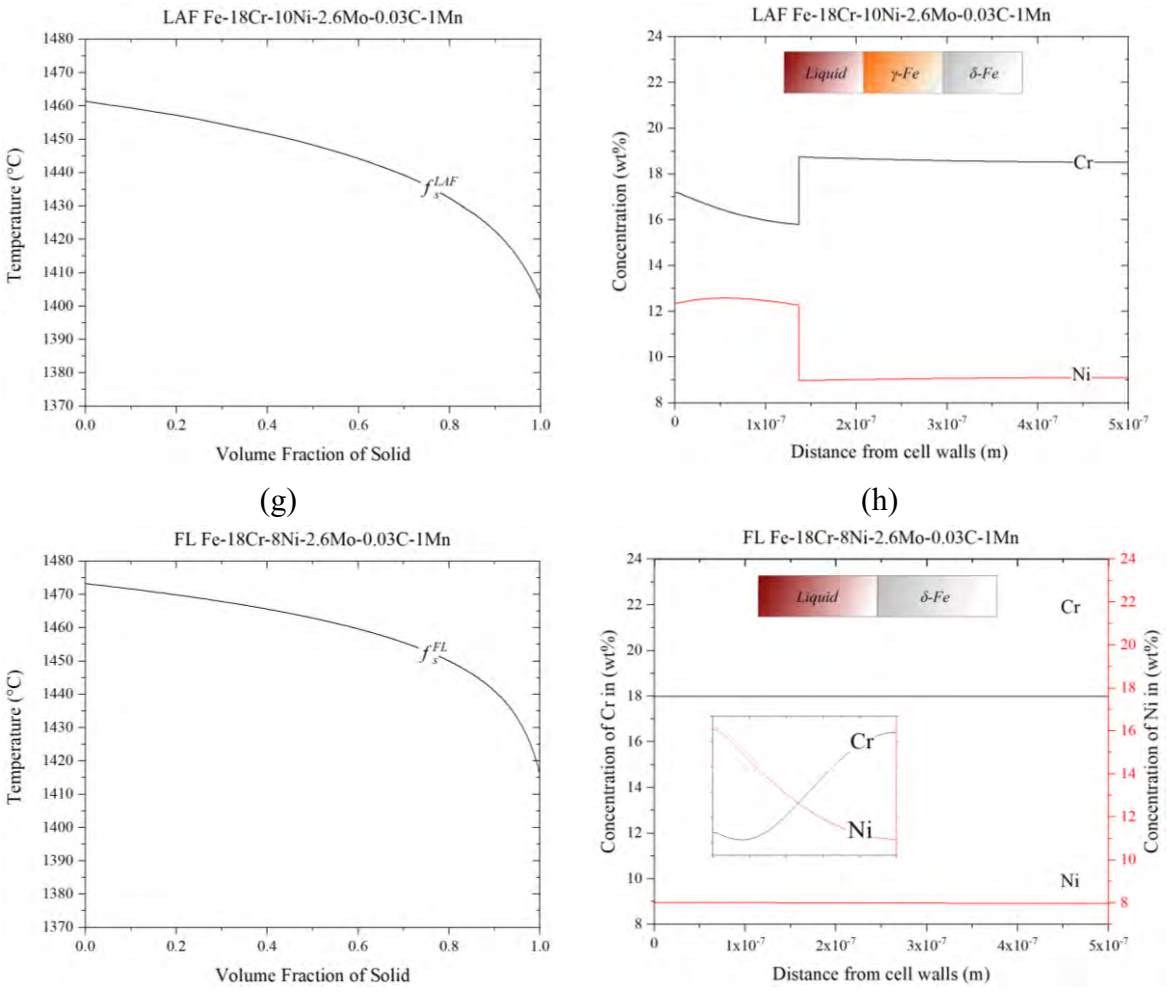

Figure 4.7. Solidification paths and microsegregation of Cr and Ni of reference systems in diffusion models: (a)-(b) AL model, (c)-(d) AFL model, (e)-(f) ALF model, (g)-(h) LAF model and (i)-(j) FL model.

Similar phenomena are present in two-phase peritectic solidification types, as shown in Figures 4.7(d) and (h). In Figure 4.7(d), the Ni-rich system in the peritectic LFA model exhibits positive segregation towards the moving interface in austenite and the highest Cr segregation towards the cell walls in all models. In Figure 4.7(h), the Ni-poor system in the peritectic LAF model, austenite is nucleated on the δ-ferrite dendrites/cells and begins to consume the melt that is rich in ferrite stabilizing elements due to segregation. From Figure 4.7(h) a relatively homogeneous ferritic dendrite core is observed at the right of the moving interface. Peritectic austenite exhibits significant segregation, positive for Cr towards the last liquid and negative for Ni both towards the last melt and the δ-ferrite, corresponding to the same thermodynamic effect as discussed for Cr segregation in the FL model. The application limits for the peritectic reactions result from the calculation of nucleation kinetics of either austenite or δ-ferrite, that is not included in the presents study, however a thermodynamic boundary for the three-phase reaction transition from eutectic to peritectic has been discussed in Section 2.1.1.

Finally, in ALF model as pictured in Figure 4.7(f), segregation is developed towards the separating moving interface, where the last liquid solidified, and is positive in all cases except for Ni in δ-ferrite. In δ-ferrite, the relatively more relaxed structure of the BCC lattice allows for diffusion to flatten the segregation profiles according to thermodynamics, in contrast to all

other diffusion models, where Ni segregated towards austenite and Cr towards ferrite. ALF models for independent growth of both austenite and δ-ferrite and simulates microstructural evolution under the same philosophy as the Scheil-Gulliver approach. Comparison among equilibrium solidification, the Scheil-Gulliver model and DICTRA ALF under increasing cooling rate is depicted in Figure 4.8 calculated for a Fe-18Cr-12Ni-2.6Mo-0.03C-1Mn system [53]. As stated previously, equilibrium and Scheil-Gulliver act as limit cases for diffusion in independent growth. ALF model's behavior resides in-between.

In Figure 4.8, the solidification paths with respect to temperature and fraction of solid are shown using the equilibrium and Scheil–Gulliver models and the ALF diffusion model at two different constant cooling rates (1000 and 10000 °C/s), The Scheil–Gulliver model resulted in the highest freezing range of 70.57°C, whereas the equilibrium at the lowest, standing at 31.97°C. Accordingly, for the case of the ALF diffusion model, employed to simulate the eutectic reaction, increasing the cooling rate results in higher freezing range. For high cooling rates, the solidification path curve approaches the curves calculated by the Scheil–Gulliver model, while for low cooling rates, the solidification path and the freezing range approach the equilibrium solidification.

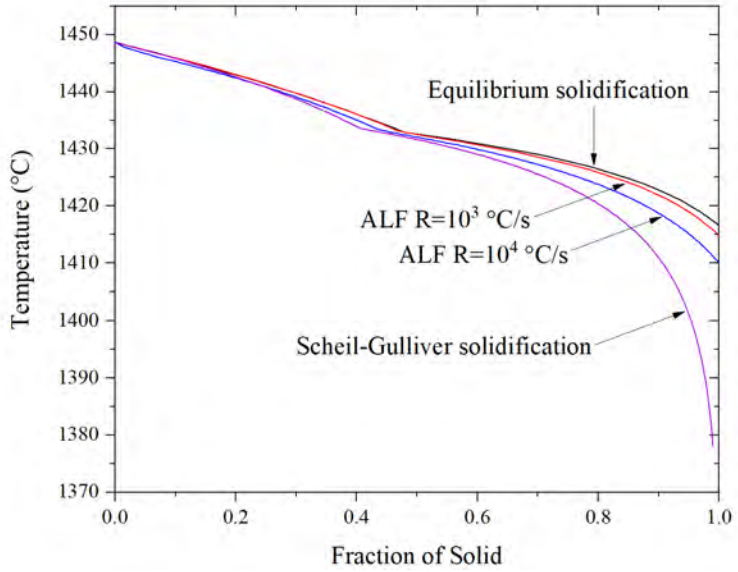

Figure 4.8. Model comparison on freezing range and the effect of cooling rate.

Similar results are extracted from analysis on single-phase solidification models, with the difference that Scheil must also consider only the corresponding single phase in its calculations. Therefore, the cooling rate determines the width of the freezing range, and the results calculated by the ALF diffusion model are located between the results obtained by the equilibrium and the Scheil–Gulliver models, deviating from equilibrium towards Scheil as the cooling rate increases. From Figure 4.8 it is evident that under intermediate-high cooling rates developing in additive manufacturing processes, solidification remains diffusion controlled, and the Scheil approach overestimates the freezing range and microsegregation.

4.3. Solidification morphology modeling

In Section 4.2.3 it is argued that diffusion transformation kinetics modeling can be applied to simulate effectively the microstructural evolution in form of columnar growth in high-rate solidification processes. However, in Section 2.3.1 the KGT dendrite growth theory predicts the evolution of additional dendritic morphologies moving towards the center of the melt pool,

namely the columnar-dendritic and the equiaxed-dendritic. The majority of experimental evidence for additive manufacturing of austenitic stainless steels [46,79–85] suggest that cellular growth is the dominant microstructural evolution mechanism. This can be because additional material deposition remelts regions close to the melt pool center where mostly equiaxed dendritic and columnar dendritic morphologies reside, or simply the spatial temperature gradient does not allow for extended evolution of dendritic morphologies. Nevertheless, in this section, additional models are proposed, to simulate the columnar- and equiaxed-dendritic morphologies for single phase or eutectic/independent solidification, within the context of diffusion control transformation modeling. Illustrations for all solidification morphology models for independent growth are presented in Figure 4.9 for single- or two-phase solidification. Note that s_i stands for the solid phase in single-phase solidification and can be either δ-ferrite or austenite. All the proposed dendritic models retain a conjectural character since they need accurate validation for a variety of cases, and are included in this chapter for completion purposes only.

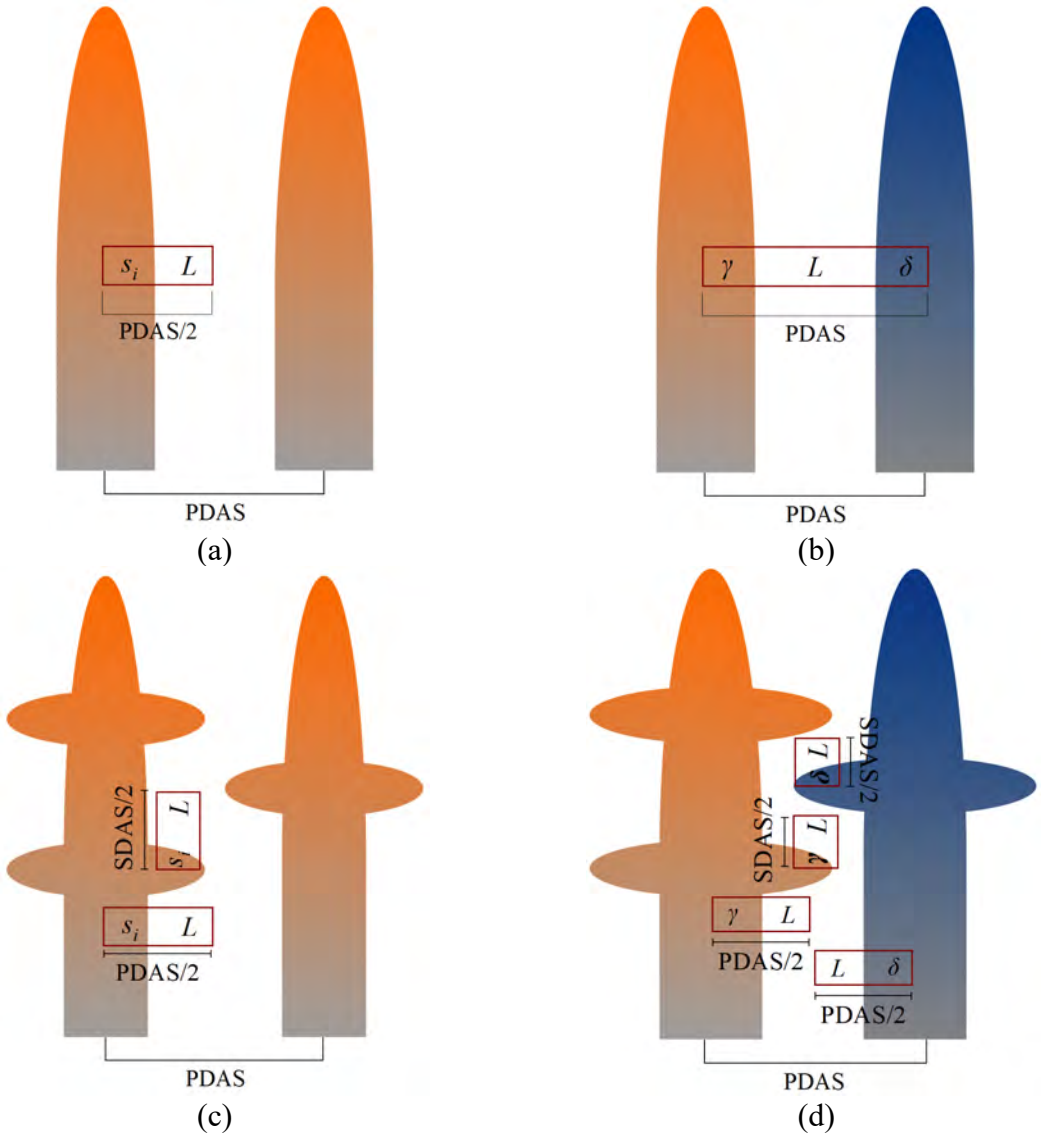

(e) (f)

Figure 4.9. Solidification morphology models: (a) Single-phase cellular, (b) two-phase cellular, (c) single-phase dendritic, (d) two-phase dendritic, (e) single-phase equiaxed and (f) two-phase equiaxed.

In Figures 4.9(a),(b) the models for single and two-phase cellular growth are presented, and they correspond to models AL, FL for single-phase and ALF for two-phase solidification, as presented in Section 4.2.3.

In order to simulate the columnar-dendritic morphology of Figures 4.9(c),(d), a dual cell planar geometry DICTRA scheme is required: the first cell simulating diffusion across the PDAS and the second cell across SDAS. The model assumes that similar temperature gradients apply from the melt towards the primary and secondary dendrite arms, formulated by the same global temperature condition. Due to symmetry between neighboring columns and among secondary arms, the respective diffusion cell sizes are reduced to PDAS/2 and SDAS/2. For single-phase solidification, the model is presented in Figure 4.10(a). Before Secondary Dendrite Arms (SDA) begin to form, microstructural evolution is determined by a diffusion cell similar to the cellular models AL and FL. The solid Primary Dendrite Arm (PDA) is separated from the liquid via a moving interface with position defined by $x_{sL}^{PD}(t)$. When $x_{sL}^{PD}(t) = x_{sL}^{PD}(t_{SDAS})$ where t_{SDAS} is a critical time value at which there is an interface instability [86], secondary dendrite arms begin to form and become regulatory of the microstructural evolution. At this point, the first simulation terminates and a second diffusion cell with the properties, size and solute distribution profiles of the solid PDA is created. While PDA boundaries do not change significantly [87], they maintain solute redistribution with the liquid due to contact via extended surface area, acting as a source or sink of alloying elements. Microstructural evolution of secondary dendrite arms is simulated considering a third 1D diffusion cell with a size of SDAS/2, under the same global temperature condition as the first diffusion cell. To simulate solute redistribution between the primary dendrite arm and the liquid, the second Solid PDA diffusion cell is considered connected to the Liquid region of the third SDA diffusion cell, separated via an immobile interface ($V_{sL} = 0$), so that the solid PDA phase can exchange mass with the melt without changing its fraction, as illustrated in Figure 4.10(a).

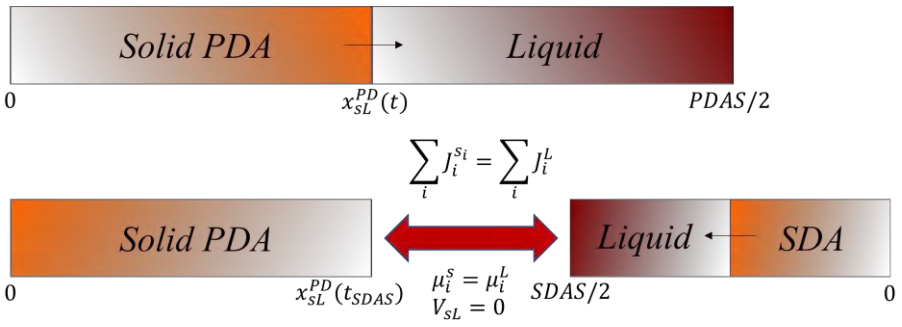

(a)

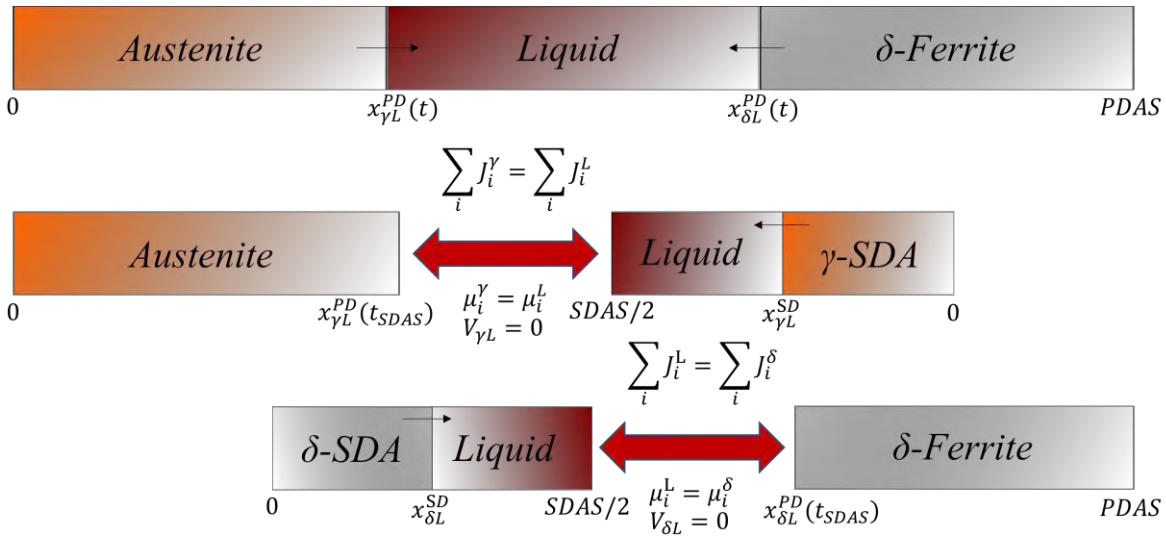

(b)

Figure 4.10. Columnar-dendritic morphology models: (a) Single-phase and (b) two-phase solidification.

Simulation of two-phase columnar-dendritic solidification of Figure 4.9(d) follows a similar modeling approach. Initially, PDAs transverse growth of austenite and δ-ferrite is simulated employing the eutectic/independent ALF model. Once the interfaces become unstable (which can be on different time instances), the solid PDA regions are transferred into separate diffusion cells (maintaining their properties and solute profiles) and a second set of diffusion cells is considered, one for simulation of the austenitic and one for simulation of the δ-ferritic secondary dendrite arms, with immobile interfaces connecting each liquid region to the respective solid PDA cell in order to enable mass transfer. The two-phase columnar-dendritic simulation scheme is illustrated in Figure 4.10(b).

Finally, simulation of the equiaxed-dendritic morphology of Figures 4.9(e),(f), for either single- or two-phase solidification, employs similar models to the cellular morphology. Single-phase solidification considers a 1D diffusion cell, with a size equal to half the equiaxed grains spacing (EGS) due to symmetry, and a cell structure similar to either AL or FL models, while two-phase solidification employes the ALF model with a cell size equal to the entire equiaxed grains spacing (EGS). An important distinction with the cellular model is that equiaxed grains form based on nucleation and growth mechanisms, thus do not grow according to the PSM scheme analyzed in Section 2.2. Selection among the AL, ALF or FL models is based solely on system thermodynamics.

4.4. Solid-state transformations

In Section 4.2, model comparison indicated that DICTRA provides a better approximation of the microstructural evolution in additive manufacturing, having the ability to account for non-equilibrium phenomena like epitaxial and competitive growth, to model in reference to solidification mode and morphology. In additive manufacturing, due to successive material deposition, melting and solidification phenomena are repeated as the heat source passes multiple times from all locations. From a metallurgy perspective, this behavior induces thermal cycling at every solidified material point. The DICTRA models are able to simulate the solid-state transformations that follow solidification, as the material cools down. Consequently, an in-depth analysis of both solidification and solid phase transformations upon rapid cooling and

thermal cycling conditions was conducted on the ALF model, considering the prototype thermal cycle, as determined via heat transfer simulations described in Chapter 3, from a heat transfer analysis conducted by Sotiriou et al. [53], and is pictured in Figure 4.11.

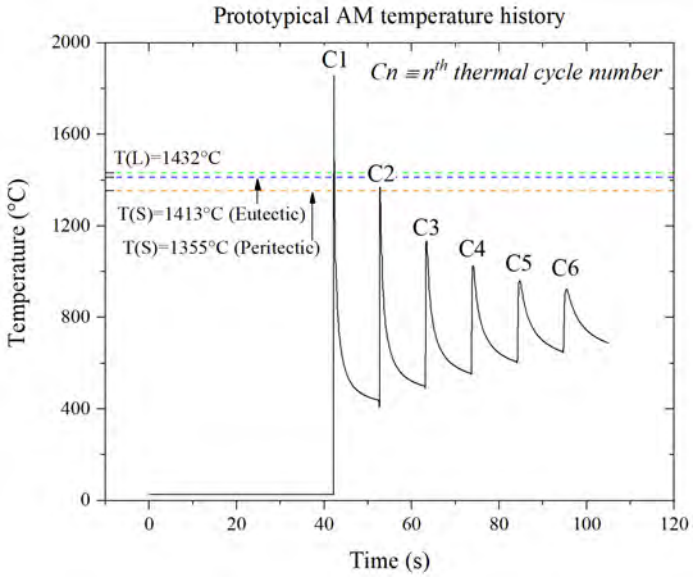

Figure 4.11. AM temperature history [53].

It was observed that the second heating cycle, due to the subsequent material deposition and laser pass, resulted in a complete remelting of the solidified microstructure. The full-remelting assumption is proved computationally in Figure 4.12(a), where above liquidus temperatures, the system melted and the melt was homogeneous. Additional laser passes did not result in melting in the examined point. Therefore, the first cycle (laser pass) was omitted in the solidification analysis and the thermal profile from the second pass to the end of the process was considered. In addition, at low temperatures below 600 °C diffusion is sluggish and thus the phase fractions and the composition profiles remain relatively stagnant, as displayed in Figure 4.12(b) from the phase fraction plateaus at low temperatures. However, significant numerical difficulties arise when integrating the diffusion equations, as the temperature decreases. For that reason, temperature sections laying lower than 600 °C, were replaced with an isothermal holding at 600 °C. Results using this simplified approach yielded no significant difference from the full approach, although they drastically decreased computational times. In Figure 4.12(b) phase fraction results of the simulation with the isothermal sections f_i^{Iso} are compared to the corresponding results from a simulation employing the initial cooling history f_i^{Lin}, revealing almost exact coincidence across the temperature field. The modified temperature history is given in Figure 4.12(c), beginning from the second thermal cycle (C2) according to Simulation assumption 1 (full remelting/melt homogenized) with sections below 600 °C being replaces with isothermal linear sections according to Simulation assumption 2 (isothermal sections).

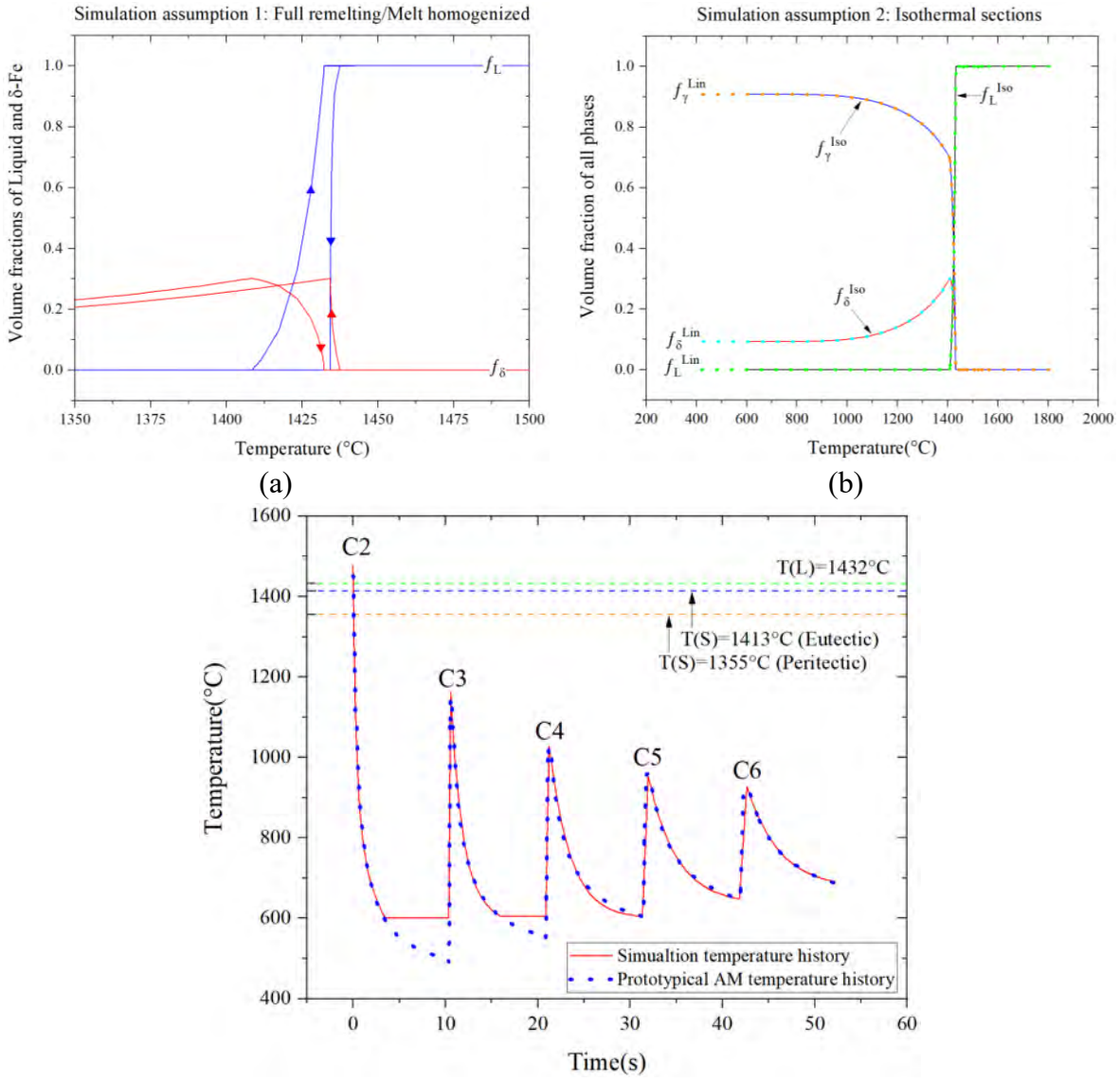

Figure 4.12. Modification of temperature history for the simulation of thermal cycling: (a) Assume full remelting above liquidus, (b) Replace all the temperature history sections below 600°C with isothermal sections and (c) comparison between prototypical and simulation temperature histories.

The kinetic analysis allows for the determination of spatial and temporal evolution of phase fractions and compositions, the presence of elemental microsegregation and the quantification of the freezing range, which are essential for the properties of the final product. The ALF model was employed to display the effects of solid-state transformations, since for all models $\delta \rightarrow \gamma$ takes place immediately after solidification. Exceptions are the AL model, that remains austenitic from the as-solidified microstructure, and FL model, where in the single δ-ferrite as-solidified microstructure, γ nucleates and grows in the region of the last melt. To simulate this evolution, an inactive γ region must be placed after solidification accordingly, and austenite will grow according to thermodynamic indication, following in the same $\delta \rightarrow \gamma$ transformation behavior. Phase fraction results of the ALF model solid-state transformations analysis are provided in Figure 4.13.

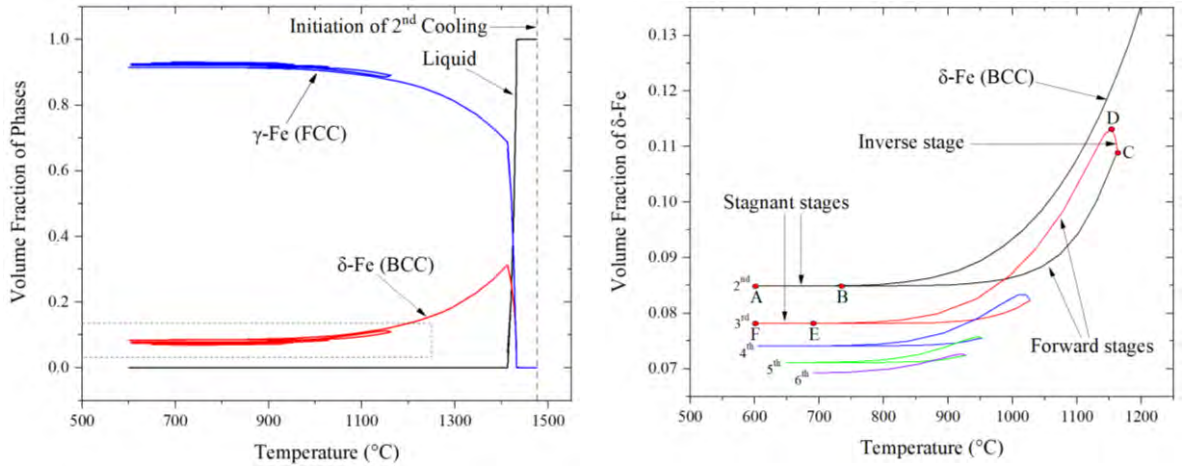

(a) (b)

Figure 4.13. (a) Variation of the volume fraction of phases with respect to temperature. (b) Magnified region depicting the evolution of the volume fraction of δ-ferrite during the thermal cycling [53].

The variation of the volume fraction of phases with respect to temperature is presented in Figure 4.13(a), after employing the thermal history given in Figure 4.12(c), in the ALF diffusion model. The dashed vertical line in Figure 4.13(a) denotes the initiation of cooling in the second thermal cycle, where a complete cycle is comprised of a cooling stage, followed by a reheating stage. It should be noted that heating in the second thermal cycle resulted in total remelting of the material and thus results regarding the first cycle can be omitted. Upon cooling in the second thermal cycle, the primary δ-ferrite phase solidifies, followed by the primary γ-austenite phase, consuming the liquid (L) phase. The growth rate of δ ferrite decreases with the formation of γ-austenite, and when the liquid phase is totally consumed, the γ austenite grows at the expense of δ-ferrite. Furthermore, hysteresis loops are formed in the volume fraction curves of both austenite and ferrite during subsequent thermal cycling. A magnified region, under the rectangular dashed area in Figure 4.14(a), is depicted in Figure 4.13(b) corresponding to the evolution of the volume fraction of δ-ferrite during thermal cycling. It is observed that upon heating in the second thermal cycle, the volume fraction of δ ferrite in part A-B remains constant, and then gradually increases in part B-C. Therefore, the parts A-B and B-C on the volume fraction curve are referred to as “stagnant” and “forward” stages, respectively [88]. A stagnant stage is defined by VOI values close to zero, as observed in Figure 4.14, where phase fractions, temperature and VOI evolve with time. During cooling in the third thermal cycle, the volume fraction of δ-ferrite in part C-D continues to increase. The part C-D on the volume fraction curve corresponds to the “inverse” stage since the volume fraction proceeds in a direction opposite to the temperature change. Upon further cooling in the 3rd cycle, the volume fraction of δ-ferrite in parts D-E and E-F evolves according to the forward and stagnant transformation, respectively. It is interesting to note that the volume fraction of δ-ferrite at the end of the cooling at each successive thermal cycle decreases, which is in accordance with the temperature change of the thermal cycling shown in Figure 4.11. Moreover, from Figure 4.14 the VOI peaks decrease with each additional thermal cycle, indicating that the oscillation of phase fraction values will reach an equilibrium state.

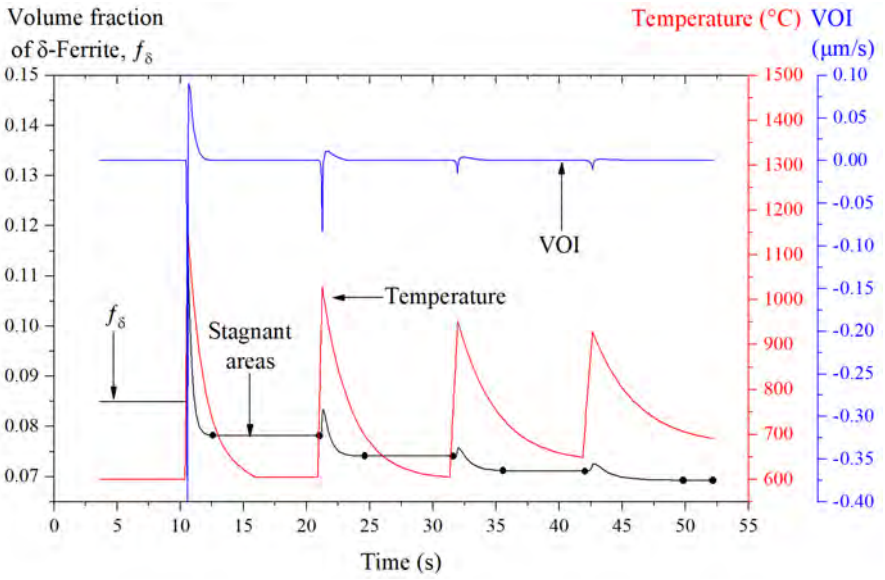

(a)

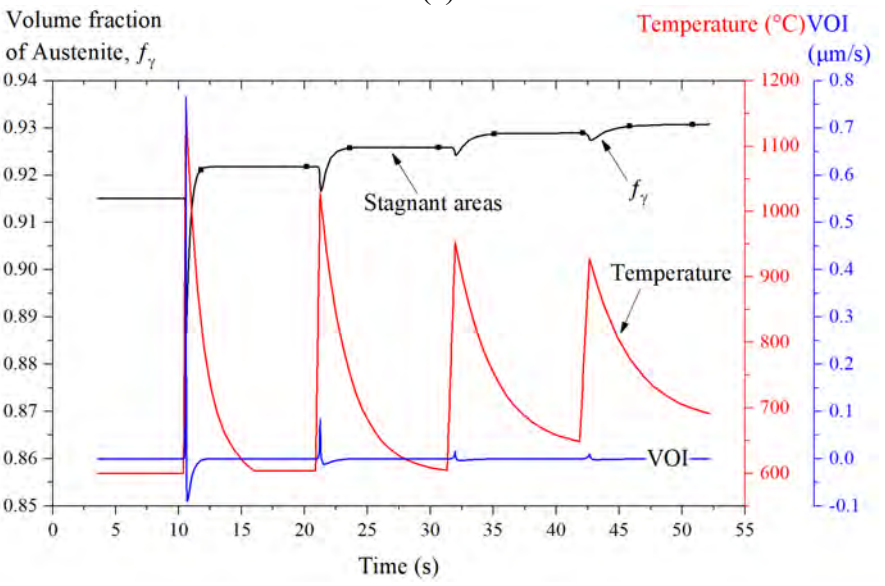

(b)

Figure 4.14. Evolution of volume fraction, Velocity of Interface (VOI) and temperature with time during thermal cycling of (a) δ-ferrite and (b) austenite.

The concentration profiles of C, Mn, Cr, Ni and Mo with respect to distance in the diffusion cell calculated with the ALF model at the end of the thermal cycling (sixth pass) are depicted in Figure 4.15(a). Partitioning of C, Mn and Ni from δ-ferrite to γ austenite takes place during the thermal cycling. The opposite partitioning behavior is observed for Cr and Mo. Therefore, at the end of thermal cycling, on the left side of the interface, the γ austenite phase is enriched in C, Mn, and Ni, whereas at the right side of the interface δ-ferrite is enriched in Cr and Mo. During the solidification, the liquid phase becomes enriched in alloying elements. However, due to the sluggish diffusion of the substitutional elements in the solid phases, microsegregation is observed in both austenite and ferrite at the end of thermal cycling. It should be noted that C does not exhibit a segregation profile in austenite and ferrite due to its higher diffusivity in these phases.

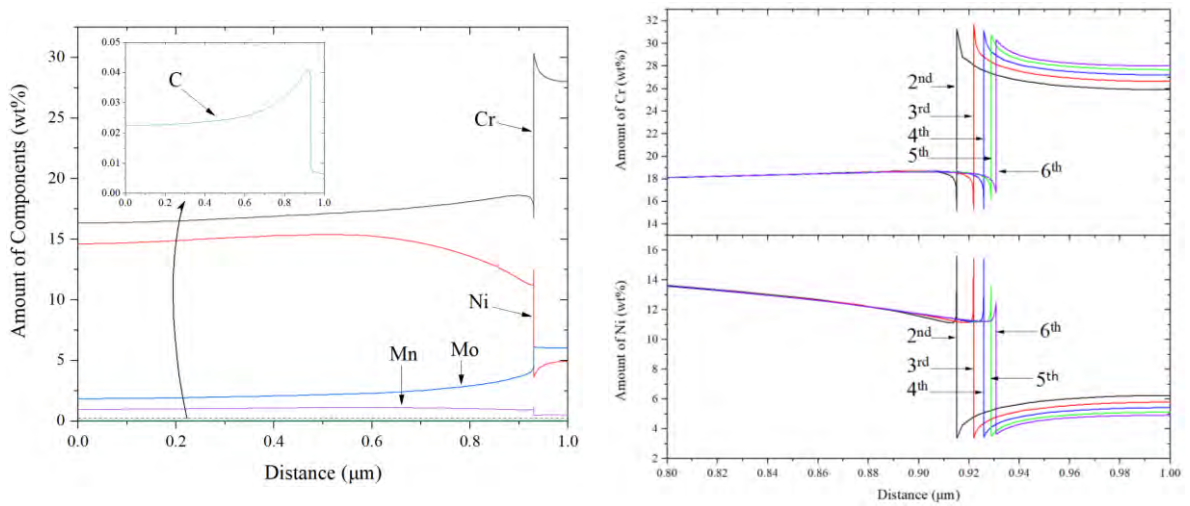

(a) (b)

Figure 4.15. (a) Concentration profiles of C, Mn, Cr, Ni and Mo at the end of the thermal cycling. (b) Concentration profiles of Cr and Ni at the end of the cooling at each thermal cycle. The austenite and ferrite regions are on the left and right of the interface respectively [53].

The concentration profiles of Cr and Ni with respect to distance at the end of cooling after each successive thermal cycle are shown in Figure 4.15(b). It is observed that the width of both Cr and Ni segregation profiles decreases at each thermal cycle, indicating that the concentrations of Cr and Ni in austenite and ferrite become homogeneous with the passage of time as diffusion takes place. In addition, the γ/δ interface is being displaced to the right by the end of each cooling cycle, resulting in the gradual decrease of the δ ferrite volume fraction, as equilibrium conditions are approached. Additionally, the concentrations of Cr in ferrite and Ni in austenite, on the interface, decrease at the last thermal cycles, following the local equilibrium conditions.

4.4.1. Thermal cycling simulation

In additive manufacturing processes in order to ensure low porosity, the layer thickness is chosen to be on the scale of (μm). Therefore, even printing of small specimens requires fusion of a lot of layers. For example, to print a cube, 1cm in height, requires 1000 layers with a layer thickness of 10 μm. Therefore, the solidified material is subjected to thermal cycling as the heat source moves across layer-by-layer. Calculation of the transient temperature evolution with high fidelity requires in-depth modeling of the heat transfer problem, as discussed in Chapter 3. Presently, the extended effect of thermal cycling on microstructural evolution is examined, employing the ALF model.

This investigation expanded the prototype temperature history of Figure 4.11, simulating the printing of additional layers for 2000 s, in three approximations as presented in Figure 4.16, with the objective to identify the effect of multi-layer printing on the microstructure. The first approximation considers an expansion of the temperature history using a sinusoidal function and is given in Figure 4.16(a), with amplitude and frequency derived from the 6^{th} cycle of the prototype profile. The second approximation includes an amplitude damping factor in the harmonic expansion of the first approximation, shown in Figure 4.16(c) to model for the additional material deposition as the printing continues, while the third approximation considers the isothermal approximation resulting from the evolution of the temperature cycling mean value (constant by definition in the present case) and is presented in Figure 4.16(e).

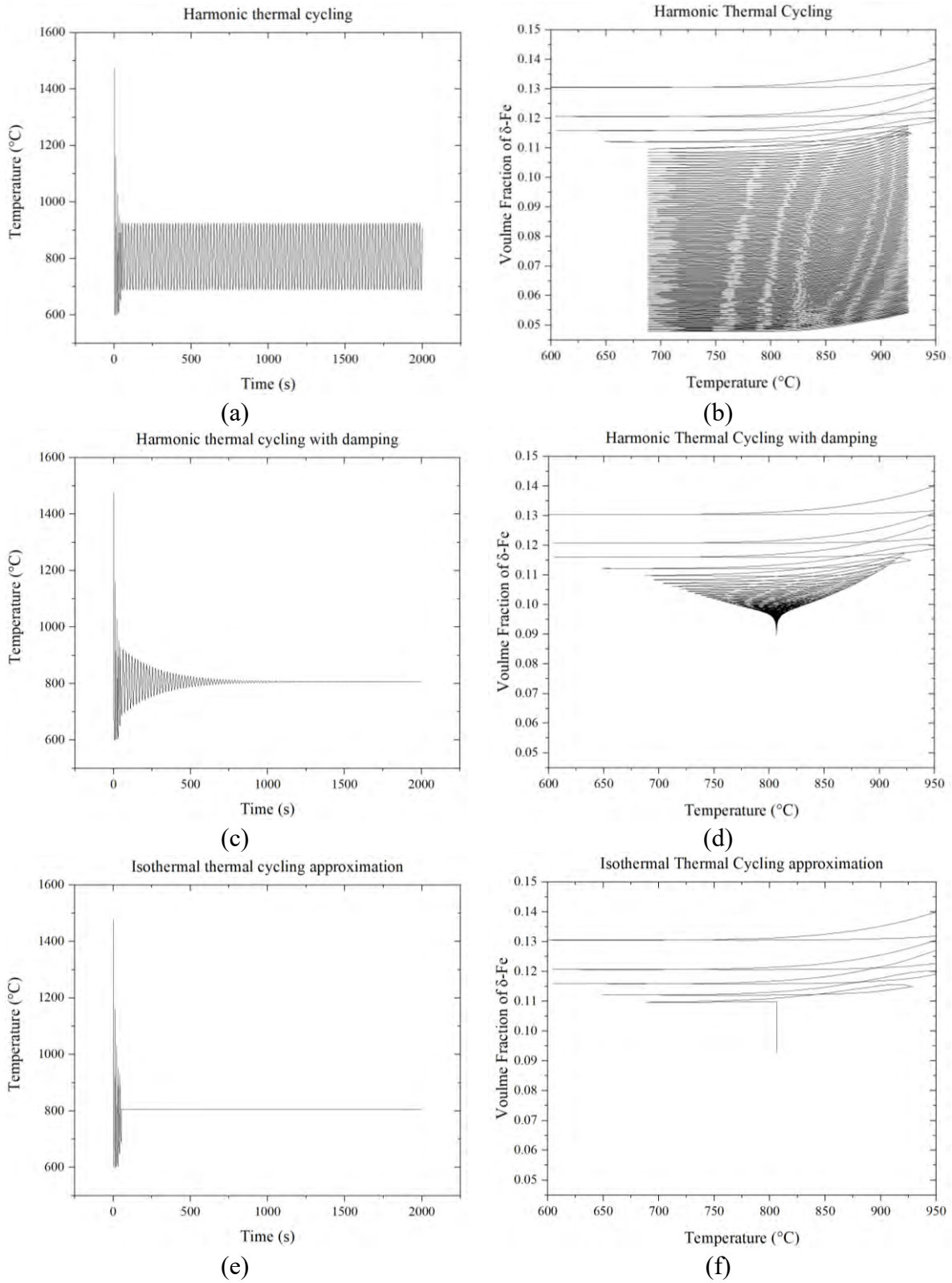

Figure 4.16. Thermal cycling temperature history approximations and resulting δ-ferrite fraction evolutions: (a) Sinusoidal expansion approximation, (b) harmonic approximation with damping and (c) isothermal approximation at mean value of oscillation.

In all cases, the volume fraction of δ-ferrite decreases with time, as presented in Figures 4.16(b),(d) and (f), with the system moving towards the equilibrium status of the evolving mean value of cycling. Comparison is conducted in terms of δ-ferrite fractions, with austenite being

complementary of the system. The Harmonic Thermal Cycling, predicts the lowest δ-ferrite fraction of less than 5 vol%, since constant temperature range enables diffusion to accelerate $\delta \rightarrow \gamma$ transformation kinetics. Introduction of the damping factor in Figure 4.16(d), constitutes a more accurate representation of additive manufacturing, since more material is deposited above the reference material point, absorbing increasingly the constant amount of directed heat. The temperature cycling damping retards $\delta \rightarrow \gamma$ transformation kinetics due to diffusion becoming increasingly sluggish under a continuously decreasing temperature range, with the simulation predicting a δ-ferrite fraction close to 9 vol%.

The isothermal approximation of Figure 4.16(e) was introduced to provide a simple modeling alternative to the computationally demanding harmonic/damping model. The simulation reached a fraction of δ-ferrite very close to the prediction of Figure 4.16(d), resulting in a successful simplification of modeling. Resulting as-cast segregation profiles were also quantitatively similar. The effect of thermal cycling on the segregation of Cr and Ni is presented in Figure 4.17. Comparison between the as-solidified and as-cast microstructure, besides showing the evolution of $\delta \rightarrow \gamma$ transformation, reveals a significant segregation of both elements in austenite that increases with time, as diffusion is not able to afflict effective solute redistribution. On the other hand, δ-ferrite is almost fully homogenized, because of its higher diffusivity and smaller region size. The diagrams of Figure 4.17 state the importance of solid-state transformations and their simulation in the framework of microstructural evolution in additive manufacturing. Comparison of thermal multi-cycling models indicated the efficiency of the mean value approximation in approaching the effect of multiple thermal cycles upon microstructural evolution.

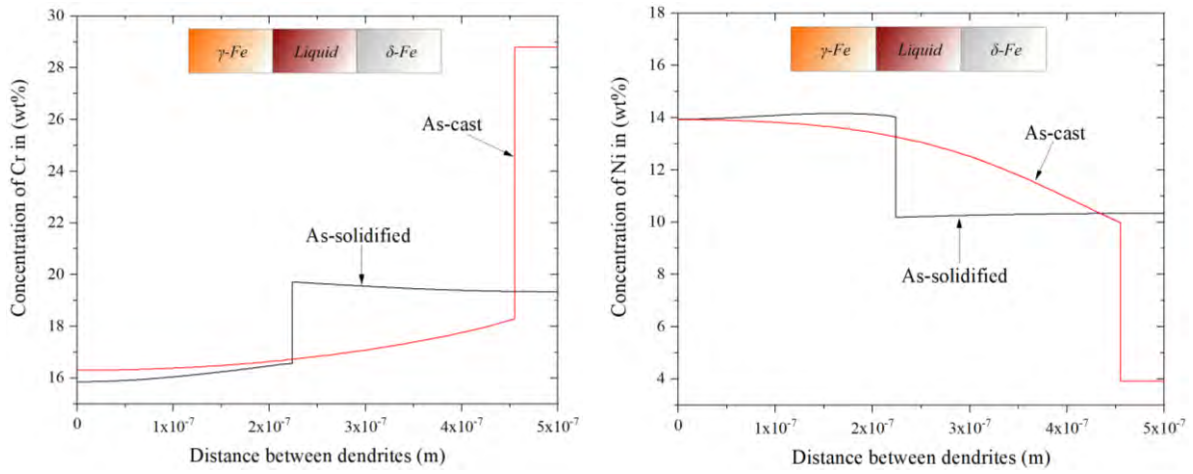

(a) (b)

Figure 4.17. Comparison of as-solidified and as-cast segregation profiles for harmonic thermal cycling with damping in ALF model. (a) Cr and (b) Ni.

4.5. Calculation of non-equilibrium thermophysical properties

Accurate simulation of the transient heat transfer in selective laser melting required development of a rapid cooling model to calculate temperature-dependent non equilibrium thermophysical properties. CALPHAD-based microstructural evolution models were employed to simulate solidification and subsequent solid-state transformations upon the applied temperature gradients. A prototype cooling path was considered, as calculated in [53] to act as a first-degree approximation of the actual cooling behavior. Multi-component and multi-phase, one-dimensional mass transfer calculations were performed in the DICTRA

module of Thermo-Calc [22], utilizing thermodynamic and mobility information provided in the TCFE11 and MOBFE2 databases respectively.

A planar geometry cell with 0.5 μm length was considered as a representative elementary structure, accounting for the transverse evolution of the primary dendrites (cells) that constitute the dominant microstructural feature. Initially, the cell was comprised of a single liquid region. In contrast with previous attempts to describe the behavior of the benchmark AISI 316L [53,75], austenite was considered to be the single solidifying phase (AL model), ignoring the effect of ferrite in eutectic or peritectic solidification. Thus, an inactive γ-austenite region was modeled adjacent to the liquid and separated by a moving interface. The reasoning behind omitting δ-ferrite from the simulation is that under extreme cooling rates, dendritic epitaxial growth regulates the microstructural evolution and promotes exclusive austenite (stable in a lower temperature range) growth through elevated solidification velocities. The nucleation stage is omitted from the analysis since only diffusion-controlled transformations are considered in DICTRA.

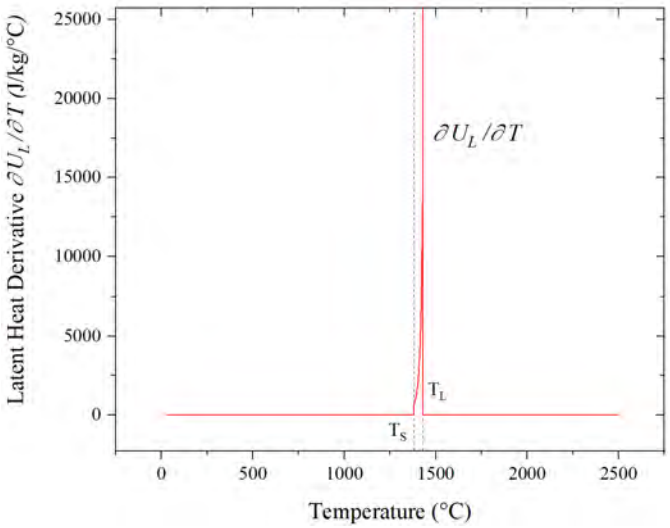

Figure 4.18. Temperature derivative of latent heat $\partial U_L(T)/\partial T$

Non-equilibrium thermophysical properties were predicted for a temperature range spanning from 27°C to 2500°C based on the calculated phase fractions and compositions from the DICTRA simulations using the first-degree approximation of the cooling curve. Density ρ, specific heat capacity c_p and latent heat U_L were computed directly from Thermo-Calc, for the non-equilibrium segregation profiles during cooling and then the transient thermophysical properties were calculated as a function of temperature by means of integration over the diffusion cell domains. In Figure 4.18 the temperature derivative of the latent heat is given as a function of temperature. The derivative was computed from changes in the enthalpy of liquid phase, as computed in Thermo-Calc for a system with mean compositional values of the liquid region in the DICTRA simulation. The latent heat was determined after numerical integration of its first temperature derivative that was calculated from changes in enthalpy, as given in Figure 4.18. Finally, for the thermal conductivity k the derived expressions from [55], extended using the specific liquidus and solidus, were incorporated in the analysis since the employed databases lack information regarding conductivity. The results were obtained in terms of terminal phase fractions and constitutions. The calculated non-equilibrium,

temperature/microstructure-dependent thermophysical properties for the reference 316L system are given in Figure 4.19.

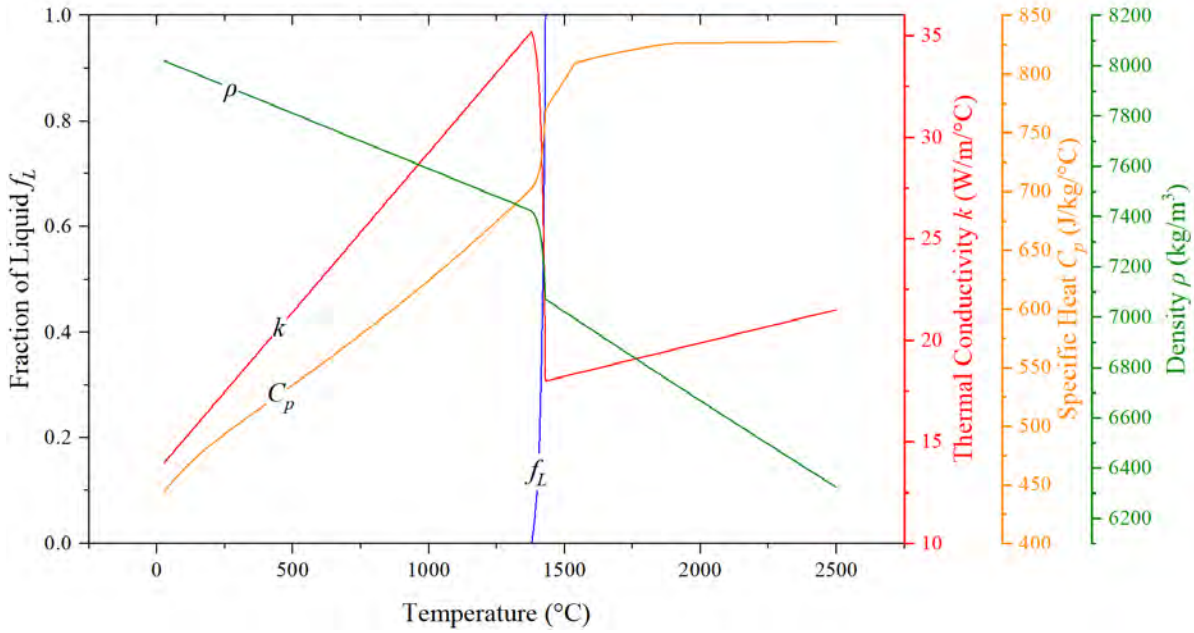

Figure 4.19. Non-equilibrium temperature/microstructure dependent thermophysical properties: Thermal conductivity $k(T)$, specific heat $c_p(T)$, density $\rho(T)$ and fraction of liquid $f_L(T)$.

As the temperature drops, in all thermophysical properties there are three distinct regions that exhibit uniform behaviors: For temperatures below solidus, for temperatures above liquidus and for temperatures between solidus and liquids. The change of state that takes place during solidification drastically affects the thermophysical properties. In the melt state, the system exhibits increasing conductivity and specific heat with temperature, and a reduction of density. When solidification begins, the forming crystal structure leads to an increase in all properties. The solidified system exhibits opposite behavior of all thermophysical properties with temperature, compared to the melt state.

Chapter 5. Results and discussion

5.1. SLM of benchmark AISI 316L austenitic stainless steel

Selective laser melting was simulated following an integrated methodology that involved heat transfer calculations coupled with microstructural evolution models to capture the microstructural evolution of the benchmark AISI 316L [12] stainless steel specimen. Temperature contour plots throughout the building process are given in Figure 5.1. The heat source is moving left to right, melting the powder layer. During the cooling period, as seen in Figures 5.1(c), (f), the temperature quickly homogenizes and then the next layer begins. Above the building layer -with dark blue color- are the quiet elements. This process repeats until the built is complete. Temperature results for three middle material points at different built heights are presented in Figure 5.1(a). Every material point is subjected to melting and rapid cooling followed by a thermal cycling behavior which culminates in slow cooling to ambient temperature after the end of the process. It is evident that under the given process parameters, each node melted and solidified twice, enabling joining of the deposited material with the previous layers.

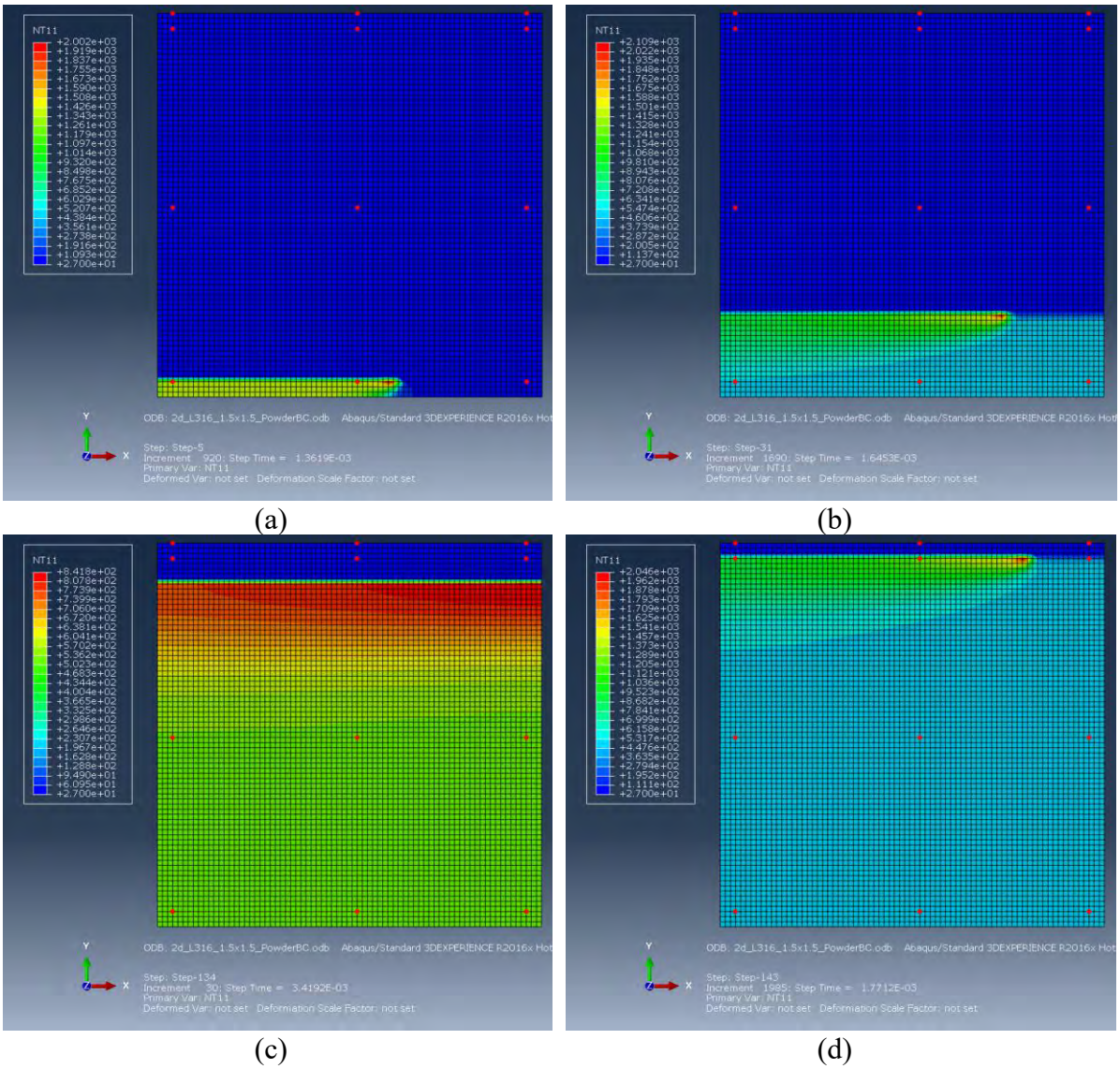

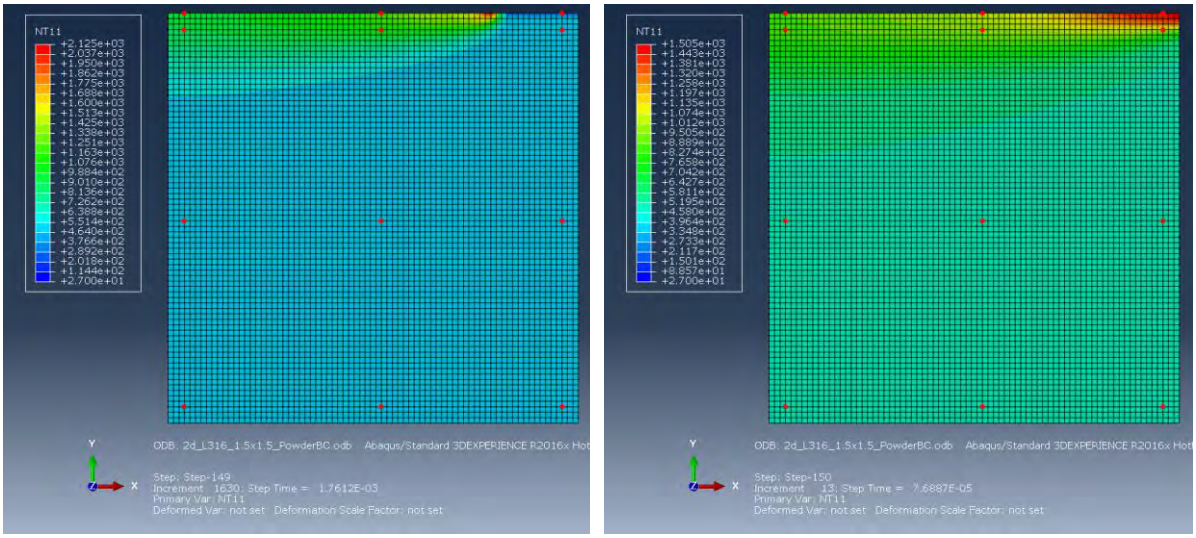

(e) (f)

Figure 5.1. Evolution of temperature history in the wall: (a), (b), (d), (e) Heating stages and (c), (f) cooling stages.

Initially, heat accumulation takes place upon subsequent laser passes, as the boundary conditions cannot remove heat efficiently, as indicated by the rise of the minimum thermal-cycle temperatures. However, after 520°C a steady decrease is noticed. Modeling provided several insights as well, regarding short-lived and transient heat transfer phenomena taking place during printing. In Figure 5.2(b), the first thermal cycle for central node 2852 (N2858) is presented. Notice that ambient-temperature powder is subjected to pre-heating, due to heat influx from the previously built layer that has an elevated temperature. Recalescence -the effect of latent heat on the temperature profile- appears, controlling the heating rate during melting and cooling rate during solidification. Moreover, each cooling stage exhibits a change of rate, from rapid cooling initially, to a very gradual cooling controlled by heat dissipation via the boundary surfaces. This is signified by conduction within the specimen, transferring heat more efficiently than free-surface areas can reject toward the environment. Evidently, the built specimen becomes saturated in heat (no internal temperature gradients) and thus the total rate of cooling decreases. At this stage the temperature profiles of all material points coincide, as observed in Figure 5.2(a).

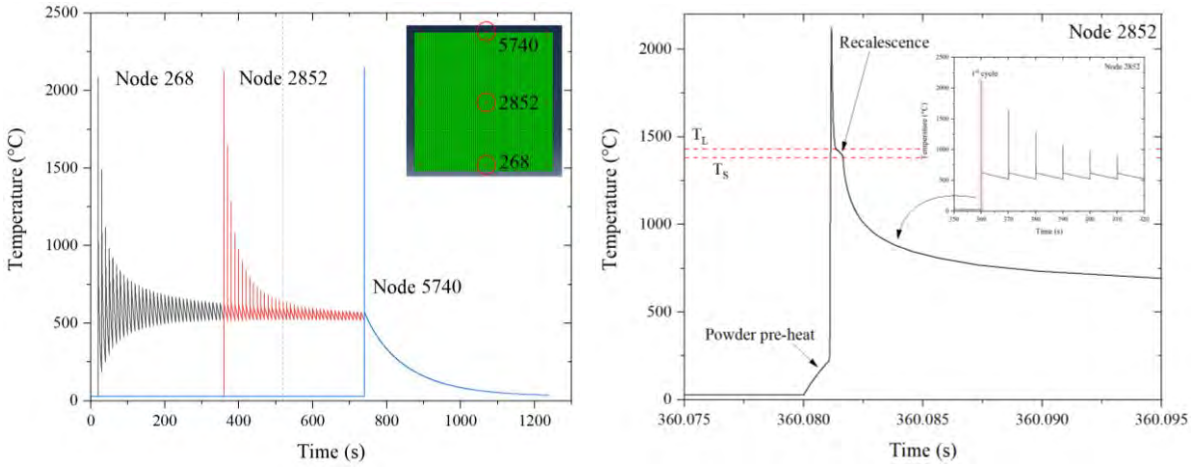

(a) (b)

Figure 5.2. Temperature history results: (a) Spatial comparison and (b) first temperature cycle node 2858.

Figure 5.3(a) shows a detail in the temperature history of node 2852, concentrating on the second temperature cycle (designated C2). The first important detail is that before the heat source hits the material point, the material exhibits a damping in temperature, due to heat transfer directed upwards, towards the cold deposited powder. In the following heating stage, the material melts, achieving temperatures higher than liquidus, thus ensuring effective incorporation as discussed in Chapter 3. Then during the cooling stage, there are two disturbances in the cooling rate: The first is due to the recalescence effect of the material in the elements below the present node 2858, where the absorption of excess heat by solidification reduces the cooling rate. The second disturbance coincides with the solidification of the material in the elements above node 2858, causing an additional damping in the cooling rate due to recalescence.

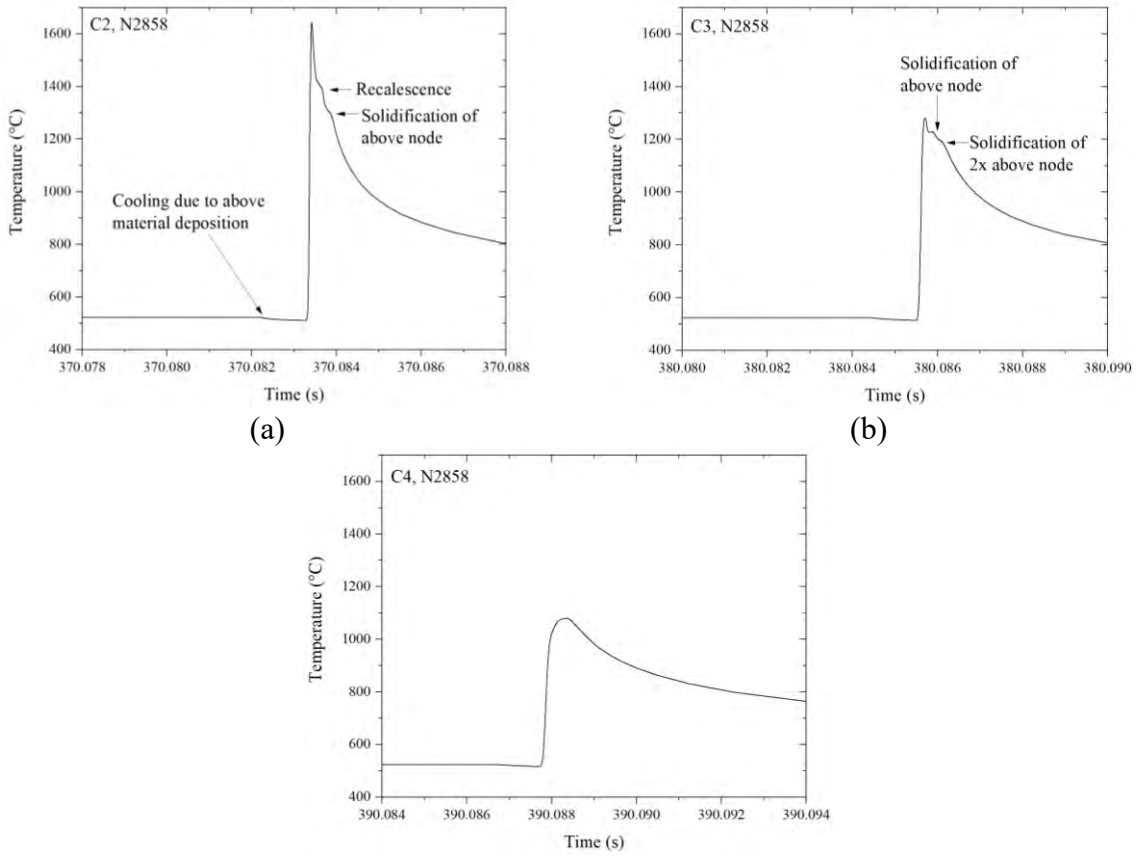

Figure 5.3. Effect of latent heat (recalescence) below the melt pool: (a) Close to the melt pool periphery, (b) one layer thickness away and (b) two layers away.

In Figure 5.3(b), the material does not melt or solidify, however two disturbances are also present in the cooling path, corresponding to solidification of above and next from above layers. Finally, this phenomenon fades completely at the fourth thermal cycle, as pictured in Figure 5.3(c). In addition, in all thermal cycles a slight drop in temperature is observed prior to heating commence, corresponding to deposition of the new powder layer, which is heated by the hot substrate, lowering the temperature of the layers below, according to Figure 5.3(a).

The temperature profile of node 2852, a central node on the mesh, was employed as a representative example, to calculate the microstructural evolution. Since the diffusion cell consists of austenite as the single solid phase, the solidification path in Figure 5.4(a) does not

exhibit cyclic behavior as observed in δ-ferrite-containing systems [53]. However, a decrease in the solidus temperature compared to thermodynamics, at 1300.4 °C due to diffusion, leads to an increase of the freezing range by almost 70 °C in comparison to the model used for the thermophysical properties calculations, with the additional range covering less than 1% of solidification. Interestingly, this behavior could not be simulated with the limit case of Scheil-Gulliver approach as described in [53], due to simulation termination criteria.

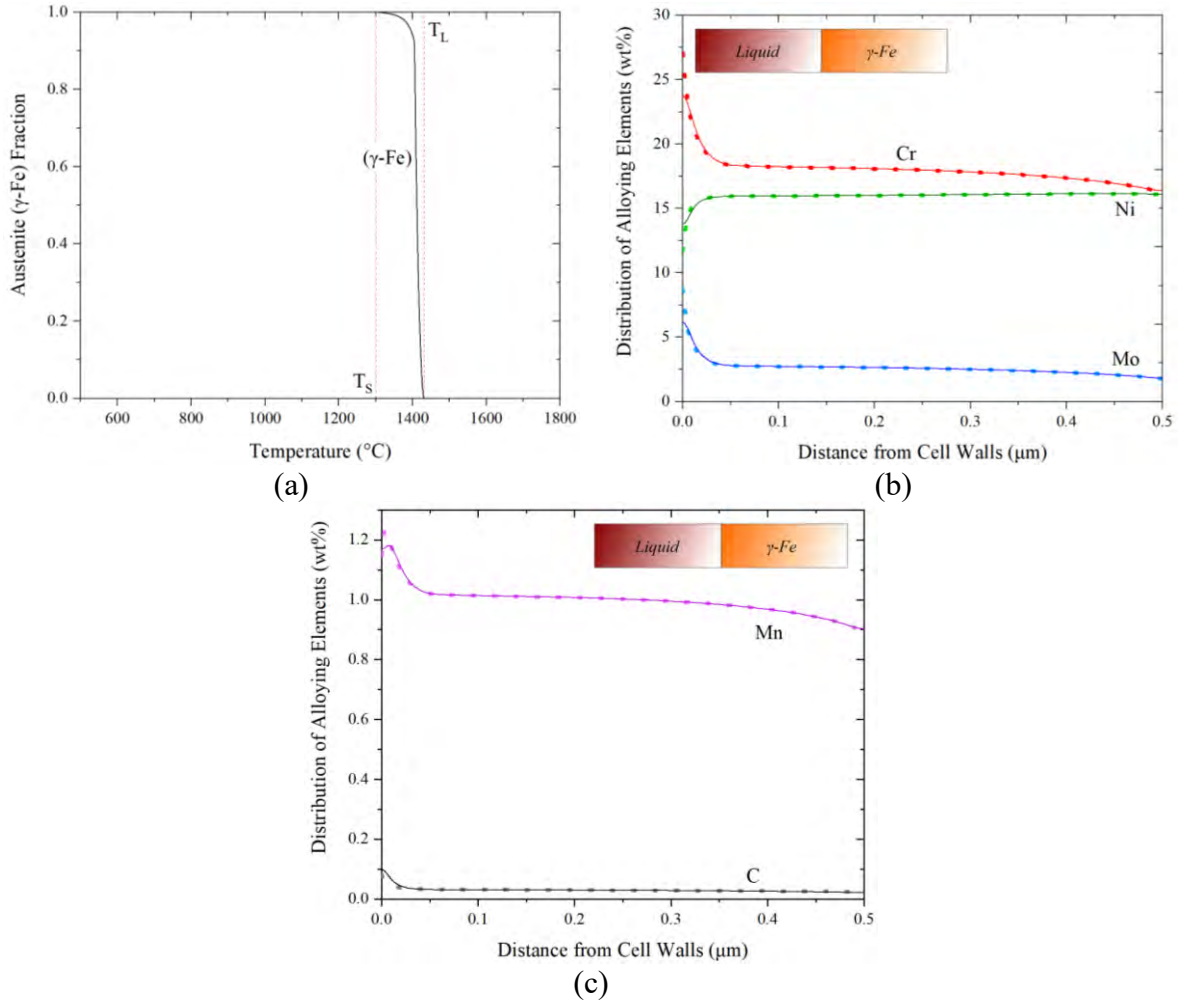

Figure 5.4. Microstructural analysis results: (a) Austenite fraction evolution with respect to temperature and (b), (c) alloying elements segregation profiles. Dashed lines correspond to post-solidification and full line to end of process profiles.

Finally, Figures 5.4(b)-(c) illustrate the evolution of microsegregation profiles after the solidification (dashed lines) and up to the end of the process (solid lines). Cr and Mo tend to transfer away from austenite and segregate to the dendrite walls, in accordance with [53,75]. A decrease in segregation is observed for all alloying elements as the effect of thermal cycling upon subsequent laser passes for the deposition of new layers. Chromium microsegregation results are similar to values provided by EDS experimental information conducted in [12], 20-22 wt% Cr in a region near the cell wall and 17 wt% Cr towards the cell core. The resulting microstructural information together with the temperature history can be provided as input for a mechanical analysis in order to calculate the residual stress field as well as the terminal mechanical properties of as-built AISI 316L SLM products.

Chapter 6. Conclusions and future work

The objective of the present thesis was to achieve an insight in the phenomena that determine the microstructural evolution of austenitic stainless steels in additive manufacturing. Summarizing, the following remarks can be made:

- Thermodynamics and kinetics of solidification in austenitic stainless steels were investigated. A distinction between eutectic and peritectic solidification modes was made, as both have been observed in AM studies.
- The effects of the cooling rate on the microstructural evolution were determined and transition criteria for solidification mode and morphology were established using the KGT dendrite growth theory.
- A 2D heat transfer modeling methodology was developed both for powder bed (PB) and powder deposition (PD) additive manufacturing techniques taking into account the effect of material powder, accounting for the phase transitions, latent heat, forced convection anemometry and Marangoni flow in the melt pool.
- Transient heat transfer analysis employed non-equilibrium thermophysical properties to calculate temperature profiles with high fidelity.
- Solidification and solid-phase transformations upon rapid cooling and thermal cycling, were studied via ICME tools including equilibrium analysis, Scheil-Gulliver and multi-component diffusion simulations. Phase fractions and composition profiles were calculated as a function of time, allowing the determination of the non-equilibrium solidus temperature, the freezing range, as well as the presence of elemental segregation.
- A CALPHAD modeling framework of solidification and solid-state transformations upon thermal cycling was developed, to consider the variance in solidification type (alloy composition), cooling rate (from the electric arc to laser beams) and growth mechanism (epitaxial growth, nucleation and growth).
- An integrated methodology of modeling and simulation of SLM in a benchmark 316L austenitic stainless steel was established. The diffusion model determined the microstructural constitution in accordance with literature experimental results.

The following suggestions for future research may be considered, based on the results of the present study:

- Validation of the entire spectrum of microstructural evolution models presented via in-situ measurements of phase fractions and spatial/temporal distribution of alloying elements, in order to experimentally verify the transition boundaries among the modeling options.
- 3D expansion of the heat transfer model to include scanning strategy, hatch spacing and other additive manufacturing building parameters in the modeling.
- Investigation of the transient temperature field inside the melt pool to study the morphology transitions.
- Explore alternate modeling options (e.g., phase-field) for the simulation of the microstructural evolution within an ICME framework to work towards sustainable microstructure prediction tools for AM applications.

References

[1] M. Markl, C. Körner, Multiscale Modeling of Powder Bed–Based Additive Manufacturing, Annu Rev Mater Res. 46 (2016) 93–123. https://doi.org/10.1146/annurev-matsci-070115-032158.

[2] M. Gouge, P. Michaleris, Chapter 1 - An Introduction to Additive Manufacturing Processes and Their Modeling Challenges, in: M. Gouge, P. Michaleris (Eds.), Thermo-Mechanical Modeling of Additive Manufacturing, Butterworth-Heinemann, 2018: pp. 3–18. https://doi.org/https://doi.org/10.1016/B978-0-12-811820-7.00002-1.

[3] W. Gao, Y. Zhang, D. Ramanujan, K. Ramani, Y. Chen, C.B. Williams, C.C.L. Wang, Y.C. Shin, S. Zhang, P.D. Zavattieri, The status, challenges, and future of additive manufacturing in engineering, CAD Computer Aided Design. 69 (2015) 65–89. https://doi.org/10.1016/j.cad.2015.04.001.

[4] E. Louvis, P. Fox, C.J. Sutcliffe, Selective laser melting of aluminium components, J Mater Process Technol. 211 (2011) 275–284. https://doi.org/10.1016/J.JMATPROTEC.2010.09.019.

[5] H. Peng, M. Ghasri-Khouzani, S. Gong, R. Attardo, P. Ostiguy, B.A. Gatrell, J. Budzinski, C. Tomonto, J. Neidig, M.R. Shankar, R. Billo, D.B. Go, D. Hoelzle, Fast prediction of thermal distortion in metal powder bed fusion additive manufacturing: Part 1, a thermal circuit network model, Addit Manuf. 22 (2018) 852–868. https://doi.org/10.1016/J.ADDMA.2018.05.023.

[6] H. Peng, M. Ghasri-Khouzani, S. Gong, R. Attardo, P. Ostiguy, R.B. Rogge, B.A. Gatrell, J. Budzinski, C. Tomonto, J. Neidig, M.R. Shankar, R. Billo, D.B. Go, D. Hoelzle, Fast prediction of thermal distortion in metal powder bed fusion additive manufacturing: Part 2, a quasi-static thermo-mechanical model, Addit Manuf. 22 (2018) 869–882. https://doi.org/10.1016/J.ADDMA.2018.05.001.

[7] P. Köhnen, M. Létang, M. Voshage, J.H. Schleifenbaum, C. Haase, Understanding the process-microstructure correlations for tailoring the mechanical properties of L-PBF produced austenitic advanced high strength steel, Addit Manuf. 30 (2019) 100914. https://doi.org/10.1016/J.ADDMA.2019.100914.

[8] T. DebRoy, H.L. Wei, J.S. Zuback, T. Mukherjee, J.W. Elmer, J.O. Milewski, A.M. Beese, A. Wilson-Heid, A. De, W. Zhang, Additive manufacturing of metallic components – Process, structure and properties, Prog Mater Sci. 92 (2018) 112–224. https://doi.org/10.1016/J.PMATSCI.2017.10.001.

[9] P. Bajaj, A. Hariharan, A. Kini, P. Kürnsteiner, D. Raabe, E.A. Jägle, Steels in additive manufacturing: A review of their microstructure and properties, Materials Science and Engineering A. 772 (2020). https://doi.org/10.1016/j.msea.2019.138633.

[10] C. Zitelli, P. Folgarait, A. Di Schino, Laser powder bed fusion of stainless steel grades: A review, Metals (Basel). 9 (2019). https://doi.org/10.3390/met9070731.

[11] M.P. Sotiriou, J.S. Aristeidakis, S.A. Koimtzidis, I. Papadioti, M.-I.T. Tzini, G.N. Haidemenopoulos, N. Aravas, Microstructural and heat transfer modeling of selective laser melting in austenitic stainless steels, (2022).

[12] K.M. Bertsch, G. Meric de Bellefon, B. Kuehl, D.J. Thoma, Origin of dislocation structures in an additively manufactured austenitic stainless steel 316L, Acta Mater. 199 (2020) 19–33. https://doi.org/10.1016/j.actamat.2020.07.063.

[13] J.C. Lippold, D.J. Kotecki, Welding Metallurgy and Weldability of Stainless Steels, 2005.

[14] S. Kou, Welding metallurgy, 2nd ed., 2003.

[15] J.A. Brooks, J.C. Lippold, Selection of Wrought Austenitic Stainless Steels, in: Welding, Brazing, and Soldering, 2018. https://doi.org/10.31399/asm.hb.v06.a0001410.

[16] D. Kong, C. Dong, S. Wei, X. Ni, L. Zhang, R. Li, L. Wang, C. Man, X. Li, About metastable cellular structure in additively manufactured austenitic stainless steels, Addit Manuf. 38 (2021) 101804. https://doi.org/10.1016/j.addma.2020.101804.

[17] R.P. Reed, Nitrogen in austenitic stainless steels, JOM. 41 (1989) 16–21. https://doi.org/10.1007/BF03220991.

[18] Metals Handbook Desk Edition, ASM International, 1998. https://doi.org/10.31399/asm.hb.mhde2.9781627081993.

[19] B.J. Sutton, Development of a primary solidification mode diagram for austenitic stainless stell weld metals using CALPHAD-based modeling, 2021.

[20] C. Sofras, J. Čapek, A. Arabi-Hashemi, C. Leinenbach, M. Frost, K. An, R.E. Logé, M. Strobl, E. Polatidis, Tailored deformation behavior of 304L stainless steel through control of the crystallographic texture with laser-powder bed fusion, Mater Des. 219 (2022). https://doi.org/10.1016/j.matdes.2022.110789.

[21] C. Herriott, X. Li, N. Kouraytem, V. Tari, W. Tan, B. Anglin, A.D. Rollett, A.D. Spear, A multi-scale, multi-physics modeling framework to predict spatial variation of properties in additive-manufactured metals, Model Simul Mat Sci Eng. 27 (2019) 25009. https://doi.org/10.1088/1361-651X/aaf753.

[22] J.O. Andersson, T. Helander, L. Höglund, P. Shi, B. Sundman, Thermo-Calc & DICTRA, computational tools for materials science, Calphad. 26 (2002) 273–312. https://doi.org/10.1016/S0364-5916(02)00037-8.

[23] ASM_Handbook, (n.d.).

[24] C. Wu, S. Li, C. Zhang, X. Wang, Microstructural evolution in 316LN austenitic stainless steel during solidification process under different cooling rates, J Mater Sci. 51 (2016) 2529–2539. https://doi.org/10.1007/s10853-015-9565-0.

[25] P. Yu, K.J. Thompson, J. McCarthy, S. Kou, Microstructure evolution and solidification cracking in austenitic stainless steel welds, Weld J. 97 (2018) 301S-314S. https://doi.org/10.29391/2018.97.026.

[26] M. Yonemura, T. Osuki, H. Terasaki, Y. Komizo, M. Sato, A. Kitano, In-situ observation for weld solidification in stainless steels using time-resolved X-ray diffraction, Mater Trans. 47 (2006) 310–316. https://doi.org/10.2320/matertrans.47.310.

[27] J. Goldak, A. Chakravarti, M. Bibby, A new finite element model for welding heat sources, Metallurgical Transactions B. 15 (1984) 299–305. https://doi.org/10.1007/BF02667333.

[28] S. Elena-Manuela, A. Păvălache, D. Gabriel, O. Dontu, B. Daniel, I. Vasile, Mechanism of keyhole formation in laser welding, Romanian Review Precision Mechanics, Optics and Mechatronics. (2010).

[29] J.W. Elmer, S.M. Allen, T.W. Eagar, Microstructural development during solidification of stainless steel alloys, Metallurgical Transactions A. 20 (1989) 2117–2131. https://doi.org/10.1007/BF02650298.

[30] M.C. Flemings, Solidification Processing, in: Materials Science and Technology, 2006. https://doi.org/10.1002/9783527603978.mst0173.

[31] S. Katayama, A. Matsunawa, Solidification Microstructure of Laser Welded Stainless Steels., LIA (Laser Institute of America). 43–48 (1985) 60–67. https://doi.org/10.2351/1.5057623.

[32] H. Inoue, T. Koseki, Solidification mechanism of austenitic stainless steels solidified with primary ferrite, Acta Mater. 124 (2017) 430–436. https://doi.org/10.1016/j.actamat.2016.11.030.

[33] J.W. Elmer, The Influence of Cooling Rate on the Microstructure of Stainless Steel Alloys, 1988.

[34] A.L. SCHAEFFLER, Constitution Diagram for Stainless Steel Weld Metal, Metal Progress. 56 (1949) 680. https://cir.nii.ac.jp/crid/1570009751069526400.

[35] W.T. Delong, Ferrite in austenitic stainless steel weld metal, Weld J (NY). 53 (1974) 273s–286s. http://inis.iaea.org/search/search.aspx?orig_q=RN:05151661.

[36] D.J. Kotecki, T. a. Siewert, WRC-1992 Constitution Diagram for Stainless Steel Weld Metals : A Modification of the WRC-1988 Diagram, AWS Annual Meeting. (1992) 171–178. http://www.aws.org/wj/supplement/WJ_1992_05_s171.pdf.

[37] J.W. Fu, Y.S. Yang, J.J. Guo, J.C. Ma, W.H. Tong, Microstructure evolution in AISI 304 stainless steel during near rapid directional solidification, Materials Science and Technology. 25 (2009) 1013–1016. https://doi.org/10.1179/174328408X317093.

[38] J.C. Lippold, Solidification Behavior and Cracking Susceptibility of Pulsed-Laser Welds in Austenitic Stainless Steels A shift in solidification behavior under rapid solidification conditions promotes an increase in cracking susceptibility, n.d.

[39] F. Mas, C. Tassin, F. Roch, M. Yescas, P. Todeschini, Y. Bréchet, Growth morphologies and primary solidification modes in a dissimilar weld between a low-alloy steel and an austenitic stainless steel, Metals (Basel). 8 (2018). https://doi.org/10.3390/met8040284.

[40] J. Singh, G.R. Purdy, G.C. Weatherly, Microstructural and microchemical aspects of the solid-state decomposition of delta ferrite in austenitic stainless steels, Metallurgical Transactions A. 16 (1985) 1363–1369. https://doi.org/10.1007/BF02658669.

[41] S.A. David, J.M. Vitek, R.W. Reed, T.L. Hebble, Effect of rapid solidification on stainless steel weld metal microstructures and its implications on the Schaeffler diagram, United States, 1987. https://doi.org/10.2172/5957599.

[42] J.C. Lippold, Centerline cracking in deep penetration electron beam welds in type 304L stainless steel, 64:5 (1985). https://www.osti.gov/biblio/5044947.

[43] N. Suutala, Effect of solidification conditions on the solidification mode in austenitic stainless steels, Metallurgical Transactions A. 14 (1983) 191–197. https://doi.org/10.1007/BF02651615.

[44] R. Trivedi, W. Kurz, Theory of Microstructural Development During Rapid Solidification., NATO ASI Series, Series E: Applied Sciences. 34 (1986) 260–267. https://doi.org/10.1007/978-94-009-4456-5_24.

[45] R. Trivedi, W. Kurz, Solidification microstructures: A conceptual approach, Acta Metallurgica Et Materialia. 42 (1994) 15–23. https://doi.org/10.1016/0956-7151(94)90044-2.

[46] T. Voisin, J.B. Forien, A. Perron, S. Aubry, N. Bertin, A. Samanta, A. Baker, Y.M. Wang, New insights on cellular structures strengthening mechanisms and thermal stability of an austenitic stainless steel fabricated by laser powder-bed-fusion, Acta Mater. 203 (2021). https://doi.org/10.1016/j.actamat.2020.11.018.

[47] S. Astafurov, E. Astafurova, Phase composition of austenitic stainless steels in additive manufacturing: A review, Metals (Basel). 11 (2021). https://doi.org/10.3390/met11071052.

[48] G.P. Ivantsov, Diffusion Supercooling during the Solidification of a Binary Alloy, in: Dokl. Akad. Nauk SSSR, 1951: pp. 179–182.

[49] J.A. Dantzig, M. Rappaz, Solidification: -Revised \& Expanded, EPFL press, 2016.

[50] P. Mohammadpour, A. Plotkowski, A.B. Phillion, Revisiting solidification microstructure selection maps in the frame of additive manufacturing, Addit Manuf. 31 (2020) 100936. https://doi.org/10.1016/j.addma.2019.100936.

[51] J.D. Hunt, Steady state columnar and equiaxed growth of dendrites and eutectic, Materials Science and Engineering. 65 (1984) 75–83. https://doi.org/10.1016/0025-5416(84)90201-5.

[52] W. Löser, D.M. Herlach, Theoretical treatment of the solidification of undercooled Fe-Cr-Ni melts, Metallurgical Transactions A. 23 (1992) 1585–1591. https://doi.org/10.1007/BF02647340.

[53] M.P. Sotiriou, J.S. Aristeidakis, M.-I.T. Tzini, I. Papadioti, G.N. Haidemenopoulos, N. Aravas, Microstructural and Thermomechanical Simulation of the Additive Manufacturing Process in 316L Austenitic Stainless Steel, (2021) 20. https://doi.org/10.3390/iec2m-09237.

[54] H.D. Hibbitt, ABAQUS/EPGEN-A general purpose finite element code with emphasis on nonlinear applications, Nuclear Engineering and Design. 77 (1984) 271–297. https://doi.org/10.1016/0029-5493(84)90106-7.

[55] C.S. Kim, Thermophysical properties of stainless steels, (n.d.). https://doi.org/10.2172/4152287.

[56] P. Michaleris, Modeling metal deposition in heat transfer analyses of additive manufacturing processes, Finite Elements in Analysis and Design. 86 (2014) 51–60. https://doi.org/10.1016/j.finel.2014.04.003.

[57] S. Koimtzidis, Simulation of Additive Manufacturing (3-D Printing), 2022.

[58] L.A. Spyrou, N. Aravas, Thermomechanical modeling of laser spot welded solar absorbers, Journal of Manufacturing Science and Engineering, Transactions of the ASME. 137 (2015). https://doi.org/10.1115/1.4028197.

[59] Wakao N., Kaguei S., Heat and Mass Transfer in Packed Beds, (n.d.).

[60] D.A. de Moraes, A. Czekanski, Parametric thermal fe analysis on the laser power input and powder effective thermal conductivity during selective laser melting of ss304l, Journal of Manufacturing and Materials Processing. 2 (2018). https://doi.org/10.3390/jmmp2030047.

[61] S. Sumin Sih, J.W. Barlow, The prediction of the emissivity and thermal conductivity of powder beds, Particulate Science and Technology. 22 (2004) 291–304. https://doi.org/10.1080/02726350490501682a.

[62] S. Hocine, H. van Swygenhoven, S. van Petegem, Verification of selective laser melting heat source models with operando X-ray diffraction data, Addit Manuf. 37 (2021). https://doi.org/10.1016/j.addma.2020.101747.

[63] EOS StainlessSteel 316L Material Data Sheet Metal Solutions.

[64] T. Hoshino, K. Mito, A. Nagashima, M. Miyata, Determination of the Thermal Conductivity of Argon and Nitrogen over a Wide Temperature Range Through Data Evaluation and Shock-Tube Experiments, 1986.

[65] H. Ali, H. Ghadbeigi, K. Mumtaz, Residual stress development in selective laser-melted Ti6Al4V: a parametric thermal modelling approach, The International

Journal of Advanced Manufacturing Technology. 97 (2018) 2621–2633. https://doi.org/10.1007/s00170-018-2104-9.

[66] M.F. Gouge, J.C. Heigel, P. Michaleris, T.A. Palmer, Modeling forced convection in the thermal simulation of laser cladding processes, International Journal of Advanced Manufacturing Technology. 79 (2015) 307–320. https://doi.org/10.1007/s00170-015-6831-x.

[67] P. Michaleris, Modeling metal deposition in heat transfer analyses of additive manufacturing processes, Finite Elements in Analysis and Design. 86 (2014) 51–60. https://doi.org/10.1016/j.finel.2014.04.003.

[68] Z.-K. Liu, Y. Wang, CALPHAD modeling of thermodynamics, in: Computational Thermodynamics of Materials, Cambridge University Press, 2016: pp. 150–164. https://doi.org/10.1017/CBO9781139018265.006.

[69] H. Lukas, S.G. Fries, B. Sundman, Computational Thermodynamics: The Calphad Method, Cambridge University Press, 2007. https://doi.org/10.1017/CBO9780511804137.

[70] L. Kaufman, Computational Thermodynamics and materials design, Calphad. 25 (2001) 141–161. https://doi.org/https://doi.org/10.1016/S0364-5916(01)00039-6.

[71] J. Andersson, J. Ågren, Models for numerical treatment of multicomponent diffusion in simple phases, J Appl Phys. 72 (1992) 1350–1355. https://doi.org/10.1063/1.351745.

[72] L. Kaufman, H. Bernstein, Computer calculation of phase diagrams With special reference to refractory metals, Academic Press Inc, United States, 1970. http://inis.iaea.org/search/search.aspx?orig_q=RN:02004171.

[73] A. Borgenstam, A. Engstro, L. Ho, J.A.˚ Gren, DICTRA, a Tool for Simulation of Diffusional Transformations in Alloys.

[74] G.N. Haidemenopoulos, Physical Metallurgy: Principles and Design, CRC Press, 2018. https://books.google.gr/books?id=8KdWAQAACAAJ.

[75] M.P. Sotiriou, M.I.T. Tzini, J.S. Aristeidakis, G.N. Haidemenopoulos, I. Barsoum, A computational study of solidification during additive manufacturing of AISI 304 austenitic stainless steel, 7th Panhellenic Conference on Metallic Materials. (2019) 6. https://www.researchgate.net/publication/337948458_A_computational_study_of_solidification_during_additive_manufacturing_of_AISI_304_austenitic_stainless_steel.

[76] M. Godec, S. Zaefferer, B. Podgornik, M. Šinko, E. Tchernychova, Quantitative multiscale correlative microstructure analysis of additive manufacturing of stainless steel 316L processed by selective laser melting, Mater Charact. 160 (2020) 110074. https://doi.org/10.1016/J.MATCHAR.2019.110074.

[77] S. Hammadi, Solidification Modeling of Microsegregation, (2018) 30. http://urn.kb.se/resolve?urn=urn:nbn:se:kth:diva-231496%0Ahttps://drive.google.com/open?id=1royJZTR8bFqyXphTMhUwkK9CyUzw3hrv.

[78] W.J. Poole, F. Weinberg, Observations of the columnar-to-equiaxed transition in stainless steels, Metall Mater Trans A Phys Metall Mater Sci. 29 A (1998) 855–861. https://doi.org/10.1007/s11661-998-0276-x.

[79] K. Saeidi, X. Gao, F. Lofaj, L. Kvetková, Z.J. Shen, Transformation of austenite to duplex austenite-ferrite assembly in annealed stainless steel 316L consolidated by laser melting, J Alloys Compd. 633 (2015) 463–469. https://doi.org/10.1016/j.jallcom.2015.01.249.

[80] K. Saeidi, X. Gao, Y. Zhong, Z.J. Shen, Hardened austenite steel with columnar sub-grain structure formed by laser melting, Materials Science and Engineering A. 625 (2015) 221–229. https://doi.org/10.1016/j.msea.2014.12.018.

[81] P. Krakhmalev, G. Fredriksson, K. Svensson, I. Yadroitsev, I. Yadroitsava, M. Thuvander, R. Peng, Microstructure, solidification texture, and thermal stability of 316 L stainless steel manufactured by laser powder bed fusion, Metals (Basel). 8 (2018). https://doi.org/10.3390/met8080643.

[82] Y.M. Wang, T. Voisin, J.T. McKeown, J. Ye, N.P. Calta, Z. Li, Z. Zeng, Y. Zhang, W. Chen, T.T. Roehling, R.T. Ott, M.K. Santala, P.J. Depond, M.J. Matthews, A. V. Hamza, T. Zhu, Additively manufactured hierarchical stainless steels with high strength and ductility, Nat Mater. 17 (2018) 63–70. https://doi.org/10.1038/NMAT5021.

[83] P. Ansari, A.U. Rehman, F. Pitir, S. Veziroglu, Y.K. Mishra, O.C. Aktas, M.U. Salamci, Selective laser melting of 316l austenitic stainless steel: Detailed process understanding using multiphysics simulation and experimentation, Metals (Basel). 11 (2021). https://doi.org/10.3390/met11071076.

[84] D.J. Sprouster, W. Streit Cunningham, G.P. Halada, H. Yan, A. Pattammattel, X. Huang, D. Olds, M. Tilton, Y.S. Chu, E. Dooryhee, G.P. Manogharan, J.R. Trelewicz, Dislocation microstructure and its influence on corrosion behavior in laser additively manufactured 316L stainless steel, Addit Manuf. 47 (2021). https://doi.org/10.1016/j.addma.2021.102263.

[85] Z. Sun, X. Tan, S.B. Tor, W.Y. Yeong, Selective laser melting of stainless steel 316L with low porosity and high build rates, Mater Des. 104 (2016) 197–204. https://doi.org/10.1016/j.matdes.2016.05.035.

[86] W.W. Mullins, R.F. Sekerka, Stability of a planar interface during solidification of a dilute binary alloy, J Appl Phys. 35 (1964) 444–451. https://doi.org/10.1063/1.1713333.

[87] R. Trivedi, W. Kurz, Dendritic growth, 1994.

[88] M.I. Tzini, P. Sarafoglou, A. Stieben, G. Haidemenopoulos, W. Bleck, Austenite Evolution and Solute Partitioning during Thermal Cycling in the Intercritical

Range of a Medium-Mn Steel, Steel Res Int. 87 (2016) 1686–1693. https://doi.org/10.1002/srin.201600050.

Biography note

Marios P. Sotiriou

Marios Sotiriou is a research assistant at the Laboratory of Materials, at the Department of Mechanical Engineering of the University of Thessaly, in Volos, Greece. His work is based on the development of a benchmark simulation framework to predict the microstructural evolution of austenitic stainless steels in welding and additive manufacturing processes, with an objective to set the simulation foundations for material design and optimization in additive manufacturing applications. He has developed an operational toolbox in tackling physical metallurgy problems, with targeted skills in computational multi-disciplinary modeling that relies on CALPHAD-based computational thermodynamic and kinetic tools of microstructural evolution, FEA, as well as experimental investigation techniques. His interests include solidification and diffusive solid-state transformations, additive manufacturing and welding of austenitic stainless steels, computational thermodynamics and kinetics modeling for process and alloy design in metallic materials, CALPHAD methodology for Integrated Computational Materials Engineering (ICME), FEA thermomechanical modeling and simulation of additive manufacturing processes, selective Laser Melting of H13 tool steel for extrusion applications and aluminium alloy refinement via partial solidification of intermetallic compounds under presence of a Lorentz field.

He aims in advancing his research in the cross-section of the fields of metallurgy and solid mechanics, towards development of materials design methodologies. He is interested in multi-disciplinary modeling (thermomechanical, diffusional, constitutional), to develop holistic approaches in combined heat/mass transfer simulations, as well as advanced optimization techniques. He is concerned with overcoming the challenges in a wide range of applications, including process design (e.g., additive manufacturing), materials for exotic uses (space exploration, metal composite matrices), computing, high-performance structural materials and transportation.

Email: mpsotiriou@gmail.com, contact@mpsotiriou.com

ResearchGate | Google Scholar | Personal Website

Working papers

1. M.P. Sotiriou, J.S. Aristeidakis, I. Papadioti, M.I.T. Tzini, N. Aravas, G.N. Haidemenopoulos, “Microstructural and thermomechanical modeling and simulation of selective laser melting in austenitic stainless steels”.
2. M.P. Sotiriou, J.S. Aristeidakis, M.I.T. Tzini, G.N. Haidemenopoulos, “Modeling microstructural evolution of austenitic stainless steels in welding and additive manufacturing”.

Conferences

1. M.P. Sotiriou, J.S. Aristeidakis, S. Koimtzidis, I. Papadioti, M.I.T. Tzini, N. Aravas, G.N. Haidemenopoulos, “Microstructural and heat transfer modeling of selective laser melting in austenitic stainless steels”, 8th International Conference of the Hellenic Metallurgical Society, December 14-16, 2022.
2. M.P. Sotiriou, J.S. Aristeidakis, M.I.T. Tzini, I. Papadioti, G.N. Haidemenopoulos, N. Aravas, “Thermomechanical and microstructural simulation of the AM process of 316L austenitic stainless steel”, 6th International Virtual Conference of Engineering Against Failure, June 23-25, 2021.
3. M.P. Sotiriou, V.D. Daniil, J.S. Aristeidakis, G.N. Haidemenopoulos, Abstract: “Thermodynamics of intermetallics formation from liquid state, during the refinement procedure of recycled aluminium alloy melt”, 1st Online Symposium for Young Scientists on Minerals, Environment, Chemical Engineering, February 26-28, 2021, Kozani, Greece.
4. Marios P. Sotiriou, John S. Aristeidakis, Maria-Ioanna T. Tzini, Ioanna Papadioti, Gregory N. Haidemenopoulos, Nikolaos Aravas, “Microstructural and Thermomechanical Simulation of the Additive Manufacturing Process in 316L Austenitic Stainless Steel”, The 1st International Electronic Conference on Metallurgy and Metals, Volume: Mater. Proc. 2021, 3(1), 20, DOI: 10.3390/IEC2M-09237.
5. M.P. Sotiriou, M.I.T. Tzini, J.S. Aristeidakis, G.N. Haidemenopoulos, I. Barsoum, “A computational study of solidification during additive manufacturing of AISI 304 austenitic stainless steel”, 7th Pan-Hellenic Conference of Metallic Materials, December 11-13, 2019. Available at ResearchGate.